



### 저작자표시-비영리-동일조건변경허락 2.0 대한민국

이용자는 아래의 조건을 따르는 경우에 한하여 자유롭게

- 이 저작물을 복제, 배포, 전송, 전시, 공연 및 방송할 수 있습니다.
- 이차적 저작물을 작성할 수 있습니다.

다음과 같은 조건을 따라야 합니다:



저작자표시. 귀하는 원저작자를 표시하여야 합니다.



비영리. 귀하는 이 저작물을 영리 목적으로 이용할 수 없습니다.



동일조건변경허락. 귀하가 이 저작물을 개작, 변형 또는 가공했을 경우에는, 이 저작물과 동일한 이용허락조건하에서만 배포할 수 있습니다.

- 귀하는, 이 저작물의 재이용이나 배포의 경우, 이 저작물에 적용된 이용허락조건을 명확하게 나타내어야 합니다.
- 저작권자로부터 별도의 허가를 받으면 이러한 조건들은 적용되지 않습니다.

저작권법에 따른 이용자의 권리는 위의 내용에 의하여 영향을 받지 않습니다.

이것은 [이용허락규약\(Legal Code\)](#)을 이해하기 쉽게 요약한 것입니다.

[Disclaimer](#)

Ph.D. Dissertation

**EMCCD-Based  
Multi-Qubit State Discrimination of  
Trapped Ions Enhanced by Machine  
Learning**

머신러닝을 활용한 EMCCD 기반  
다중 이온 상태측정 신뢰도 향상 방법

August 2023

**Department of Electrical and  
Computer Engineering  
Seoul National University**

**Junho Jeong**

# EMCCD-Based Multi-Qubit State Discrimination of Trapped Ions Enhanced by Machine Learning

지도 교수 조 동 일

이 논문을 공학박사 학위논문으로 제출함

2023년 6월

서울대학교 대학원  
전기·정보 공학부  
정 준 호

정준호의 공학박사 학위논문을 인준함

2023년 6월

Chair	<u>박 남 규</u>
Vice Chair	<u>조 동 일</u>
Examiner	<u>윤 성 로</u>
Examiner	<u>김 태 현</u>
Examiner	<u>최 태 영</u>

## Abstract

Quantum information processing is a rapidly growing field with the potential to revolutionize computing, communication, and cryptography. However, to achieve the full potential of quantum computing, fast and accurate measurements of quantum states are essential. Especially, measuring the individual state of multiple qubits with high fidelity is challenging as the number of qubits is increasing.

Ion traps are one of the promising platforms for realizing quantum computers due to their long coherence time and self-calibration, which arise from the identical characteristics of ions throughout the universe. The state measurement of trapped ions is carried out by collecting state-dependently scattered photons from ions. To individually measure the state of each ion, the detector not only can detect photons with high sensitivity but also provide spatial information for the detected photons.

One promising device for multi-qubit state measurement of trapped ions is the electron-multiplying charge-coupled device (EMCCD). This device has a unique ability to amplify single-photon-level small signals with electron-multiplying (EM) gain and to provide spatial measurement with a grid-like sensors array.

Several strategies have been investigated from an experimental setup

perspective to enhance the state detection fidelity of trapped ions. These include utilizing the time information of scattered photons, improving the quantum efficiency of the detector, and expanding the coverage angle of the photon-collecting system. From an algorithmic perspective, two methods have been developed to determine the state of the ion. One is the threshold method, which determines the state of the ion based on a criterion. The second is the maximum-likelihood method, which determines the ion's state by considering the probability of the measured data belonging to each state and selecting the most probable one.

Recently, with the rapid growth of machine learning technology, there have been several attempts to apply machine learning to the field of state detection. Since machine learning models have the capability to automatically learn the noise patterns of the detector and capture unique local patterns of signals that may not be considered in the analysis, these attempts have shown superior performance compared to conventional algorithmic methods.

Convolutional neural networks (CNNs) are powerful deep-learning algorithms that are widely used in many fields, including image and speech recognition. CNNs are particularly renowned for their exceptional performance in handling image data, which is typically represented as 2D grid-like data. This is due to the unique architecture and operations of CNNs that allow them to effectively capture spatial dependencies and hierarchical

features within images. By employing convolutional layers, pooling layers, and non-linear activation functions, CNNs can automatically learn and extract relevant features from images, enabling accurate image recognition, object detection, and other visual tasks.

In this dissertation, to acquire all 16 quantum states of a 4-ion chain with high fidelity,  $^{170}\text{Yb}^+$ , an isotope of the qubit ion ( $^{171}\text{Yb}^+$ ), which barely interacts with the detection beam is used to represent  $|0\rangle$  states in the ion chain. In contrast, the  $^{171}\text{Yb}^+$  ions are prepared in the  $|1\rangle$  state with high fidelity and serve as representatives of the  $|1\rangle$  states. This technique enables the acquisition of EMCCD images of the deterministic state of multi-qubits with high fidelity, without individual multi-qubit control.

A CNN model is then applied to the acquired data to determine the quantum states of the ions, and these results are compared to those of conventional methods, namely the threshold method and the maximum-likelihood method. It is observed that the CNN models not only outperform the conventional methods but are also more robust to the long-term positional drift of the trapped ions, promising high reliability over an extended period during the experiment.

The results of this study, showing sustained performance even with an increasing number of qubits, are expected to help develop practical quantum computers and their application in quantum error correction for the future.

Keywords: Ion Trap, Machine Learning, Quantum Information, EMCCD,

Quantum State Detection

Student Number: 2017-28386

# Table of Contents

<b>CHAPTER 1. INTRODUCTION .....</b>	<b>1</b>
1.1. QUANTUM INFORMATION PROCESSING AND QUBITS .....	1
1.2. MULTI-QUBIT SYSTEM .....	4
1.3. QUBIT CONTROL WITH MICROWAVE .....	5
1.4. ION TRAP .....	10
1.5. MEMS-BASED SURFACE-ELECTRODE ION TRAP .....	15
<b>CHAPTER 2. YTTERBIUM .....</b>	<b>18</b>
2.1. 399-NM SPECTROSCOPY OF NEUTRAL YTTERBIUM.....	20
2.2. ISOTOPE-SELECTIVE YB ION TRAPPING .....	23
<b>CHAPTER 3. QUANTUM STATE DETECTION.....</b>	<b>26</b>
3.1. QUANTUM STATE DETECTION OF TRAPPED IONS .....	26
3.2. SCATTERING RATE OF $^{171}\text{Yb}^+$ ION.....	27
3.3. STATE PREPARATION .....	33
3.4. THEORETICAL STATE DETECTION FIDELITY .....	34
<b>CHAPTER 4. EMCCD .....</b>	<b>41</b>
4.1. CONCEPT .....	41
4.2. ELECTRON-MULTIPLYING GAIN.....	43
4.3. NOISES OF EMCCD.....	45

4.3.1	Signal-to-Noise Ratio (SNR) .....	4 5
4.3.2	Shot Noise.....	4 5
4.3.3	Dark Current .....	4 6
4.3.4	Clock-Induced Charge Noise .....	4 8
4.3.5	Readout Noise.....	4 9
4.3.6	Summary.....	4 9
<b>CHAPTER 5. MACHINE LEARNING.....</b>		<b>5 1</b>
5.1.	OVERVIEW .....	5 1
5.2.	POPULAR ALGORITHMS IN DEEP LEARNING .....	5 2
5.2.1	Feedforward Neural Networks (FNNs).....	5 2
5.2.2	Recurrent Neural Networks (RNNs).....	5 3
5.2.3	Convolutional Neural Networks (CNNs).....	5 5
5.2.4	Vision Transformer (ViT) .....	5 7
5.3.	POPULAR BASE MODELS OF CNNs .....	5 8
5.3.1	ResNet.....	5 8
5.3.2	MobileNet.....	6 0
5.3.3	SqueezeNet .....	6 1
5.3.4	ShuffleNet.....	6 3
5.4.	CLASSIFICATION .....	6 3
5.5.	OBJECT DETECTION.....	6 4
<b>CHAPTER 6. SETUP .....</b>		<b>6 6</b>

6.1.	EXPERIMENTAL SETUP .....	6 6
6.2.	EXPERIMENTAL CONTROLLER .....	6 9
6.3.	TIMING OPTIMIZATION .....	7 0
6.3.1	Rising time and falling time of an acousto-optic modulator .....	7 0
6.3.2	Synchronization of the FPGA with EMCCD .....	7 4
6.4.	PARAMETER OPTIMIZATION.....	7 8
6.4.1	High Preparation Fidelity.....	7 8
6.4.2	Detection time optimization.....	7 9
6.5.	MACHINE LEARNING MODEL DESIGN .....	8 3
<b>CHAPTER 7. EXPERIMENT .....</b>		<b>8 7</b>
7.1.	MULTI-QUBIT STATE PREPARATION .....	8 7
7.2.	EMCCD-BASED MULTI-QUBIT STATE DETECTION .....	9 2
7.2.1	Characteristics of Pixels of EMCCD .....	9 2
7.2.2	Experimental Sequence.....	9 3
7.2.3	Determination of ROIs for Each Ion.....	9 6
7.2.4	Simultaneous Rabi Oscillation.....	9 6
<b>CHAPTER 8. RESULTS .....</b>		<b>9 9</b>
8.1.	SINGLE QUBIT STATE DETECTION .....	9 9
8.1.1	Threshold Method.....	1 0 0
8.1.2	Maximum likelihood method.....	1 0 0

8.1.3	Machine learning .....	1 0 3
8.2.	MULTI-QUBIT STATE DETECTION .....	1 0 5
8.2.1	Threshold method .....	1 0 6
8.2.2	Maximum likelihood method.....	1 0 7
8.2.3	ResNet-based CNN model.....	1 0 8
8.2.4	Simultaneous Rabi oscillation of 4 qubits.....	1 0 9
8.2.5	Other Models .....	1 1 3
8.2.6	Robustness Against Optical System Drift .....	1 1 4
<b>CHAPTER 9. DISCUSSION AND CONCLUSIONS.....</b>		<b>1 1 7</b>

# List of Figures

Figure 1-1. A single qubit visualized on the Bloch sphere. ....	2
Figure 1-2. Visualized Rabi oscillation on the Bloch sphere with detuning. ....	9
Figure 1-3. Theoretical Rabi oscillations with different detunings. ....	1 0
Figure 1-4. Simulation result of the pseudopotential. ....	1 5
Figure 1-5. Two small-sized four-rod ion traps. ....	1 6
Figure 2-1. Energy levels of $\text{Yb}^+$ ion. ....	1 9
Figure 2-2. CCD snapshots of the ion trap chip and laser scattering. ....	2 2
Figure 2-3. Spectroscopy result of the ytterbium oven. ....	2 3
Figure 2-4. CCD image of a trapped single $^{174}\text{Yb}^+$ ion. ....	2 5
Figure 3-1. Simplified energy levels of $^{171}\text{Yb}^+$ . ....	2 9
Figure 3-2. Coherent population trapping (CPT) compared to transitions of $^{171}\text{Yb}^+$ with a high-intensity detection beam. ....	3 2
Figure 3-3. Measured photon count result of $^{171}\text{Yb}^+$ with respect to the beam power. ....	3 3
Figure 3-4. Theoretically calculated detection error rate regarding the detection beam intensity. ....	3 7
Figure 3-5. Histograms of detected photon numbers for 25 $\mu\text{s}$ , 50 $\mu\text{s}$ , and 150 $\mu\text{s}$ , respectively. ....	3 9

Figure 4-1. EMCCD device that is used for experiments.....	4 2
Figure 4-2. Configuration diagram of EMCCD: The image section detects photons through the photoelectric effect from the sensor.....	4 4
Figure 4-3. Measured dark current in EMCCD device. ....	4 8
Figure 5-1. A unit of a perceptron.....	5 2
Figure 5-2. Shortcut connection in ResNet .....	6 0
Figure 6-1. The simplified diagram of the experimental setup. ....	6 7
Figure 6-2. Setup for combining two laser beams.....	6 9
Figure 6-3. ARTY S7-50 FPGA as an experimental controller. ....	7 0
Figure 6-4. Measurement results of rising time and falling time of the AOM .....	7 3
Figure 6-5. D-type connector interface of EMCCD.....	7 5
Figure 6-6. Timing diagram of the “Fire Out” and the stopwatch signals in the FPGA.....	7 7
Figure 6-7. Measured result of the next “Fire Out” timing within 100 ns. ....	7 7
Figure 6-8. Measured spin flip fidelity by a global microwave. ....	8 0
Figure 6-9. Measurements results of the dark state pumping rate and the bright state pumping rate .....	8 1

Figure 6-10. Measured single photon state detection fidelity for single-shot detection. ....	8 2
Figure 6-11. Layers of the designed Reset-Based CNN model.....	8 6
Figure 7-1. Comparison of energy levels of $^{171}\text{Yb}^+$ and $^{170}\text{Yb}^+$ . ....	8 8
Figure 7-2. EMCCD image of simultaneously trapped $^{170}\text{Yb}^+$ and $^{171}\text{Yb}^+$ ions. ....	9 0
Figure 7-3. Timing diagram of the experimental schedule.....	9 5
Figure 7-4. Measured 4-qubit EMCCD data: the averaged image of all data and symbolic data for each state.....	9 8
Figure 8-1. Result of applying the threshold method to single qubit state measurement. ....	1 0 2
Figure 8-2. Result of applying the maximum likelihood method to a single ion for state detection. ....	1 0 4
Figure 8-3. Unit structure of ResNet. ....	1 0 9
Figure 8-4. Comparison of fidelities with various state detection algorithms .....	1 1 1
Figure 8-5. Coherent Rabi oscillation result of 4 ions.....	1 1 2
Figure A-1. Expected detection error when the ion species is changed. .....	1 2 2

Figure A-2. Expected detection error rate when the threshold is 1.5 photons.

..... 1 2 2

## List of Tables

Table 1. Isotopes of ytterbium ions and their transition frequency ..... 9 1

Table 2. Comparison of MIMF when applied to the data with a shifted  
imaging system. .... 1 1 6

Table 3. Performance comparison with different models. .... 1 1 4

# Chapter 1. Introduction

## 1.1. Quantum Information Processing and Qubits

Quantum information processing (QIP) is a field of study that processes information by exploiting principles of quantum mechanics [1]. Compared to classical information processing, which encodes the data as either 1 or 0, QIP can take advantage of the superposition principle to encode the data as both 1 and 0 simultaneously. This enables efficient and rapid calculations that cannot be achieved by classical computers and even is believed classical computers cannot calculate [2], [3].

A quantum bit, or shortly a qubit, is an elemental unit of quantum information. The classical information unit, a bit, can have either one of two values: 0 or 1. However, a qubit can have values of both simultaneously based on the superposition principle in quantum mechanics. The state of the qubit can be represented as a combination of computational bases,  $|0\rangle$  and  $|1\rangle$ , as written below.

$$|\psi\rangle = \alpha|0\rangle + \beta|1\rangle \tag{1.1}$$

where the numbers  $\alpha$  and  $\beta$  are complex numbers. If a measurement is made, the quantum state  $|\psi\rangle$  collapses one of two states. the probability that we get  $|0\rangle$  is  $|\alpha|^2$ . Similarly, the probability that we get  $|1\rangle$  is  $|\beta|^2$ . Since

the total probability should be 1, this satisfies  $|\alpha|^2 + |\beta|^2 = 1$ .

Now we can imagine a sphere that has a radius of 1, and the pure states  $|0\rangle$  and  $|1\rangle$  on each pole. Using the global phase  $\gamma$  and the relative phases  $\theta, \phi$ , we can rewrite Equation (1.1) as

$$|\psi\rangle = e^{i\gamma} \left( \cos\frac{\theta}{2} |0\rangle + e^{i\phi} \sin\frac{\theta}{2} |1\rangle \right), \quad (1.2)$$

where  $\gamma, \theta$ , and  $\phi$  are real numbers. The global phase  $e^{i\gamma}$  is usually ignored for convenience. Figure 1-1 represents the Bloch sphere, which geometrically visualizes the state of Equation (1.2) on an imaginary sphere.

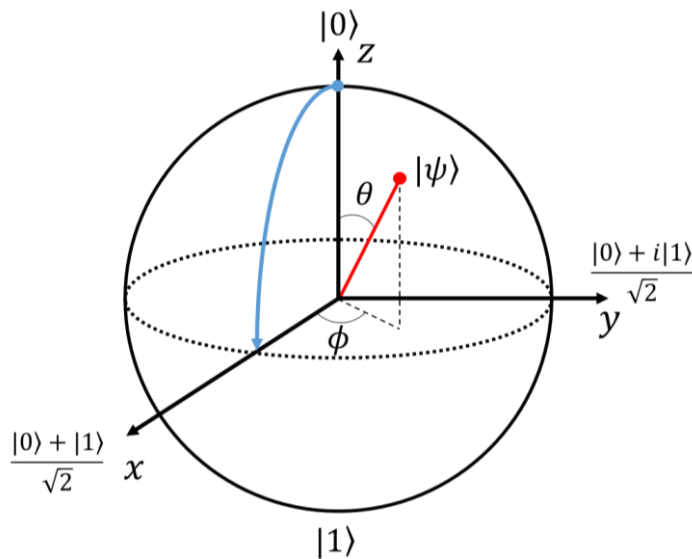


Figure 1-1. A single qubit visualized on the Bloch sphere.

Pauli gates are good tools to represent basic quantum gates that operate on

single qubits. Pauli gates are named after the physicist Wolfgang Pauli. The Pauli gates consist of Pauli  $x$ -gate, Pauli  $y$ -gate, and Pauli  $z$ -gate. The names of gates denote the rotation axis of the operation on the Bloch sphere.

The basic Pauli gates can be represented in  $2 \times 2$  matrices as

$$X = \begin{pmatrix} 0 & 1 \\ 1 & 0 \end{pmatrix} \quad (1.3)$$

$$Y = \begin{pmatrix} 0 & -i \\ i & 0 \end{pmatrix} \quad (1.4)$$

$$Z = \begin{pmatrix} 1 & 0 \\ 0 & -1 \end{pmatrix} \quad (1.5)$$

Although the Bloch sphere is a convenient method to represent the qubit state, it is limited to a single qubit. For quantum computing processors, many algorithms necessitate multiple qubits.

## 1.2. Multi-Qubit System

Quantum computing can be realized with multiple qubits since quantum algorithms for practical levels require a large number of qubits. In quantum computing, qubits are categorized into several types, including computing qubits, memory qubits, and ancilla qubits [3], [4]. Unlike classical computation, quantum computation is probabilistic and susceptible to environmental interference, which can cause errors through a process called decoherence. As the operation time gets longer, the effects of decoherence become more pronounced, making it necessary to use ancilla qubits to correct errors and extend the memory time.

Ancilla qubits play a unique role in quantum computing by allowing the manipulation and control of the state of other qubits in the circuit. This is because the state of a quantum gate depends not only on the input qubits but also on the state of the gate's environment, which can be affected by decoherence and other quantum effects. Ancilla qubits are used to perform specific operations, such as quantum error correction, by interacting with the other qubits in the circuit.

### 1.3. Qubit Control with Microwave

Microwave is a commonly used technique for controlling qubits of trapped ions [5]-[7]. Microwave-based control makes it easier to achieve spin-flips of trapped ions compared to a laser-based method, which requires two beams to be overlapped on the trapped ions. Microwave control requires a finely tuned frequency for high-fidelity control, and it is less sensitive to alignment issues due to its long wavelength.

Due to the long wavelength that reaches about a few centimeters, another advantage of microwave-based control is that it can simultaneously control the quantum states of multiple ions in phase. At the same time, this long wavelength also makes it challenging to control individual qubit control of multiple ions. To achieve individual qubit control, a strong magnetic field gradient necessitates shifting the quantum levels of individual ions by the Zeeman effect [8].

In this dissertation, however, a novel method using an isotope is developed to obtain multi-qubit state detection data with high fidelity. Thus, individual qubit controls were not necessary, a simultaneous qubit control sufficed.

The total Hamiltonian of the system can be written as

$$\hat{H} = \hat{H}_0 + \hat{H}_I \tag{1.6}$$

where  $H_0$  is the unperturbed Hamiltonian and  $H_I$  is the Hamiltonian with a

small perturbation. If we write the eigenstates of the unperturbed system, then

$$|\psi(t)\rangle = \sum_m c_m(t) e^{-iE_m t/\hbar} |m\rangle \quad (1.7)$$

The unperturbed Hamiltonian can be written with defined energy levels as

$$\hat{H}_0 |m\rangle = E_m |m\rangle \quad (1.8)$$

On the other hand, the perturbative Hamiltonian where the electron is interacting with the microwave that oscillates the magnetic field along the z-axis is

$$\hat{H}_I = -\hat{\mu}_z B_0 \cos(\omega t + \delta_0) \quad (1.9)$$

where  $\hat{\mu}_z$  is the magnetic moment of the atom along the z-axis,  $\omega$  is the angular frequency of the microwave,  $B_0$  is the amplitude of the magnetic field, and  $\delta_0$  is the phase of the microwave. The time-dependent Schrodinger equation can be solved by

$$i\hbar \frac{d}{dt} |\psi(t)\rangle = \hat{H} |\psi(t)\rangle \quad (1.10)$$

Combining Eq. (1.7) and Eq. (1.10), and applying the inner product with  $\langle n|$  yield differential equations for the time-dependent coefficients.

$$i\hbar \dot{c}_n e^{-iE_n t/\hbar} = \sum_m c_m e^{-iE_m t/\hbar} \langle n | \hat{H}_I | m \rangle \quad (1.11)$$

The magnetic dipole can be written approximately,

$$\langle n|\hat{H}_I|m\rangle = -B_o \cos(\omega t + \delta_o) \langle n|\hat{\mu}_z|m\rangle \quad (1.12)$$

note that  $\langle n|\hat{\mu}_z|m\rangle$  is zero if  $n = m$ . For simplicity, we define the dipole moment strength  $\langle n|\hat{\mu}_z|m\rangle$  as  $\wp_{nm} = \langle n|\hat{\mu}_z|m\rangle$ ; note that  $\wp_{nm} = \wp_{mn}^*$ .

The transition we have an interest in is only between the two levels  $|0\rangle$  and  $|1\rangle$ . We then can simplify Eq. (1.11) as a system of two equations:

$$\begin{aligned} i\hbar\dot{c}_0 &= -c_1\wp_{10}B_o e^{-i\omega_{10}t} \cos(\omega t + \delta_o) \\ i\hbar\dot{c}_1 &= -c_0\wp_{10}^*B_o e^{i\omega_{10}t} \cos(\omega t + \delta_o) \end{aligned} \quad (1.13)$$

where  $\omega_{10} = (E_1 - E_0)/\hbar$  is defined as the angular frequency difference between the two levels. If we replace the cosine terms with exponential terms, we get

$$\begin{aligned} i\hbar\dot{c}_0 &= -c_1\wp_{10}B_o (e^{i(\omega-\omega_{10})t} e^{i\delta_o} + e^{-i(\omega+\omega_{10})t} e^{-i\delta_o}) \\ i\hbar\dot{c}_1 &= -c_0\wp_{10}^*B_o (e^{i(\omega+\omega_{10})t} e^{i\delta_o} + e^{-i(\omega-\omega_{10})t} e^{-i\delta_o}) \end{aligned} \quad (1.14)$$

Applying the rotating wave approximation (RWA) allows Eq. (1.14) to contain only slowly varying terms. Now we can finally define the Rabi frequency  $\Omega = \wp_{10}B_o/\hbar$ , and the detuning from the resonance of the two levels as  $\Delta = \omega - \omega_{10}$ . The system equations then are simply,

$$\begin{aligned} \dot{c}_0 &= \frac{i\Omega}{2} c_1 e^{i\Delta t} e^{i\delta_o} \\ \dot{c}_1 &= \frac{i\Omega^*}{2} c_0 e^{-i\Delta t} e^{-i\delta_o} \end{aligned} \quad (1.15)$$

Taking the second-order derivative and combining the equations, we get

$$\ddot{c}_1 + i\Delta\dot{c}_1 + \left|\frac{\Omega}{2}\right|^2 c_1 = 0 \quad (1.16)$$

This implies that  $c_1$  and  $c_0$  oscillate by time but in different phases. The solution of this kind of equation has the form:

$$c_1(t) = ae^{\alpha_r t} + be^{\beta_r t} \quad (1.17)$$

where  $\alpha_r = -\frac{i}{2}(\Delta + \sqrt{\Omega^2 + \Delta^2})$  and  $\beta_r = -\frac{i}{2}(\Delta - \sqrt{\Omega^2 + \Delta^2})$ . A generalized Rabi frequency can be defined as  $\Omega_R = \sqrt{\Omega^2 + \Delta^2}$ . Now Eq. (1.17) becomes,

$$c_1(t) = e^{-\frac{i\Delta t}{2}}(ae^{-i\Omega_R t/2} + be^{i\Omega_R t/2}) \quad (1.18)$$

From the initial condition where the electron is initialized to the  $|0\rangle$  state,  $c_1(0) = 0$ , we get  $b = -a$ . Taking the derivative of Eq. (1.18) and replacing the derivative of  $c_1$  in Eq. (1.15), we finally get

$$c_1(t) = \frac{i\Omega^*}{\Omega_R} e^{-i\Delta t/2} e^{-i\delta_o} \sin\left(\frac{1}{2}\Omega_R t\right) \quad (1.19)$$

The probability that the electron can be found in the  $|1\rangle$  state is

$$p_1(t) = |c_1(t)|^2 = \frac{\Omega^2}{\Omega^2 + \Delta^2} \sin^2\left(\frac{1}{2}\sqrt{\Omega^2 + \Delta^2}t\right) \quad (1.20)$$

This is the familiar form of Rabi oscillation [9]. Note that if the microwave is detuned from the resonance, the probability of the  $|1\rangle$  state cannot reach

100%. Therefore, to achieve high-fidelity state preparation, the microwave should be driven on resonance. This can be visualized on the Bloch sphere as shown in Figure 1-2. Detuning causes the rotation axis to tilt by an angle of  $\theta = \arctan(\Delta/\Omega)$ . The resulting tilted axis makes it impossible to detect the  $|1\rangle$  state with 100%.

Theoretically calculated Rabi oscillations with three different detunings ( $\Delta = 0, \Delta = \Omega$ , and  $\Delta = 2\Omega$ ) are illustrated in Figure 1-3.

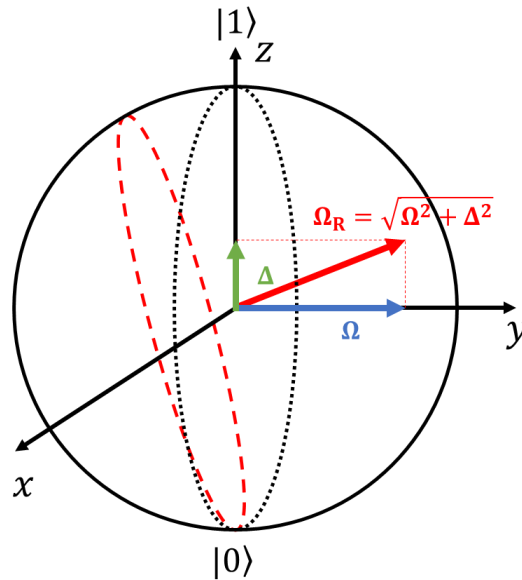


Figure 1-2. Visualized Rabi oscillation on the Bloch sphere with detuning.

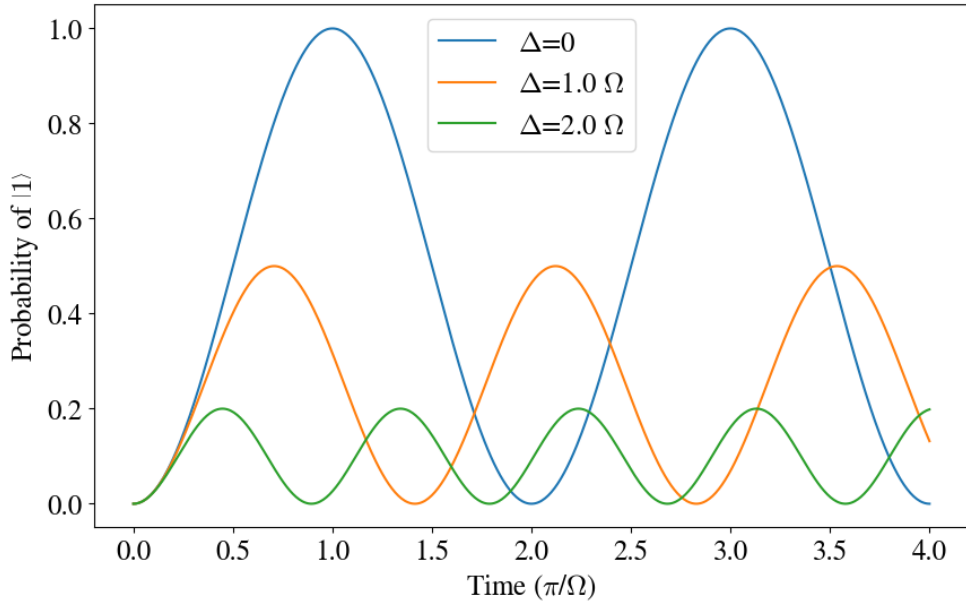


Figure 1-3. Theoretical Rabi oscillations with different detunings.

## 1.4. Ion Trap

Ion traps are devices that trap charged particles using an electrical or electromagnetic field. It is widely used in diverse areas of physics ranging from high to low energies, and from fundamental physics through quantum engineering to simulate space plasmas or solid-state systems [10].

Since charged particles cannot be trapped in a static field due to Earnshaw's theorem [11], that can be written below

$$\nabla \cdot F = \nabla \cdot (-\nabla U) = -\nabla^2 U = 0 \quad (1.21)$$

There are two primary types of ion traps: Penning traps and Paul traps.

Penning traps, named after the physicist Frans Michel Penning, use a combination of electric and magnetic fields to confine charged particles. On the other hand, Paul traps, named after the physicist Wolfgang Paul, confine ions with a combination of a static electric field and a ponderomotive electric field.

The electric field in a Penning trap is typically created by applying a voltage to a ring electrode, while a magnetic field is applied perpendicular to the plane of the ring. The motion of charged particles in a Penning trap can be described using the equations of motion for a charged particle in a magnetic field and an electric field. The magnetic field exerts a Lorentz force on the charged particles, which creates a circular motion of them. Penning traps are typically used for precision spectroscopy experiments by observing the angular frequency of the motion of the trapped particles.

Contrary to the Penning traps, Paul traps use ponderomotive electric fields to trap charged particles. In a Paul trap, two or more cylindrical electrodes are arranged in a linear or circular configuration, and a radio-frequency (RF) voltage is applied to them. The resulting electric field creates a potential well that can trap charged particles in a localized manner. Due to this localization, it is easier to produce lasers to cool and control the quantum state of trapped ions, making Paul traps suitable for quantum information processing.

The motion of trapped ions within the ponderomotive electric field can be described as fast Brownian motion, where their dynamics are characterized by time-averaged behavior. The fast oscillation of the potential can be represented by the time-averaged pseudopotential, which describes the dynamics of charged particles confined by the quadrupole potential [12], which is given by

$$\phi_{\text{pseudo}} = \frac{V_0}{2} \cos(\Omega_T t) \left( 1 + \frac{x^2 - y^2}{R^2} \right), \quad (1.22)$$

where  $\Omega_T$  is the frequency of the ponderomotive potential,  $V_0$  is the amplitude of the input voltage, and  $R$  is the distance from the nearest electrode.

Figure 1-4 shows the simulation result of this pseudopotential, the potential is a quadratic potential well, the ion is trapped and escapes continuously in the saddle point of this potential well as the RF voltage oscillates.

The electric field produced by this potential is now can be derived by

$$\begin{aligned} \hat{E}(x, y, t) &= -\nabla \phi_{\text{pseudo}} \\ &= -\frac{V_0}{R^2} (x\hat{x} - y\hat{y}) \cos(\Omega_T t) \end{aligned} \quad (1.23)$$

The force acting on a particle with mass  $m$  and charge  $e$  in the  $x$ -direction can be described as follows.

$$F_x = m\ddot{x} = eE_x = -x \frac{eV_0}{R^2} \cos(\Omega_T t), \quad (1.24)$$

The equation of the motion is the form of a Mathieu equation, if this is rewritten in a general form of the Mathieu equation, then

$$\frac{d^2 u}{d\tau^2} + (a_u + 2q_u \cos(2\tau))u = 0, \quad (1.25)$$

where  $u$  represents the position of the particle,  $a_u$  represents the static motion of the particle, and  $q_u$  is the oscillating motion of the particle induced by the ponderomotive potential. Note that the term of  $a_u$  can be suppressed by matching the null point of the RF potential and the DC potential in the experimental setup. This extra motion of the particle increases the ion heating during the quantum operation, which significantly degrades the fidelity of the quantum gate [12].

When the term  $a_u$  can be ignored, the equation of the motion is simply the motion of the oscillating particle, which has the form

$$x(t) \approx AC_0 \cos(\omega_x t) \left[ 1 + \frac{q_x}{2} \cos(\Omega_T t) \right] \quad (1.26)$$

where  $A$  is the elemental amplitude of the motion,  $C_0$  the coefficient of the 0-th order of the solution of the Mathieu equation, which is related to the temperature of the trapped ion,  $\omega_x$  is secular frequency, which is the frequency of the motion when it is projected on a single axis, and  $q_x = \frac{(2eV_0)}{mR^2\Omega_T^2}$

is the ponderomotive term oscillating with the frequency of the input RF frequency, which is small and averaged out when the motion of the ion is observed within the trap frequency.

Note that from equation (1.26), when the ion is sufficiently cooled by the Doppler cooling, the amplitude term  $AC$  is small enough ( $\sim 10^{-9}$  m), and the fast-oscillating  $q_x$  term can be negligible. Under these conditions, the trapped ion can be regarded as a static particle, and the amplitude of its motion can be disregarded. This is one additional advantage of trapped ions for physics experiments.

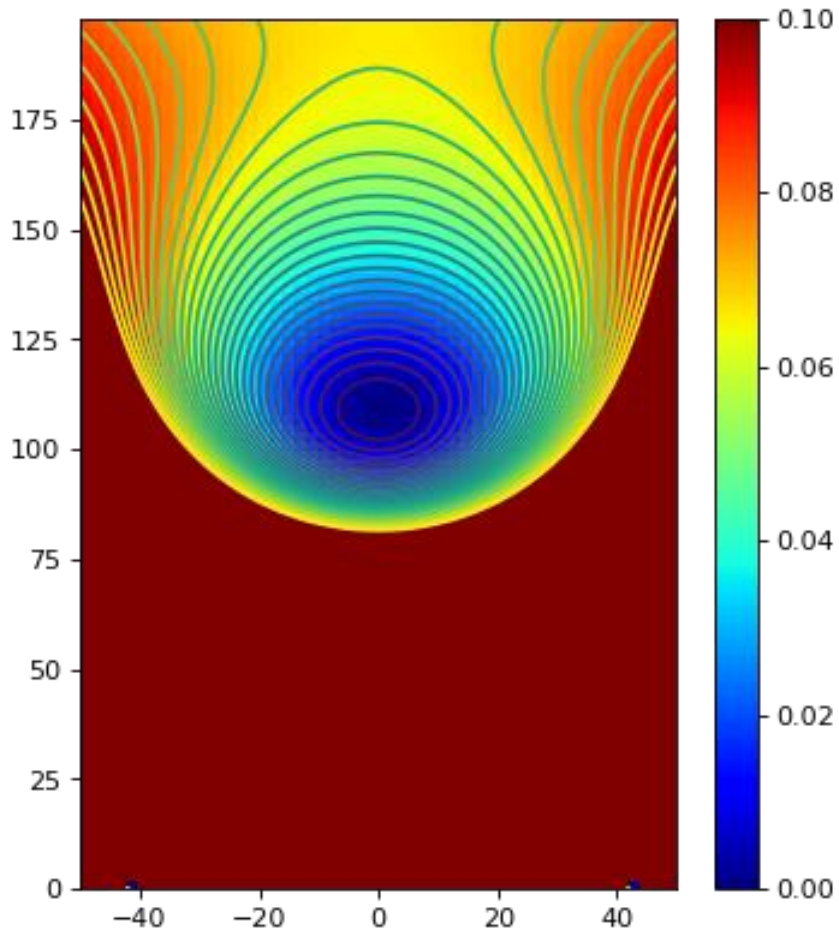


Figure 1-4. Simulation result of the pseudopotential.

### **1.5. MEMS-Based Surface-Electrode Ion Trap**

To realize a large-scale quantum information processor with ion traps, a large number of trapped ions are required. However, due to the large size of the primitive ion traps that can reach several meters, it is challenging to make

them industry-friendly and practical for a quantum processor. This has led to the development of scalable, small-sized ion traps [12], [13].

There are two representative small-sized linear ion traps for quantum information processing illustrated in Figure 1-5: the blade trap, also called a macro-trap, and the micro-electromechanical systems (MEMS)-based surface-electrode ion trap. Both the blade trap and the surface-electrode ion trap are based on a 4-rod trap. Thus, they have a pair of RF electrodes that provide transverse potential, and DC electrodes for longitudinal potential, preventing the ions from escaping.

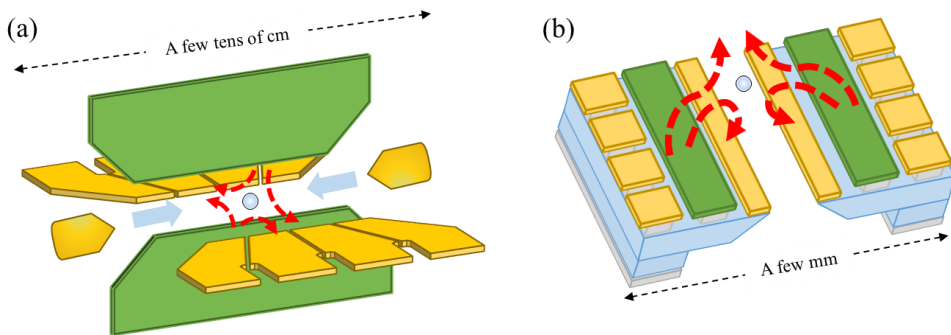


Figure 1-5. Two small-sized four-rod ion traps.

The green electrodes shown in Figure 1-5 indicate RF electrodes that trap the ions transversely, as represented by the dotted red line. The yellow electrodes represent DC electrodes that provide a longitudinal potential to

prevent the trapped ions from escaping. Additionally, some of the DC electrodes are segmented to move the DC potential and enable ion shuttling within the trap by applying different values of the voltages to the electrodes [14].

Since the macro-trap has a larger scale than the surface ion trap, it has some advantages in terms of heating rate. The trapped ions have a greater distance from the closest RF electrode, which results in less anomalous heating [15], [16]. Therefore, blade traps are often used to realize two-qubit gates and fundamental physics experiments that exploit the motional states of trapped ions.

On the other hand, surface ion traps tend to be used for realizing quantum computers. Due to their scalability based on MEMS technology, performing quantum algorithms with high fidelity on surface-electrode ion traps may imply that a quantum computer can be realized. Furthermore, due to the advancement of semiconductor industries such as silicon-based complementary metal oxide semiconductor (CMOS) processes, the fabrication of ion traps based on MEMS is industry-friendly. In this dissertation, MEME-based ion traps fabricated by this research group are used for experiments [17], [18].

## Chapter 2. Ytterbium

Ytterbium is one of the promising Rydberg atoms that can be implemented as a qubit ion [19]. Since its ion can be easily cooled and controlled its quantum states with an industrially manufactured laser. Furthermore, it has a long coherence time compared to other ions [20].

Among the isotopes that have hyperfine levels,  $^{171}\text{Yb}^+$  is commonly used as a qubit ion. Since the level structures are well-known and it is easier to manipulate compared to  $^{173}\text{Yb}^+$ , which requires another laser beam to depopulate hyperfine levels [19].

Figure 2-1 illustrates the energy levels of Ytterbium ions. The strong transition between  $^2S_{1/2}$  and  $^2P_{1/2}$  is utilized for cooling the ion with Doppler cooling [21] and for state detection. A 935-nm laser repumps the electron that occasionally decays to  $^2D_{3/2}$  manifolds. Even though there is no decay channel from  $^3[3/2]_{1/2}$  to  $^2F_{7/2}$ , the electron decayed to the  $^2D_{3/2}$  manifolds sometimes decay to the  $^2F_{7/2}$  manifolds during experiments. It is believed that this transition is driven by the collision with a buffer gas in the UHV chamber [22].

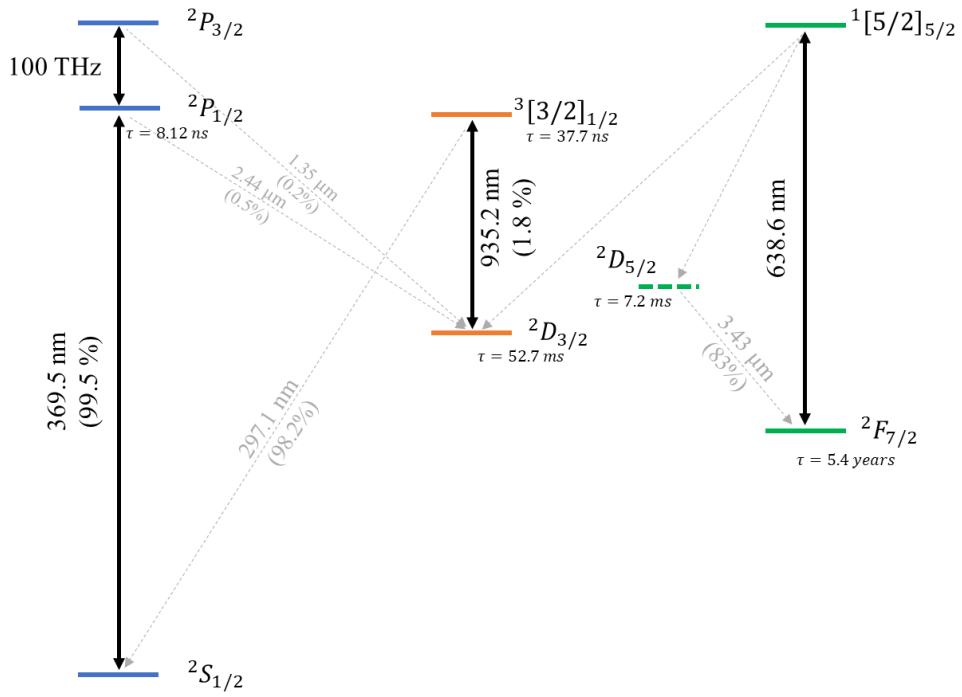


Figure 2-1. Energy levels of  $\text{Yb}^+$  ion.

## **2.1. 399-nm Spectroscopy of Neutral Ytterbium**

By applying a 399-nm laser that is resonant to a specific isotope, one can selectively trap desired isotope ytterbium ions. To achieve this, a 399-nm spectroscopy of neutral ytterbiums in which the ions are expected to be trapped is required. The results of the 399-nm spectroscopic analysis can vary depending on the vacuum chambers used, due to the different Doppler shifts resulting from variations in chamber geometry and installation angles of the ytterbium oven [23].

The spectroscopy was performed as follows: a detector that can detect 399 nm light is placed where the imaging lens focuses. In this dissertation, a CCD camera (Thorlabs, 1501M-USB) is used.

Figure 2-2 shows the snapshot of the CCD with a scattered 399-nm laser. Initially, the 399-nm laser beam is aligned to scatter from the backside of the trap chip. This backside scattering results in photons being scattered in all directions, which allows us to observe all the geometry of the trap chip. Figure 2-2 (a) shows the snapshot of the CCD with backside scattering. Watching the CCD, a 399-nm laser is aligned and focused at the location where the ions are expected to be trapped as shown in Figure 2-2 (b). Then, the ytterbium oven is turned on, letting the ytterbiums be vaporized. Finally, if the oven is heated up enough, the CCD values of the trap position should be recorded while

changing the frequency of the 399-nm laser.

Note that the scattering from the chip surface caused by the strong 399-nm laser obscured the signals from the ions. To address this issue, the laser was slightly positioned higher than the trap position, and the ROI on the CCD was carefully selected. The selected ROI was along the slot of the trap chip, but regions near the electrodes were excluded to reduce the scattering signals. The signals were then averaged for every frequency bin.

The spectroscopy result is shown in Figure 2-3. The peaks of the CCD signals indicate that the frequency of the 399-nm laser is resonant with the evaporated ytterbium atoms, scattering lots of photons. The species of isotopes are confirmed by the measured frequencies and separations of peaks between isotopes.

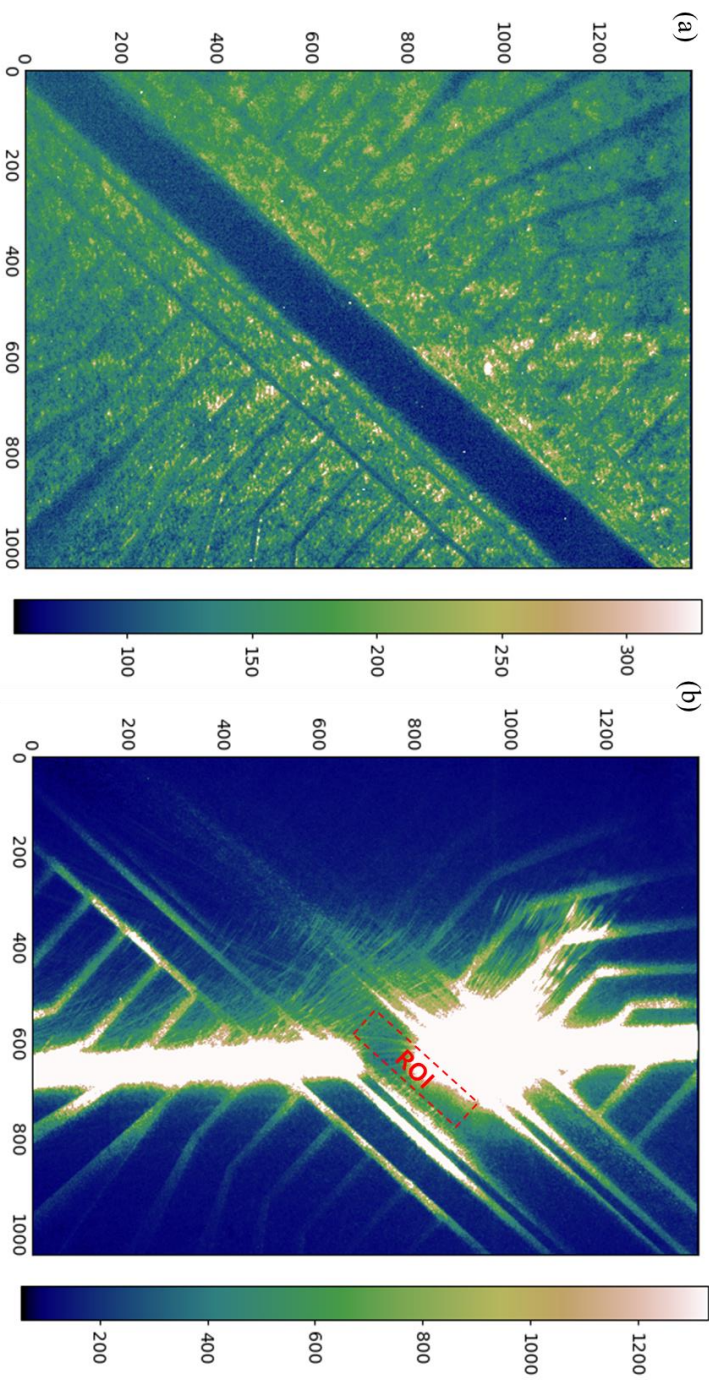


Figure 2-2. CCD snapshots of the ion trap chip and laser scattering.

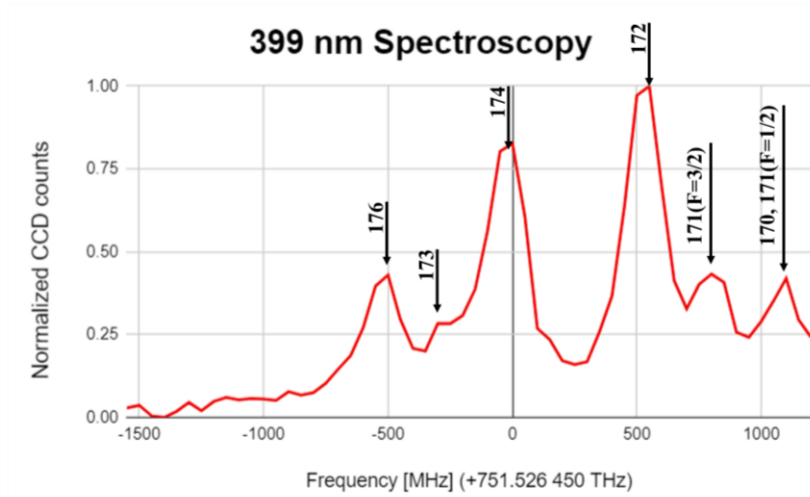


Figure 2-3. Spectroscopy result of the ytterbium oven.

## 2.2. Isotope-Selective Yb Ion Trapping

With the result of spectroscopy, it is now possible to ionize the vaporized neutral ytterbium atoms isotope-selectively and excite the electron from  $^2S_{1/2}$  level to  $^2P_{1/2}$  level. To transit the excited electron to the continuum and make it fully ionized by a two-photon transition [19], a 369-nm laser is counter-propagated to the 399-nm laser.

The fully ionized atom should be cooled immediately in order not to escape from the trap potential by the huge Brownian motion. To mitigate this issue, it is necessary to emit a cooling beam while trapping the ions. Fortunately, the 369-nm cooling beam can send the electron

excited by the 399-nm laser during the first ionization to the continuum energy level. Therefore, only a 399-nm laser and a 369-nm laser are necessary.

Figure 2-4 shows a CCD image of the trapped single  $^{174}\text{Yb}^+$  ion via isotope-selective trapping. To trap the  $^{174}\text{Yb}^+$  ion selectively, the frequency of the 399-nm laser is set to 751.526 450 THz, and the 369-nm laser is set to 811.291 400 THz, which is more than 100 MHz red-detuned from the resonant frequency of  $^{174}\text{Yb}^+$  ion between  $^2S_{1/2}$  and  $^2P_{1/2}$ . Note that the frequency of the 369-nm laser is set to cool the trapped ion, and its frequency does not affect the ionization. Since the 399-nm laser is strongly radiated in the trapping region, even when the 399-nm laser is detuned from the resonance more than 200 MHz, the ion is easily trapped due to the power broadening of the transition.

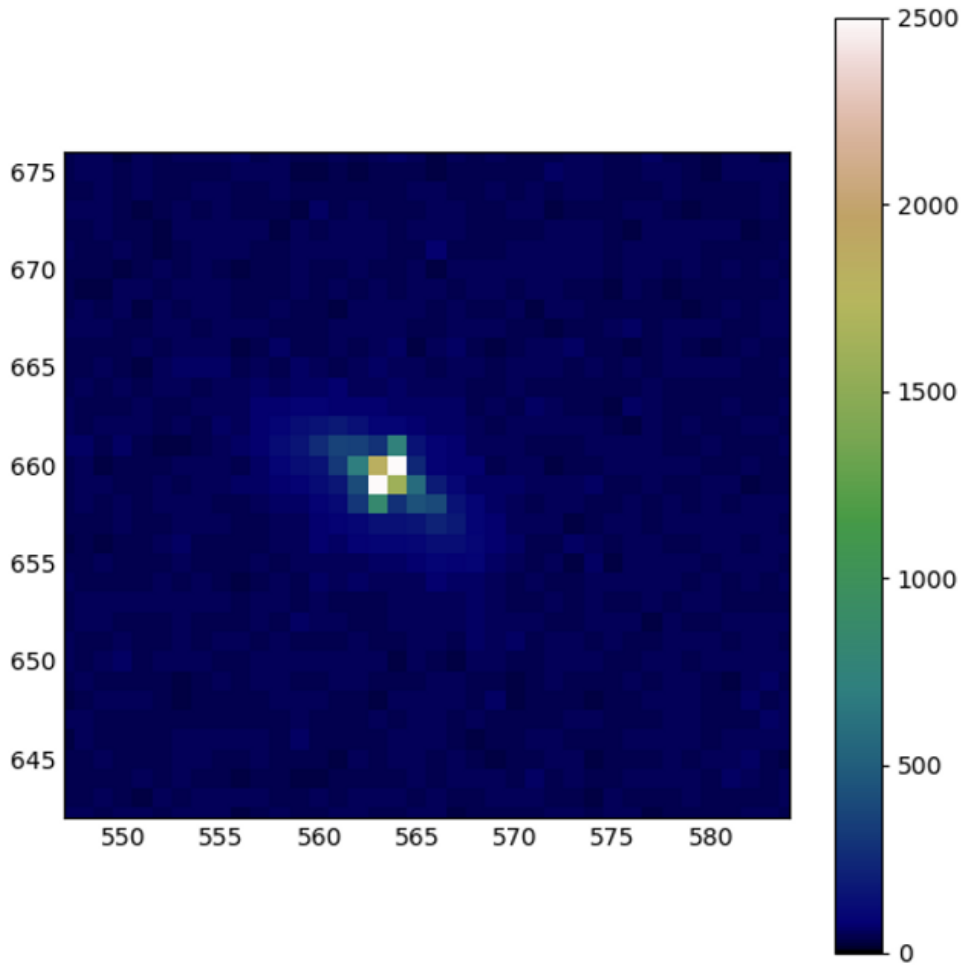


Figure 2-4. CCD image of a trapped single  $^{174}\text{Yb}^+$  ion.

## Chapter 3. Quantum State Detection

### 3.1. Quantum State Detection of Trapped Ions

Quantum state detection with high fidelity is a key step in quantum information processing [1]. It is a prerequisite for realizing quantum error correction (QEC) which is essential for building quantum computers [4], [24]. The QEC detects and corrects errors in quantum bits to preserve the information in quantum states and make the quantum algorithms realizable.

The quantum state of trapped ions can be detected by observing scattered photons from state-dependent cycling transitions [25]. Two internal energy levels of a trapped ion are selected and encoded as  $|0\rangle$  and  $|1\rangle$ , respectively. If a laser that is resonant with a certain energy level of the ion is radiated, and the ion scatters photons, then the state is determined as  $|1\rangle$ . Otherwise, it is determined as  $|0\rangle$ .

However, due to the noise from high-sensitivity detectors and off-resonant transitions during state detection, achieving 100% state detection fidelity is not feasible. The thermally or electrically induced false signals from the detector cannot be distinguished from the actual signals, resulting in a false determination of  $|0\rangle$  as  $|1\rangle$ . Moreover, if the quantum state of an ion in  $|1\rangle$  is changed to  $|0\rangle$  before any photons are detected in the detector during the state detection process, one cannot correctly determine the state as  $|1\rangle$ .

Similarly, if the quantum state of an ion in  $|0\rangle$  is changed to  $|1\rangle$  and scatters lots of photons, it is also impossible to accurately determine the quantum state as  $|0\rangle$ .

To reduce these detection errors, optimizing the detection time to mitigate the errors induced by off-resonant transitions and false signals [26], integrating a micro-fabricated mirror into the trap chip [27], and enhancing quantum efficiency [28] for better photon collection efficiency have been studied for the experimental setup. Moreover, providing more information when determining the quantum state [29], [30] and machine-learning methods also have been explored to improve state detection fidelity [31], [32].

### **3.2. Scattering rate of $^{171}\text{Yb}^+$ Ion.**

Unlike other isotopes with fine structures that can be approximated as a simple two-level system, the hyperfine structure of  $^{171}\text{Yb}^+$  gives several factors to optimize the scattering rate of the ion. With this optimized photon scattering rate, one can reduce the detection time, resulting in a minimized error rate resulting from long exposure of the sensitive detector, as well as a reduced processing time for quantum algorithms.

Figure 3-1 shows relevant energy levels of  $^{171}\text{Yb}^+$  for cooling the ion and manipulating the quantum state. The two levels of  $^{171}\text{Yb}^+$ ,  $^2S_{1/2} |F = 1\rangle$

and  ${}^2S_{1/2} |F = 0\rangle$ , are selected and encoded as  $|1\rangle$  and  $|0\rangle$ , respectively. It should be noted that since the  $|1\rangle$  state has the total angular momentum quantum number  $F = 1$ , which results in three different magnetic quantum values. These three levels, split into different magnetic quantum number values, form a polarization-dependent transition between  ${}^2S_{1/2} |F = 1\rangle$  and  ${}^2P_{1/2} |F = 0\rangle$ , which is used for cooling the ion and detecting the quantum state.

The resulting polarization dependence in the cycling transition inevitably renders at least one state a coherent dark state [33]. Simply put, when the detection beam has  $\pi$ -polarization, the two states of  ${}^2S_{1/2} |F = 1\rangle$  that have magnetic quantum number  $\pm 1$  remain coherent dark states, on the hand, when the detection beam has  $\sigma^\pm$ -polarization, the state of  ${}^2S_{1/2} |F = 1\rangle$  with 0 magnetic quantum number is a coherent dark state.

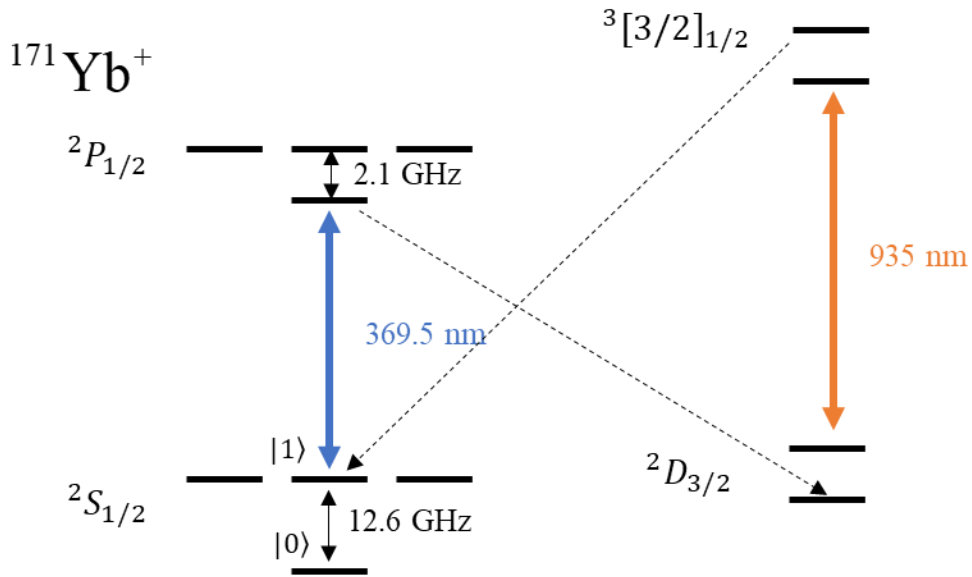


Figure 3-1. Simplified energy levels of  $^{171}\text{Yb}^+$ .

In addition to polarization optimization, the magnetic field strength should also be optimized for maximum photon scattering [33]. When the strength of a magnetic field is not strong enough, the hyperfine splitting is small and makes them degenerate. This degeneracy of hyperfine levels makes the coherent dark state stable and less responsive to the detection beam. On the other hand, when the magnetic field is too strong, causing the hyperfine splitting to become large, the frequency difference from the detection beam also increases, which makes the level less interactive with the beam.

Since the natural linewidth of the excited electron to  $2P_{1/2} |F = 1\rangle$  is

narrow ( $\tau \approx 8$  ns), the photon scattering rate can be approximated as the population rate of the excited state. The population of the excited state of the ion interacting with the detection beam can be expressed as [33]

$$P_f = \frac{3 \Omega^2 \cos^2 \theta_{BE} \sin^2 \theta_{BE}}{4 (1 + 3 \cos^2 \theta_{BE})} \frac{1}{(\Gamma'/2)^2 + \Delta^2}, \quad (3.1)$$

where

$$\begin{aligned} \left(\frac{\Gamma'}{2}\right)^2 &= \left(\frac{\Gamma}{2}\right)^2 + \Omega^2 \cos^2 \theta_{BE} \frac{1 - 3 \cos^2 \theta_{BE}}{1 + 3 \cos^2 \theta_{BE}} \\ &+ \frac{\cos^2 \theta_{BE}}{1 + 3 \cos^2 \theta_{BE}} \left( \frac{\Omega^4}{16\delta_B^4} + 16\delta_B^2 \right) \end{aligned} \quad (3.2)$$

where  $\delta_B = \Omega/4$  is the magnetic-field strength and  $\theta_{BE} = \arccos(1/\sqrt{3})$  is the laser-polarization angle. Both parameters maximize the photon scattering by destabilizing the coherent dark states of hyperfine levels.

The scattering rate with optimized experimental parameters is when setting the saturation parameter  $s_o = 2\Omega^2/\Gamma^2$  [26],

$$R_{o,opt} = \Gamma P_f = \left(\frac{\Gamma}{6}\right) \frac{s_o}{1 + \frac{2}{3}s_o + \left(\frac{2\Delta}{\Gamma}\right)^2}, \quad (3.3)$$

where  $R_{o,opt}$  represents the optimized scattering rate. This optimized scattering rate implies that it is now a function of beam power. Note that at high beam powers the scattering rate drops due to the destabilized coherent dark states [26], [33].

This non-intuitive behavior can be understood as coherent population trapping (CPT) [34]. The CPT is a phenomenon in a 3-level system with two strong laser beams. When the transitions induced by two laser beams share an excited state and have two ground states, the excited state becomes a metastable state by stimulated decay, resulting in no photon emission during the transition.

In CPT, the state of the electron can be written as

$$|\psi\rangle = \frac{\Omega_p|2\rangle - \Omega_s|3\rangle}{\sqrt{|\Omega_p|^2 + |\Omega_s|^2}}, \quad (3.4)$$

where  $\Omega_p$  is the Rabi frequency of the pump beam and  $\Omega_s$  is the Rabi frequency of the scope beam. Note that the transition occurs between the two ground states without photon emission.

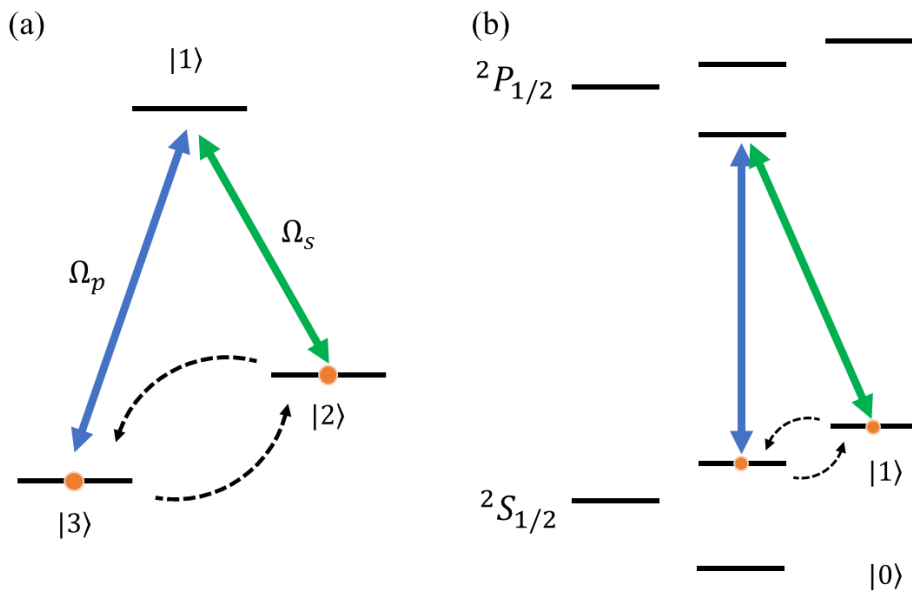


Figure 3-2. Coherent population trapping (CPT) compared to transitions of  $^{171}\text{Yb}^+$  with a high-intensity detection beam.

The measured photon counts of  $^{171}\text{Yb}^+$  are plotted in Figure 3-3. The blue dots represent the measured photon counts by a PMT, and the red line is plotted based on the theoretical fit. The red line is fitted to  $\varepsilon R_{o,opt}$ , where  $\varepsilon$  represents the photon collection efficiency of the system, which includes the solid angle of the imaging lens, losses from optical components, and the quantum efficiency of the PMT. Given that the natural linewidth  $\Gamma$  and the detuning of the laser beam  $\Delta$  are known, the saturation beam power and the total photon collection efficiency  $\varepsilon = 0.023(3)$  can be acquired from the fit.

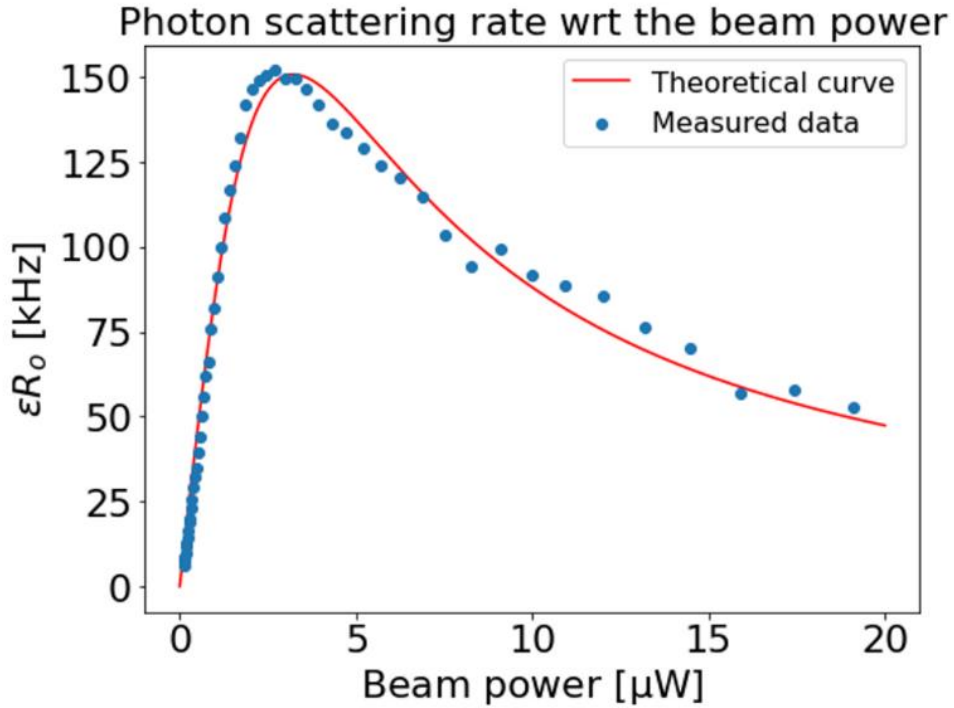


Figure 3-3. Measured photon count result of  $^{171}\text{Yb}^+$  with respect to the beam power.

### 3.3. State Preparation

Before detecting the quantum states of the trapped ions, the states of ions should be prepared as desired. To verify the efficacy of the state measurement, the fidelity of the preparation should be high enough, such that the error rate stemming from the state preparation is negligible. The state preparation fidelity is defined as

$$\bar{F}_{prep} = \frac{1}{2} \sum_s p(\text{prepared } s | \text{desired } s) \quad (3.5)$$

where  $s$  is the state that we want to prepare, which for a single qubit is either  $|0\rangle$  or  $|1\rangle$ .

The  $|0\rangle$  state can be prepared using optical pumping with the beam resonant to the energy between  $^2S_{1/2} |F = 1\rangle$  and  $^2P_{1/2} |F = 1\rangle$  [35]. Since the initialized  $|0\rangle$  state requires large detuning to off-resonantly transferred back to the  $|1\rangle$  state, the preparation error rate of the  $|0\rangle$  is usually very low ( $< 10^{-4}$ ) [28].

On the other hand, the  $|1\rangle$  state is prepared from the  $|0\rangle$  state by flipping the spin with a microwave pulse. To achieve a high-fidelity preparation, one should find the resonance frequency of the two states ( $\Delta \rightarrow 0$ ) and drive the microwave for a  $\pi$ -pulse time. This makes Eq. (1.20) simply  $p_1\left(\frac{\pi}{\Omega}\right) = \sin^2(0.5\pi) = 1$ . However, due to the uncertainty of the frequency standard and the timing margins of the control signals, State preparation fidelity of the  $|1\rangle$  state with 100% cannot be achieved experimentally.

### 3.4. Theoretical State Detection Fidelity

Provided the scattering rate, off-resonant transition rate, and false signal rate of the detector are known, one can calculate the theoretical state detection

fidelity, thus its optimal detection time [26], [28]. When the polarization of the detection beam and the Zeeman splitting of hyperfine levels of  $^2S_{1/2}$  are optimized, the probability of pumping the initial state into a different state is simply [26]

$$R_{pump} = R_{branch} \left(\frac{2}{3}\right) \left(\frac{\Gamma}{2}\right) \left(\frac{2\Omega^2}{\Gamma}\right) \left(\frac{\Gamma}{2\Delta}\right)^2 \quad (3.6)$$

where  $R_{branch}$  is the branching ratio of the spontaneous decay, which is 1/3 for dark state pumping, and 1 for bright state pumping, respectively.  $\Gamma = 2\pi \times 19.6$  MHz is the natural linewidth of the ytterbium ion,  $\Omega$  is the Rabi frequency, and  $\Delta$  is the detuning from the measurement beam for off-resonant transition.

With these pumping rates, one can now calculate the probability that zero photons are detected for a given time of each state respectively [36]. The probability that any photons are not detected from the  $|0\rangle$  state is:

$$P_{t,d}(n = 0) = \frac{R_b}{\varepsilon R_o - R_b} e^{-R_{dc}t} [e^{-R_b t} - e^{-R_o t}] + e^{-R_b t} e^{-R_{dc}t} \quad (3.7)$$

where  $n$  is the detected photon number,  $R_{dc}$  is the dark current of the detector, and  $\varepsilon$  is the total photon detection efficiency in the system, including the solid angle of the imaging lens, quantum efficiency of the

detector and small loss from optical components. Similarly, the probability that no photons are detected when the state is prepared in  $|1\rangle$  state is:

$$\begin{aligned}
 P_{t,b}(n = 0) &= \frac{R_d}{\varepsilon R_o + R_b} e^{-R_{dc}t} [1 \\
 &\quad - e^{-(\varepsilon R_o + R_d)t}] \\
 &\quad + e^{-R_d t} e^{-(\varepsilon R_o + R_{dc})t}
 \end{aligned} \tag{3.8}$$

If we set the threshold to 0.5 photons for the threshold method, we can define the state detention fidelity as:

$$\bar{F}_{Threshold} = \frac{1}{2} [P_{t,d} + (1 - P_{t,b})] \tag{3.9}$$

where the  $1 - P_{t,b}$  term represents the probability that more than one photon is detected. Theoretically calculated state detection error ( $1 - \bar{F}_{threshold}$ ) is shown in Figure 3-4. Note that there is a trade-off between the optimal detection time and the state detection fidelity. A strong detection beam guarantees a short optimal detection time. However, it also increases the pumping rate, resulting in a higher error rate from the off-resonant transition.

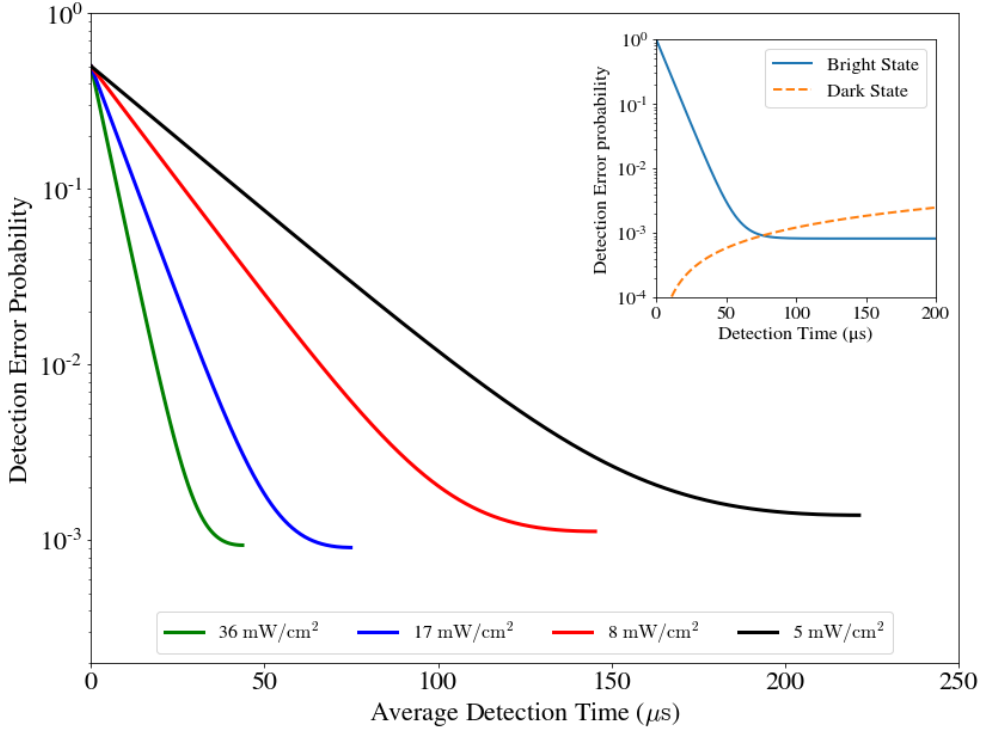


Figure 3-4. Theoretically calculated detection error rate regarding the detection beam intensity.

If we fix the beam intensity to half of the saturation intensity ( $I = 0.5I_{sat}$ ), the bright state pumping rate, the probability that the  $|0\rangle$  state is pumped into the  $|1\rangle$  state by the off-resonant transition, is:

$$R_b = \left(\frac{2}{3}\right) \left(\frac{\Gamma}{2}\right) \left(\frac{1}{2}\right) \left(\frac{\Gamma}{2(2\pi \times 14.7 \text{ GHz})}\right)^2 = 9.12 \text{ Hz} \quad (3.10)$$

Similarly, the dark state pumping rate also can be calculated as

$$\begin{aligned}
R_d &= \left(\frac{1}{3}\right) \left(\frac{2}{3}\right) \left(\frac{\Gamma}{2}\right) \left(\frac{1}{2}\right) \left(\frac{\Gamma}{2(2\pi \times 2.1 \text{ GHz})}\right)^2 \\
&= 149.0 \text{ Hz}
\end{aligned}
\tag{3.11}$$

With these pumping rates, the fidelity of state detection can be calculated. However, since taking into account the state changes due to the off-resonant transition is not an easy task, it is worth trying the Markov chain Monte Carlo (MCMC) simulation, which is a statistical methodology used to simulate probability distributions for situations where the model is too complex to anticipate the final results.

To obtain precise results, 5,000,000 data for the  $|0\rangle$  and  $|1\rangle$  states are sampled. Starting from the initial state, changes in the state and the number of emitted photons are simulated every  $5 \mu\text{s}$  until  $200 \mu\text{s}$  according to the pumping rates and photon emission rate described above. The time bin is set to  $5 \mu\text{s}$  since any changes in the state that occur twice within this time bin can be considered negligible ( $2.8 \times 10^{-14}$ ). If the initial state is changed to a different state, then this final state becomes the initial state for the next time bin to calculate the emitted photons and state changes.

Figure 3-5 shows some histograms of the simulated photons numbers.

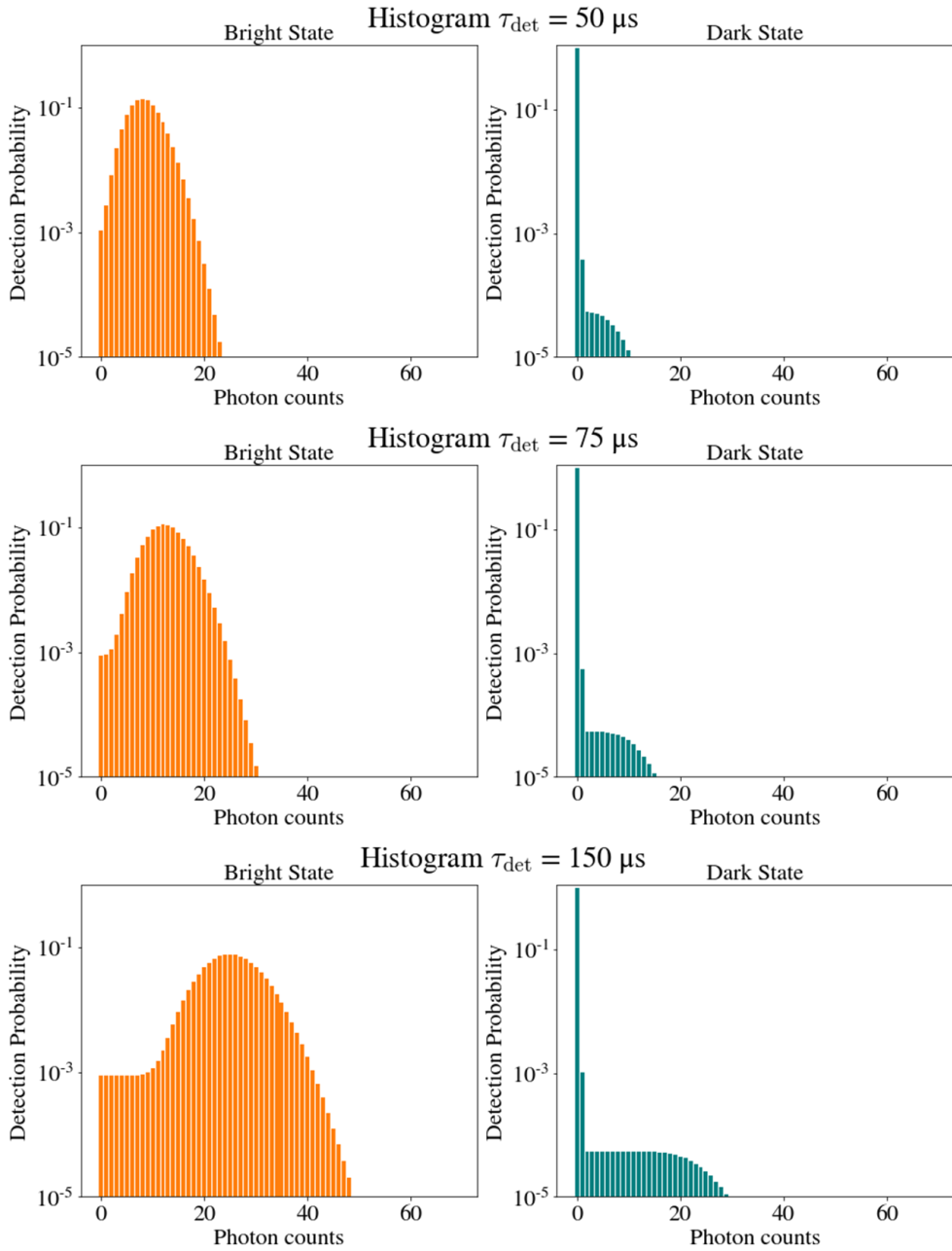


Figure 3-5. Histograms of detected photon numbers for 25  $\mu\text{s}$ , 50  $\mu\text{s}$ , and 150  $\mu\text{s}$ , respectively.

The histograms indicate that if the threshold value is set to 0.5 photons, then the fidelity of the  $|1\rangle$  state saturates as the histogram of 0 photon counts becomes saturated. However, as time passes, the histograms of the  $|0\rangle$  state above 0 photons become larger, resulting in an increased detection error rate of the  $|0\rangle$  state. Therefore, it can be concluded that if the quantum state is determined using the threshold method, the detection fidelity is maximized when the histograms of the 0 photons of the  $|1\rangle$  state are saturated.

## Chapter 4. EMCCD

### 4.1. Concept

An electron-multiplying charge-coupled device (EMCCD) is a highly sensitive device that can detect weak signals like a single photon. Its high sensitivity is achieved by an electron-multiplying (EM) gain mechanism. This mechanism involves the physical multiplication of electrons by impact ionization [37], [38].

Another important property of the EMCCD is that it has a 100% fill factor, which means that there are no gaps between the pixels of the sensor. This enables the sensor to capture the full extent of the incoming light and provides detailed spatial information without losing any photons.

An EMCCD is a suitable device that can be used for state detection of multi-qubits due to its high amplification of EM gain registers and pixels arranged in a grid that can provide spatial information of detected photons. Therefore, unlike PMTs, the EMCCD doesn't require fine alignment to recognize the source ion of the detected photons if a proper analysis method is provided.

Figure 4-1 shows the picture of the EMCCD (Andor, DU-897 BB+) used in the experiments, which is from the official website of Oxford Instruments [39]. The model has the enhanced sensitivity of the sensor about the UV lights

up to 20%, which offers better quantum efficiency and leads to improved state measurement fidelity.

Compared to the multi-channel PMTs that are commonly used for multi-qubit state discrimination, the EMCCD has a longer processing time due to the internal register processing time. However, the processing time can be reduced to a few milliseconds when the parameters are optimized and the region of interest (ROI) is minimized. Moreover, the state detection is usually carried out at the end of the algorithm, which suggests that the processing time of EMCCD is less critical compared to the gate operation time.



Figure 4-1. EMCCD device that is used for experiments.

## 4.2. Electron-Multiplying Gain

The amplification process of the signals in an EMCCD device occurs through the impact ionization of electrons resulting from the photoelectric effect. The electrons become trapped in potentials created within the Si substrate of the registers and are subsequently transferred to the next register on each clock cycle. As the electrons move, they collide with the Si substrate, producing additional electrons.

Although this process occurs with low probability ( $p \approx 0.01 \sim 0.02$ ), if many registers are employed, the net gain of the device can be significant [30]:

$$G = (1 + p)^r, \quad (4.1)$$

where  $p$  is the probability that the impact ionization occurs and  $r$  is the number of registers. With  $r = 512$ , the total gain can reach  $G \approx 1000$ .

Figure 4-2 illustrates the diagram of the EMCCD. The image section accepts incoming photons, and electrons are generated via the photoelectric effect when the image section is activated. The generated electrons are immediately transferred to the store section, where the sensors are deactivated, and no more photoelectric effect occurs. The stored electrons are then moved along the readout registers on each clock. Finally, the electrons reach the EM registers and are multiplied by impact ionization. In this region, the electrons can be multiplied up to 1000 times, and the analog-to-digital converter (ADC)

reads out the electrons as a digital value.

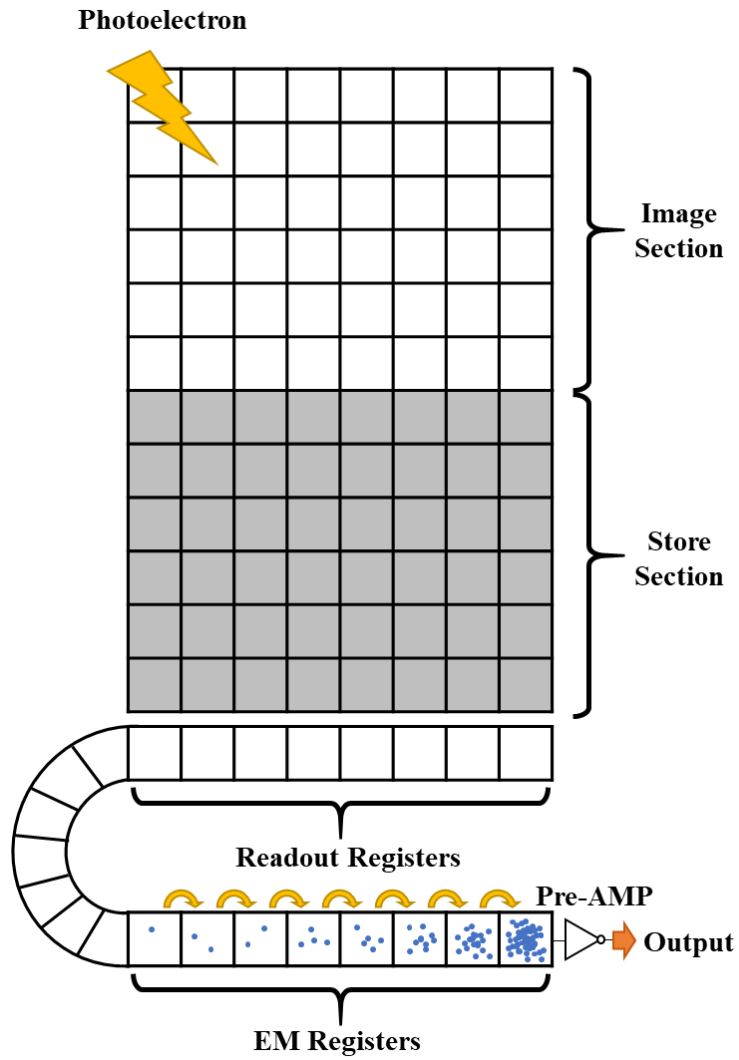


Figure 4-2. Configuration diagram of EMCCD: The image section detects photons through the photoelectric effect from the sensor.

### 4.3. Noises of EMCCD

#### 4.3.1 Signal-to-Noise Ratio (SNR)

To achieve high-fidelity state detection, one should secure a high signal-to-noise ratio (SNR). There are several types of noises in EMCCD that should be considered when one uses it as a quantum state detector.

The signal can be considered as the number of generated electrons. If we let the number of photons that are falling onto the detector  $N_p$ , then the generated electrons  $N_e$  can be written with a given quantum efficiency  $\eta_{EMCCD}$  as,

$$N_e = \eta_{EMCCD} N_p. \quad (4.2)$$

With this defined signal, the SNR can be written as

$$\text{SNR}_{EMCCD} = \frac{N_e}{\sqrt{\sum_i \sigma_{\text{noise},i}^2}}, \quad (4.3)$$

where  $\sigma_{\text{noise},i}$  denotes the deviation of the noise source  $i$  and the summation includes all the noise sources.

#### 4.3.2 Shot Noise

Shot noise is a fundamental limit to the precision of photon detection and arises due to the probabilistic nature of photons [40]. Since quantum state measurements are performed under the sub milliseconds exposure, the

contribution of the uncertain number of photons to the noise factor is significant. Therefore, every quantum state measurement suffers from the shot noise.

In the shot-noise limit, the randomly emitted photons can be modeled as the Poissonian distribution, which has the form:

$$N(n; \lambda) = \frac{\lambda^n e^{-\lambda}}{n!}, \quad (4.4)$$

where  $n$  is the emitted photon number in a given exposure and  $\lambda$  is the expectation value of the emitted photon numbers.

One notable characteristic of the Poissonian distribution is that its variance is equal to the expectation value. Thus, the contribution of the shot noise to the noise factor is as much as  $\lambda$ . The deviation of the shot noise then can be represented simply:  $\sigma_{shot} = \sqrt{N_e} = \sqrt{\eta_{EMCCD} N_p}$ .

### 4.3.3 Dark Current

Dark current is a false signal that is generated within the device due to its high sensitivity. Thermally induced free electrons from the silicon substrate can be captured as signals by the sensors, and these false signals cannot be distinguished from actual signals that originate from photon signals. However, this thermal noise can be significantly mitigated by cooling the device to

below  $-80^{\circ}\text{C}$ . To minimize this noise, the device is cooled to  $-90^{\circ}\text{C}$  and the low temperature is maintained during experiments using a connected chiller for the device.

Figure 4-3 shows the averaged measured EMCCD data in a dark room where the EMCCD device was sealed in a black box to prevent photons from entering. The total 1,000 measurement data, each measured for  $350\ \mu\text{s}$ , were averaged. This means that the noise in Figure 4-3 is solely generated from the device itself. The gradation in the data is caused by the thermal noise resulting from the unevenly distributed temperature.

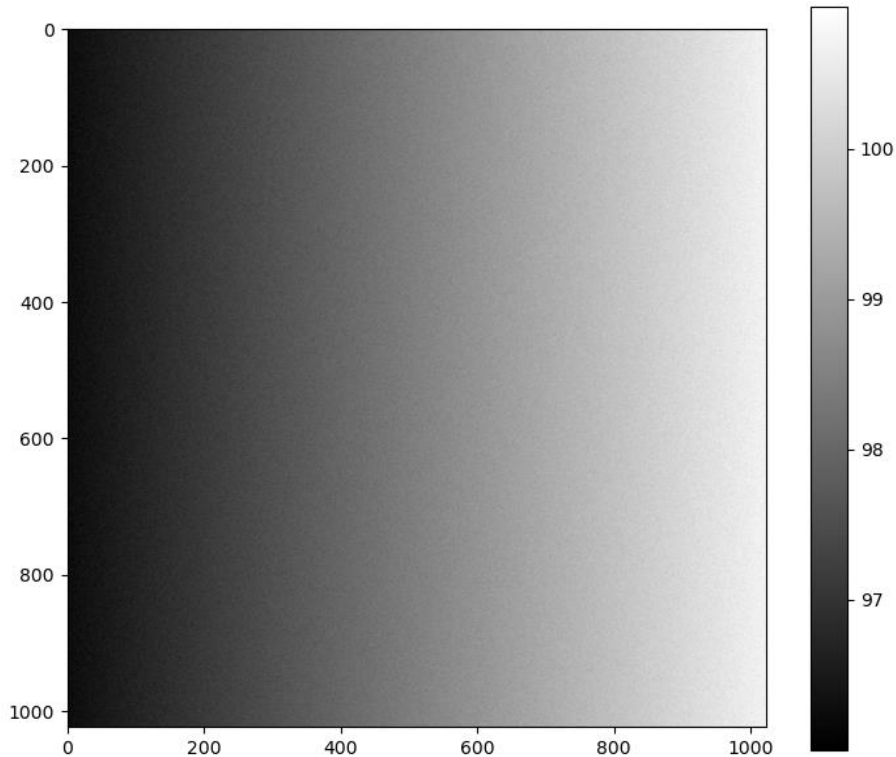


Figure 4-3. Measured dark current in EMCCD device.

#### 4.3.4 Clock-Induced Charge Noise

To achieve fast state measurement, the transfer time of generated electrons along the registers should be minimized by shortening the register shifting time. However, this short shifting time can make it more difficult for the generated electrons to transfer to the potential of the next register. To ensure that the generated electrons are transferred without loss, the clock voltage that generates a potential to trap the signal electrons should be increased. However,

this high clock voltage can be amplified in the gain registers and detected as a strong signal.

#### 4.3.5 Readout Noise

The readout noise can occur when the amplified electrons are converted into digital signals through an analog-to-digital converter (ADC) at the end of the gain register. This electrically induced noise can be modeled as white noise, which contributes to the EMCCD histograms as a convolutional Gaussian filter, leading to further broadening of the histograms.

This circuit noise can be suppressed by setting the readout speed to the lowest value. Although this readout speed increases the data transfer time and hence leads to a longer measurement time, the reduced noise is more favorable. Moreover, by setting the region of interest (ROI) of the EMCCD to the smallest possible region, the number of processed registers can be minimized, resulting in decreased readout time.

#### 4.3.6 Summary

As discussed in the previous chapters, the total SNR of the EMCCD can be written as:

$$\text{SNR}_{EMCCD} = \frac{N_e}{\sqrt{\sum_i \sigma_{\text{noise},i}^2}} = \frac{N_e}{\sqrt{\sigma_{SN}^2 + \sigma_{DC}^2 + \sigma_{CIC}^2 + \sigma_{RO}^2}}, \quad (4.5)$$

where  $\sigma_{SN}$  is the deviation of the shot noise, which is  $N_e$ ,  $\sigma_{DC}$  is the deviation of the dark current noise,  $\sigma_{CIC}$  is the deviation of the CIC noise, and  $\sigma_{RO}$  is the readout noise.

However, when the device is sufficiently cooled, the dark current noise can become negligible. In addition, if the signals are strong enough, then the readout noise can also be negligible. This leads to the SNR for the EMCCD given by:

$$\text{SNR}_{EMCCD} = \frac{N_e}{\sqrt{N_e + \sigma_{CIC}^2}}. \quad (4.6)$$

If one can minimize the CIC noise with optimized EMCCD parameters, then the SNR becomes  $\text{SNR}_{EMCCD} = \frac{N_e}{\sqrt{N_e}} = \sqrt{N_e}$ . This represents a fundamental limit of the detection of photons. With the high EM gain, the SNR can be significantly improved, enabling the detection of small numbers of photons.

# Chapter 5. Machine Learning

## 5.1. Overview

Machine learning is a fast-developing field of a branch of artificial intelligence (AI) that aims to develop algorithms by machines that can learn from data [41]. In recent years, deep learning technologies have experienced significant advancements, driven by the growth in the computing power of graphical processing units (GPUs). Deep learning, a subfield of machine learning, involves training artificial neural networks with multiple layers to extract high-level representations from raw data. This approach has revolutionized the field by enabling machines to automatically learn and understand complex patterns and relationships in data.

With the rapid development of deep learning, many groups have tried to apply this technology to various fields to achieve improved performance and to run the task automatically [42]. In this dissertation, it is aimed to enhance the fidelity of quantum state measurements of multiple ions by utilizing deep learning techniques on data measured with EMCCD.

## 5.2. Popular Algorithms in Deep Learning

### 5.2.1 Feedforward Neural Networks (FNNs)

Feedforward Neural Networks, also known as multilayer perceptrons (MLPs), are a type of artificial neural network where information flows in a single direction, from the input layer through one or more hidden layers, to the output layer.

Figure 5-1 shows the unit of a perceptron. A perceptron is one of the simplest forms of artificial neural networks initially inspired by the functioning of biological neurons in the human brain [43]. It accepts multiple inputs and each input feature is multiplied by a corresponding weight and then summed. This sum, along with a bias term, is passed through an activation function. The activation function determines the output based on the aggregated result.

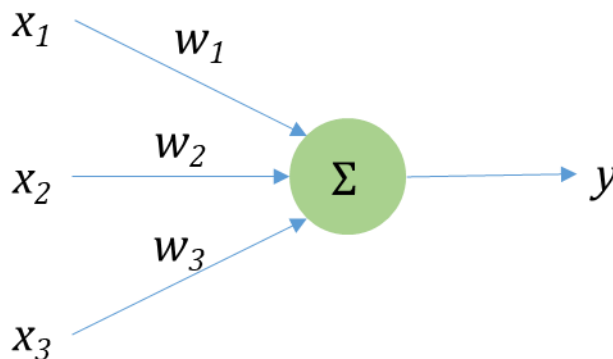


Figure 5-1. A unit of a perceptron.

However, FNNs require a large number of parameters, which results in increased memory and computing power requirements. Consequently, they are prone to overfitting [44] and redundant calculations due to the abundance of parameters. These factors make FNNs less popular in recent years.

### 5.2.2 Recurrent Neural Networks (RNNs)

Recurrent Neural Networks (RNNs) [45] are a type of neural network architecture commonly used for sequential data processing tasks such as natural language processing (NLP), speech recognition, and time series analysis.

Unlike feedforward neural networks, which process inputs independently, RNNs have a recurrent connection that allows information to be passed from previous steps to the current step. This recurrent connection enables RNNs to capture temporal dependencies and learn from sequential patterns.

The basic building block of an RNN is the recurrent unit, typically represented by a simple form called the Long Short-Term Memory (LSTM) cell or the Gated Recurrent Unit (GRU). These units have internal memory that allows them to remember information from past time steps and selectively update or forget that information based on the current input.

During training, an RNN receives input data step by step and updates its hidden state at each time step. The hidden state serves as a summary or representation of the input sequence up to that point. The output at each time step can be used for prediction, or the RNN can be designed to produce an output only at the final time step.

One key advantage of RNNs is their ability to handle variable-length input sequences. This makes them well-suited for tasks such as sentiment analysis, machine translation, and speech recognition, where input lengths may vary. RNNs can process inputs of different lengths by unrolling the network over time, treating each time step as a separate input.

However, RNNs also face challenges such as vanishing or exploding gradients, which can hinder their ability to learn long-term dependencies. To address this issue, variants like LSTM and GRU units were introduced, which incorporate gating mechanisms to control the flow of information and alleviate the vanishing gradient problem.

In recent years, more advanced sequence models like Transformer-based architectures have gained popularity, surpassing traditional RNNs in tasks such as machine translation. Nevertheless, RNNs still find applications in scenarios where sequential dependencies are crucial, or when dealing with streaming data where real-time processing is required.

RNNs are neural network architectures designed to process sequential data by utilizing recurrent connections. They excel at tasks involving sequential patterns and have been widely used in various fields of natural language processing and time series analysis.

### 5.2.3 Convolutional Neural Networks (CNNs)

Similarly, CNNs (Convolutional Neural Networks) [46] have gained popularity in various fields, especially in computer vision tasks. CNNs are specifically designed to process grid-like data such as images. They are composed of multiple layers, including convolutional layers, pooling layers, and fully connected layers.

Convolutional layers play a crucial role in CNNs. They apply a set of learnable filters to input data, enabling the network to automatically extract relevant features. These filters perform convolution operations, which involve sliding windows over the input data and computing dot products between the filter weights and the corresponding input values. This process helps capture spatial patterns and local dependencies in the data.

Pooling layers are often inserted after convolutional layers to downsample the feature maps. They reduce the spatial dimensions while preserving the important features. Common pooling operations include max pooling and

average pooling, which extract the maximum or average value from each pooling region, respectively.

The output of the convolutional and pooling layers is then flattened and fed into fully connected layers. These layers have connections between every neuron, allowing the network to learn complex patterns and make predictions based on the extracted features. The final fully connected layer typically uses a softmax activation function to produce the probability distribution over the possible output classes.

CNNs have several advantages. Firstly, they automatically learn hierarchical representations, starting from low-level features (e.g., edges and textures) to high-level features (e.g., objects and scenes). This hierarchical feature learning makes CNNs effective in recognizing complex patterns. Additionally, CNNs have fewer parameters compared to fully connected networks, which helps reduce memory and computational requirements.

Overall, the unique architecture of CNNs, tailored for processing grid-like data, along with their ability to automatically learn relevant features, has made them highly successful in various applications, including image classification, object detection, and image segmentation.

#### 5.2.4 Vision Transformer (ViT)

Vision transformer (ViT) [47] is a deep learning model that applies transformer architecture [48] to image processing. Traditionally, convolutional neural networks (CNNs) have been dominant for image-related tasks. However, ViT introduces a novel approach by leveraging the power of transformers.

The ViT model begins by dividing an input image into a grid of patches, treating each patch as a token. These patches are then linearly embedded to generate a sequence of tokens. Next, the transformer's self-attention mechanism is applied to capture the relationships between different patches in the image. This enables the model to learn global dependencies and interactions across the entire image, facilitating a more holistic understanding of the visual context.

By leveraging self-attention, ViT models have shown that they can effectively capture long-range dependencies and explicitly model the relationships between image patches, allowing for better context understanding. This helps in tasks such as image classification, object detection, and semantic segmentation. Recently, ViT models have demonstrated state-of-the-art (SOTA) performance that is comparable to CNN models.

### **5.3. Popular Base Models of CNNs**

There is a plethora of models that are frequently used as base models for CNNs. Choosing the base model depends on various factors, such as the purpose of the model, the limited computing power of the processor, the required accuracy, or the desired response time. In this chapter, popular CNN models are introduced that are focused on high accuracy but light-weighted models. These Lightweight, high-accuracy models are suitable for quantum information processing, as the controllers often suffer from limited computing resources and require fast processing times for high-speed quantum computing.

#### **5.3.1 ResNet**

ResNet [49], short for "Residual Network," is a neural network architecture that was introduced to address the challenges of training deep neural networks. Deep networks often suffer from the problem of vanishing gradients [44], [53], where the gradients become extremely small as they propagate backward through the network layers. This phenomenon hampers the learning process and makes it difficult to train deep networks effectively.

The key aspect of ResNet is the skip connections, also known as shortcut

connections or identity mappings. These skip connections allow the network to learn residual mappings, which are the differences between the desired output and the input. By introducing these shortcuts, ResNet enables the network to learn residual functions instead of trying to directly learn the underlying mapping from the input to the output.

The skip connections in ResNet operate by adding the input of a certain layer directly to the output of one or more subsequent layers. This creates a shortcut path that bypasses the intermediate layers. As a result, the network can effectively propagate gradients through the shortcut path, mitigating the vanishing gradients problem. The skip connections also facilitate the flow of information, allowing the network to retain important features from earlier layers and incorporate them into deeper layers. Figure 5-2 shows the basic residual block of ResNet. The input of the ResNet unit bypasses the convolutional layers and is directly added to the output. By including the skip connection, the gradient from the subsequent layers can flow directly to the input of the ResNet unit, allowing the network to learn residual mappings effectively and mitigate the vanishing gradients problem.

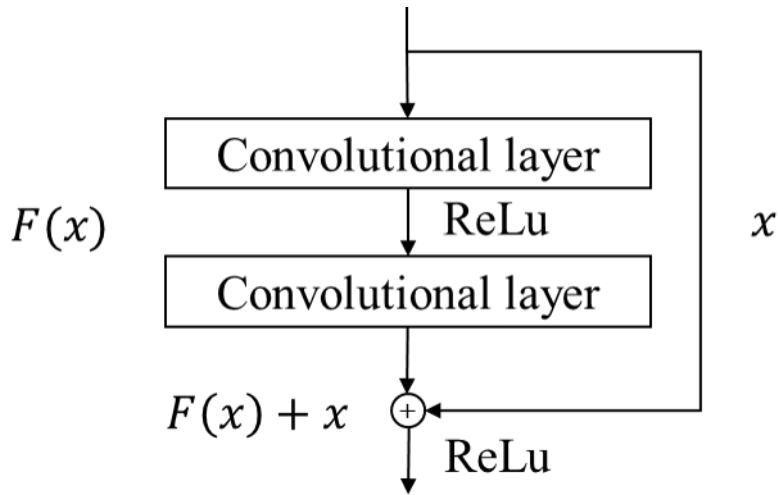


Figure 5-2. Shortcut connection in ResNet

ResNet architectures typically consist of multiple residual blocks, each containing several convolutional layers, batch normalization layers, and nonlinear activation functions. These blocks can have different depths and complexities, depending on the specific application and network requirements.

### 5.3.2 MobileNet

MobileNet [50] is a lightweight neural network architecture designed specifically for mobile and embedded devices with limited computational resources. It aims to provide efficient and accurate models for various computer vision tasks while minimizing the number of parameters and

computational complexity.

The key idea behind MobileNet is the use of depth-wise separable convolutions, which decompose the standard convolution operation into two separate operations: depth-wise convolution and point-wise convolution. Depth-wise convolution applies a single filter per input channel, independently across all input channels. Point-wise convolution then applies a 1x1 convolution to combine the output of the depth-wise convolution, allowing the network to learn complex representations with fewer parameters.

By utilizing depth-wise separable convolutions, MobileNet significantly reduces the computational cost and model size compared to traditional convolutional neural networks. This makes it suitable for real-time applications on resource-constrained devices without compromising accuracy.

### 5.3.3 SqueezeNet

SqueezeNet [51] is a compact and lightweight neural network architecture designed to achieve high accuracy while minimizing the model size and computational complexity. It aims to strike a balance between model efficiency and performance by reducing the number of parameters without sacrificing accuracy.

The key idea behind SqueezeNet is the concept of fire modules. Fire

modules consist of two types of layers: squeeze layers and expand layers. Squeeze layers primarily focus on reducing the number of input channels, while expand layers aim to capture more complex features by increasing the number of output channels.

Squeeze layers utilize  $1 \times 1$  convolutions, which have the computational advantage of reducing the number of parameters and the amount of computation. These layers effectively squeeze the input channels to a lower dimension, allowing the network to capture essential information in a more efficient manner.

Expand layers consist of a combination of  $1 \times 1$  and  $3 \times 3$  convolutions. The  $1 \times 1$  convolutions are responsible for expanding the squeezed channels, while the subsequent  $3 \times 3$  convolutions capture more spatial information and learn richer representations. By using these expanded layers, SqueezeNet can increase the model capacity while still maintaining a compact architecture.

By leveraging these design principles, SqueezeNet achieves a highly efficient architecture with a small memory footprint. It has demonstrated comparable or even superior performance to larger and more computationally intensive models, making it well-suited for scenarios with limited computational resources, such as mobile and embedded devices.

### 5.3.4 ShuffleNet

ShuffleNet [52] is also a lightweight CNN architecture that was introduced to address the need for efficient models with reduced computational complexity. The key idea behind ShuffleNet is to utilize pointwise group convolutions and channel shuffling to achieve computational efficiency while maintaining good accuracy.

## 5.4. Classification

Classification in deep learning refers to the task of assigning given input data to predefined classes or categories. It is a part of supervised learning, where the goal is to learn the relationship between input data and their corresponding classes, to make predictions on new inputs.

Deep learning models, primarily artificial neural networks, are commonly used for classification tasks. Neural networks consist of input layers, hidden layers, and output layers. By adjusting the weights and biases based on the training data, the neural network learns the relationship between the inputs and outputs.

This dissertation utilizes deep learning, specifically classification techniques, applied to EMCCD images to facilitate the measurement of quantum states in multi-qubit trapped ions. The EMCCD images are used as

input data and applied to a deep learning model for classifying quantum states in multi-qubit trapped ions.

## **5.5. Object Detection**

Object Detection is one of the important applications of deep learning in the field of computer vision. It involves identifying objects and accurately localizing their positions in images or videos. Object detection has various real-world applications, such as autonomous driving, surveillance, face recognition, robotics, airport security, and medical image analysis.

Deep learning-based object detection has made significant advancements compared to traditional methods. Previous approaches relied on predefined feature extractors and classifiers to identify objects in images. However, deep learning addresses the object detection problem with an end-to-end approach, where feature extraction and object classification are performed simultaneously.

One of the prominent methods in deep learning object detection is the Single Shot Detector (SSD) [53]. SSD is a real-time object detection algorithm capable of detecting objects of various sizes in an image simultaneously. It utilizes convolutional feature maps of different scales to predict the presence, location, and class of objects.

Other important object detection algorithms include Faster Regional Convolutional Neural Network (R-CNN) [54] and you only look once (YOLO) [55]. Faster R-CNN performs accurate object detection by employing separate networks for region proposal and object classification (a two-stage object detection). YOLO, on the other hand, provides fast real-time object detection by predicting bounding boxes and classes directly using a single neural network.

These deep learning object detection algorithms are typically based on convolutional neural networks (CNNs) and utilize weights learned from large-scale datasets for object detection. The trained models can be applied to new images to predict the presence and location of objects.

However, the object detection algorithms do not perform well for the quantum state detection of trapped ions. This is because the  $|0\rangle$  state does not scatter any photons when exposed to the detection beam, making it impossible to distinguish ions in the  $|0\rangle$  state from the background, and determine the number of ions in the  $|0\rangle$  state.

# Chapter 6. Setup

## 6.1. Experimental setup

The experimental setup used in this dissertation is illustrated in Figure 6-1. The surface-electrode ion trap, which is fabricated in this research group [18], is implemented in an ultra-high vacuum (UHV) chamber. The pressure in the UHV chamber reaches the order of  $10^{-11}$  Torr. In this high vacuum, the expected mean free path of  $H_2$  in the background is about a few thousand km, which implies any random collisions with stray molecules in the chamber can be ignored.

Three different colors of lasers are injected into the vacuum chamber through a viewport and focused on the positions where ions are trapped. A 369-nm laser is used to cool the trapped ions by Doppler cooling and to detect the quantum states of the trapped ions. A 399-nm laser is used for selectively ionizing the isotopes of the neutral ytterbium atoms. Finally, a 935-nm laser is used to repump the electrons that occasionally decay to the  $^2D_{3/2}$  manifolds by optical pumping.

A microwave antenna horn (Pasternack PE9855/SF-10) is installed to control the qubit states of the trapped ions with global radiation. It is carefully aligned to maximally deliver the power of the microwave to the ions. Additionally, a custom-designed diffraction-limited imaging lens (Photon

Gear 15470-S) with a 0.6 numerical aperture (NA) is used to collect photons emitted from the trapped ions. The collected photons are then focused either onto the sensor of EMCCD (Andor DU-897) or onto the PMT (Hamamatsu H10682-210) depending on the position of the flip mirror.

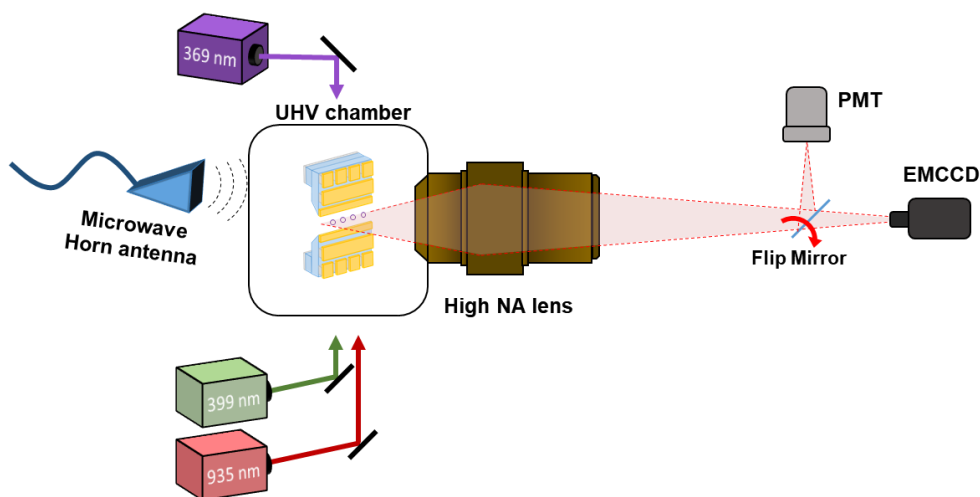


Figure 6-1. The simplified diagram of the experimental setup.

In order to simultaneously trap two different isotopes of ytterbium ions, two independent 369-nm lasers are combined using a polarized-beam splitter (PBS) before they enter the vacuum chamber. Figure 6.2 shows the combining setup. 369A is the original 369-nm laser that was initially installed, and 369B is an additional laser used to trap a different isotope. To overlap the two paths of the lasers, the PBS is installed and its two ports are used as inputs for the

two beams, respectively. The PBS transmits the p-polarized beam and reflects the s-polarized beam [40]. Therefore, if the polarizations of the two input beams are adjusted correctly, the two beams can be overlapped and combined. To minimize the leakages from the PBS due to the polarization mismatch, a half-wave plate (HWP) is installed before the PBS. This HWP allows the polarization of the beam from the fiber to be controlled.

To provide the degree of freedom of the beam path for the additional 369-nm laser, two mirrors are installed before the PBS. With these two mirrors, the beam path of 369B can be aligned to overlap the beam path of 369A. Similar to the 369A setup, a half-wave plate (HWP) is installed before the PBS to control the polarization of the 369B. Finally, the two beams are combined using a PBS and then directed toward the vacuum chamber. Once inside the chamber, they are both focused on the same location where the ions are trapped.

To maximize the scattering rate of  $^{171}\text{Yb}^+$  ions, another HWP is installed after the PBS to control the polarization of the combined beams with respect to the quantization axis of the trapped ions. A spherical lens is used to focus the beams on the trapped ions for maximum beam intensity to be delivered and to minimize the unwanted scatterings from the chip surface [23].

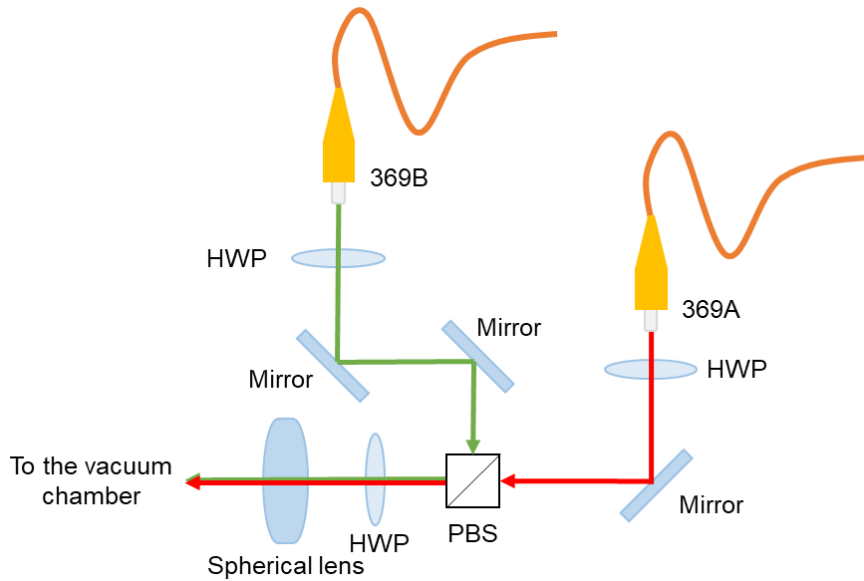


Figure 6-2. Setup for combining two laser beams.

## 6.2. Experimental Controller

Since communication with experimental devices via LAN/USB usually takes a few milliseconds, it is unrealistic to control the devices with a PC, which requires sub-microsecond controls considering the short gate times and switching times of the electro-optical or microwave devices [23].

As a controller for experiments, a field programmable gate array (FPGA, Xilinx Arty S7-50) is used and the picture of it is shown in Figure 6-3. The FPGA operates on a 100 MHz clock cycle, thus enabling it to control the experiment with a time resolution of 10 ns. The experimental sequences are programmed to the FPGA from a PC, and the FPGA runs the experiment as

scheduled. FPGA runs the programmed experiments by either reading or generating the transistor-transistor logic (TTL) signals at 3.3V logic levels via its pmod ports. The input signals are generated from detectors or other controllers for triggering and synchronizing the operation time. The output signals are mostly used to turn on and off the switches of high-frequency signals for acousto-optical modulators (AOMs) or electro-optical modulators (EOMs), or other controllers/detectors.

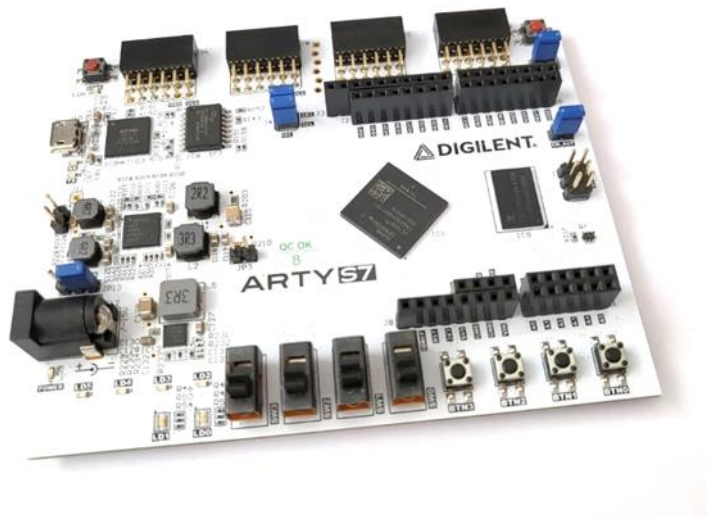


Figure 6-3. ARTY S7-50 FPGA as an experimental controller.

## 6.3. Timing Optimization

### 6.3.1 Rising time and falling time of an acousto-optic modulator

To minimize measurement error during experiments, it is important to

optimize the timings of control signals. Optimized control signals can minimize the heating time of trapped ions during operations, which results in improved qubit control fidelity [57], [58] and state detection fidelity.

For fast switching of the 369-nm laser, an AOM (IntraAction Corp. ASM-2002B8) is installed. The AOM is modulated by a 200 MHz radio frequency signal generated by a direct digital synthesizer (DDS, ANALOG DEVICES, AD9912), which is then amplified by an amplifier (MiniCircuits, ZHL-03-5WF+) up to 36 dBm to saturate the beam intensity of the 1st order laser beam.

The rising time of the AOM triggered by a user-control signal is mostly limited by the velocity of the soundwave within the crystal. Although most datasheets of AOM state that their rising times are in the ns range and define rising time as the transverse time of the soundwave of the input beam, in this dissertation, the terms "rising time" and "falling time" of the AOM specifically refer to the duration required for the 1st order modulated beam of the AOM to switch on and off, respectively, in response to a user-controlled signal.

These rising and falling times usually cannot be achieved within an ns timeline due to the relatively slow soundwave and the size of the crystal. The transducer that produces a soundwave followed by the input RF signal is usually located a few millimeters away from the laser beam, and the velocity

of the soundwave that travels within the crystal in the AOM is  $5.95 \text{ mm}/\mu\text{s}$  [59]. Therefore, the rising time of the AOM is calculated to be a few microseconds when measured.

To measure the rising time of the AOM induced by a user-control signal, a 369-nm laser was aligned to be scattered from the chip surface. The laser alignment was optimized to maximize the amount of scattering light that could be measured within a short time-bin, such as sub- $\mu\text{s}$ . The rising and falling times of the AOM are measured with a PMT by recording the time delay between the user-control signal and the PMT signals. The measured result is shown in Figure 6-4. Both the rising and falling times of the AOM were measured to be  $2.48(3) \mu\text{s}$ . These measurement results were used to schedule experimental sequences that minimize the time wasted for turning on and off the 369-nm laser.

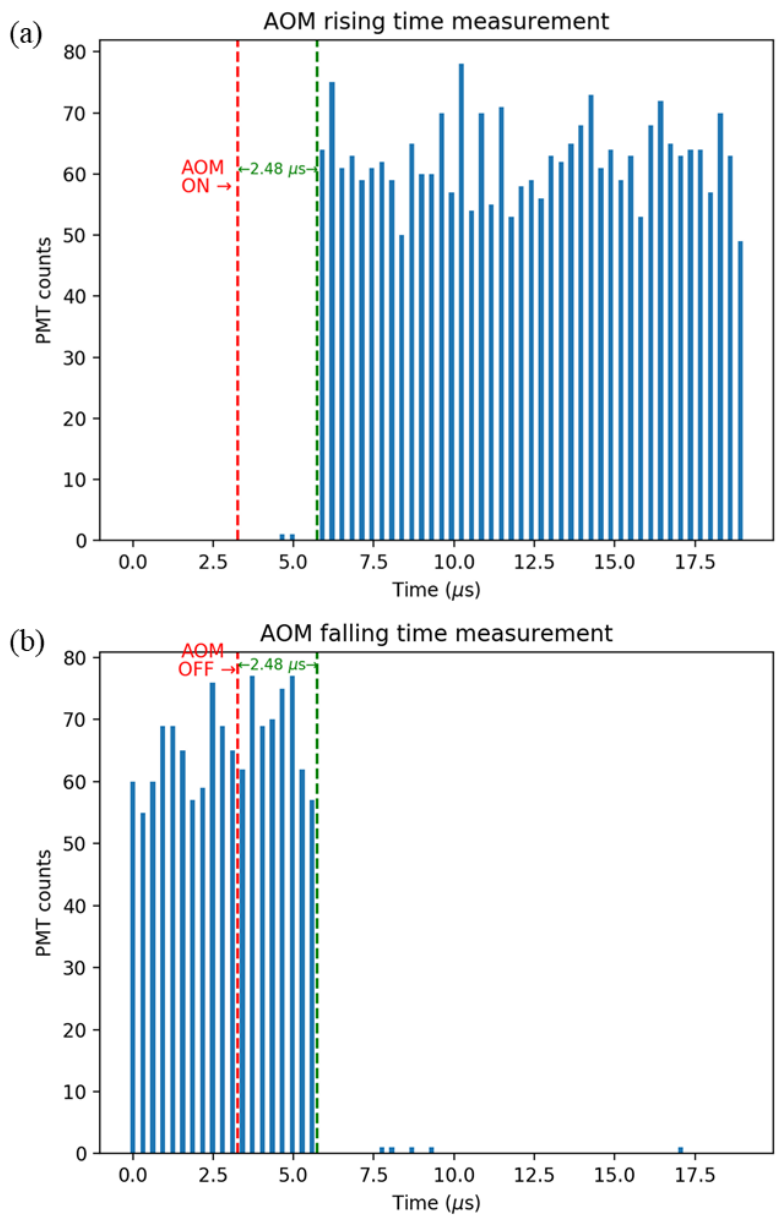


Figure 6-4. Measurement results of rising time and falling time of the AOM

### 6.3.2 Synchronization of the FPGA with EMCCD

Unlike PMTs, which emit outputs for every generated signal with a response time of a few nanoseconds, EMCCD takes more time to process the measured data due to its large number of registers. In addition, EMCCD has its own processor unit, which means it has an independent clock cycle for processing data and registers. Therefore, integrating the EMCCD into the experimental system is more challenging than integrating a PMT.

The EMCCD used in this dissertation provides two acquisition modes: the external triggering mode, whose acquisition time is determined by the external signal, and the internal triggering mode, where the device itself determines when to capture.

The process of the external triggering mode is very intuitive and easier to implement. However, the external triggering mode coerces the device into capturing the image even though the cleaning register process is not over [60]. These residual charges in the registers result in the external triggering mode generating noisier data compared to the internal triggering mode, which has a cleaning process.

Therefore, the internal triggering mode is preferred over the external triggering mode when high SNR is needed with weak signals or with short exposure time.

To use the internal triggering mode, it is required that the experimental controller is synchronized with the EMCCD. Figure 6-5 shows the D-type connector interface of the EMCCD used in the dissertation. The red dot indicates the control input for external triggering mode, the yellow dot represents the “Fire Output” that produces a high TTL signal when the device is capturing, the black dots are the ground connections, and the blue dots are not used in this experiment.

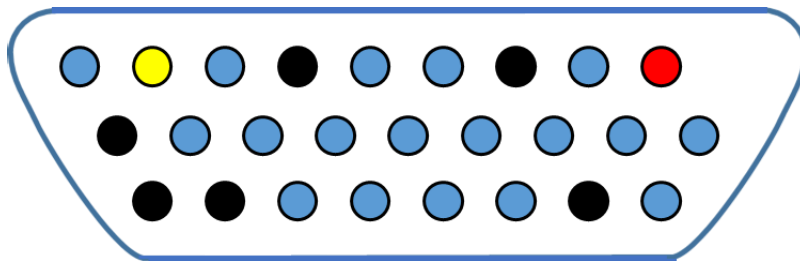


Figure 6-5. D-type connector interface of EMCCD.

The “Fire Output” is connected to one of the inputs of the FPGA to detect the signal of the fire output. the EMCCD is set to start capturing images via internal triggering mode. Since the EMCCD captures periodically, if one measures when the EMCCD captures, then it can be calculated when the next exposure occurs. Note that this capturing cycle differs by various parameters of EMCCD, such as horizontal or vertical register shifting time, the number

of pixels in the ROI, and the readout speed. To confirm whether the FPGA can correctly operate on time, the timing of the next exposure is measured using the FPGA within a 2 ms window.

Figure 6-6 shows the timing diagram of the “Fire Out” that is generated by the EMCCD device, and the stopwatch signals in the FPGA, which starts recording the time when the input signal is detected. Since the time of the first exposure is arbitrary, to reduce the ambiguity of the timing, we used the second “Fire Out” input as a time standard. The timing of the 3rd “Fire Out” then is precisely measured within 100 ns. Figure 6-7 illustrates the measured result. The expected timing of the input signal is detected as less than 100 ns (10 clocks), which is a reasonably short time compared to the AOM switching time (2.5  $\mu$ s) and the detection time (250  $\mu$ s). Thus, any errors stemming from this time margin can be negligible.

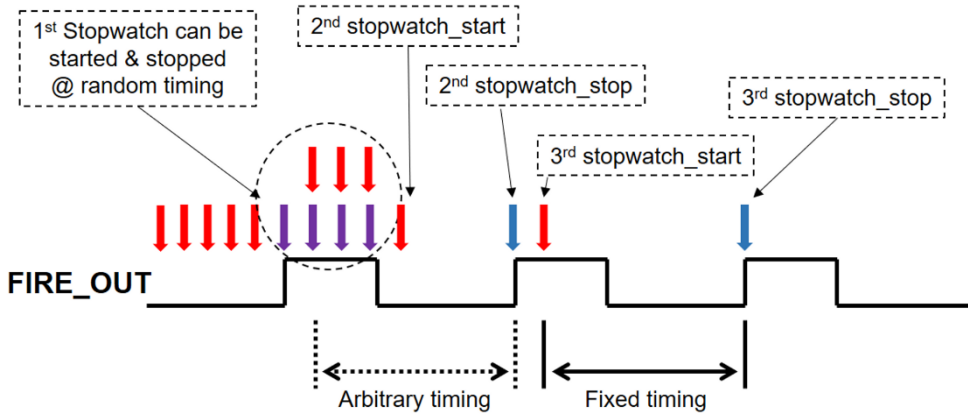


Figure 6-6. Timing diagram of the “Fire Out” and the stopwatch signals in the FPGA.

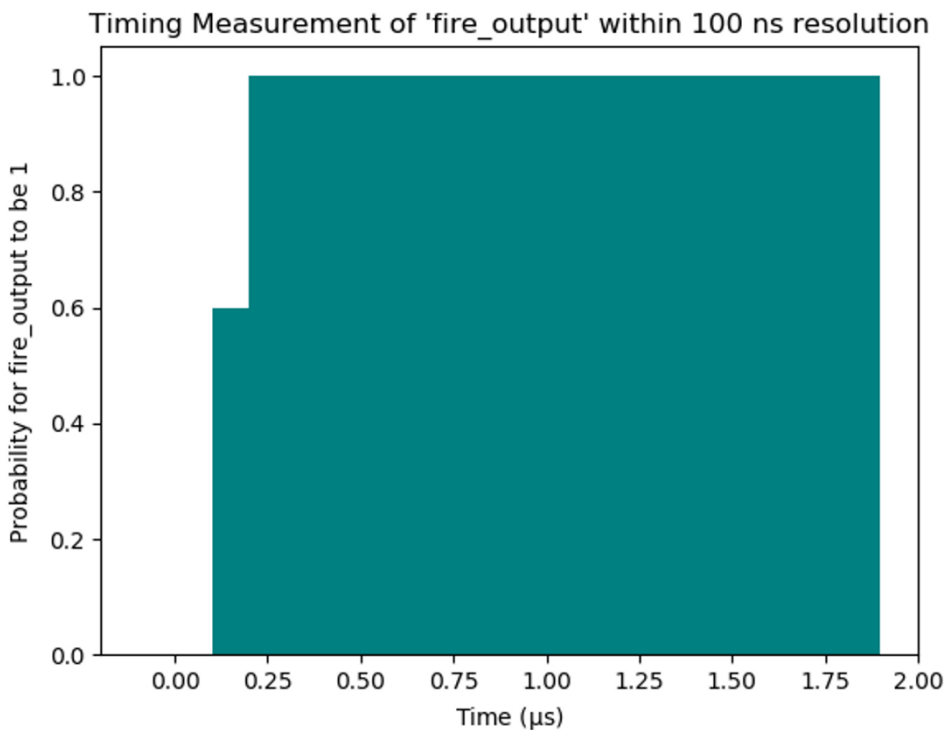


Figure 6-7. Measured result of the next “Fire Out” timing within 100 ns.

## 6.4. Parameter Optimization

### 6.4.1 High Preparation Fidelity

To achieve high-fidelity state measurements, it is a prerequisite to have a state preparation with high fidelity. Specifically, the state preparation fidelity should be at least one order of magnitude higher than the state measurement fidelity to ignore errors stemming from the state preparation. The state preparation of  $|0\rangle$  is carried out by optical pumping using a modulated 369-nm laser at a frequency of 2.1 GHz and easily achieved with an error rate less than  $1 \times 10^{-4}$  [19], [61].

The  $|1\rangle$  state is prepared by flipping the spin from the prepared  $|0\rangle$  states. To ensure that the  $|1\rangle$  state can be prepared with high-fidelity, the probability of the  $|1\rangle$  state is experimentally measured by repeatedly flipping the spin from the prepared  $|0\rangle$  state. The spin-flip fidelity is calculated from curve fitting using the following equation:

$$p_{|1\rangle}(n) = F_{det} F_{spin\_flip}^{2n-1} \quad (6.1)$$

where  $p_{|1\rangle}(n)$  is the measured probability that the ion is in the  $|1\rangle$  state after the spin has been flipped  $2n - 1$  times ( $n=1, 2, 3, \dots, n$ ),  $F_{det}$  is the detection fidelity of the  $|1\rangle$  state in the system (a constant) including the state preparation fidelity of the  $|0\rangle$  state, and  $F_{spin\_flip}^{2n-1}$  is the spin-flip

fidelity. The measured result is plotted in Figure 6-8 and the spin-flip fidelity is calculated to be 99.98(3)% from the curve fitting. This high spin flip fidelity ensures that the error rate from state preparation is on the order of  $10^{-4}$ , making it negligible when considering the measurement fidelity.

#### 6.4.2 Detection time optimization

To achieve high-fidelity state measurement fidelity, the detection time should be optimized to suppress the error rate stemming from the off-resonant transition of the  $|0\rangle$  states. To calculate the optimal detection time, the bright state pumping rate, and the dark state pumping rate are measured with respect to the beam intensity as described in ref. [26]. The measured results are illustrated in Figure 6-9.

With these pumping rates, one can theoretically calculate the optimized detection time for quantum state detection of a single ion using Eq. (3.8) and Eq. (3.9). The calculated optimal detection time for a single ion, when the threshold is set to 0.5 photons, is 89.69  $\mu\text{s}$ .

Figure 6-10 (a) shows the calculated error rates of both the  $|0\rangle$  and  $|1\rangle$  states. As the detection time gets longer, the error rate of the  $|1\rangle$  state is getting lower, and it saturates. On the contrary, the error rate of the  $|0\rangle$  state keeps larger as the detection time gets longer. Note that the optimal detection

time for quantum state detection occurs when the error rate of the  $|1\rangle$  state is saturated. Figure 6-10 (b) displays the experimental result of the single-shot quantum state detection of a trapped ion using the optimal detection time. The state detection fidelity is calculated to be 99.57(12)%, which is close to the theoretical state detection fidelity obtained from the measured pumping rate of 99.64%.

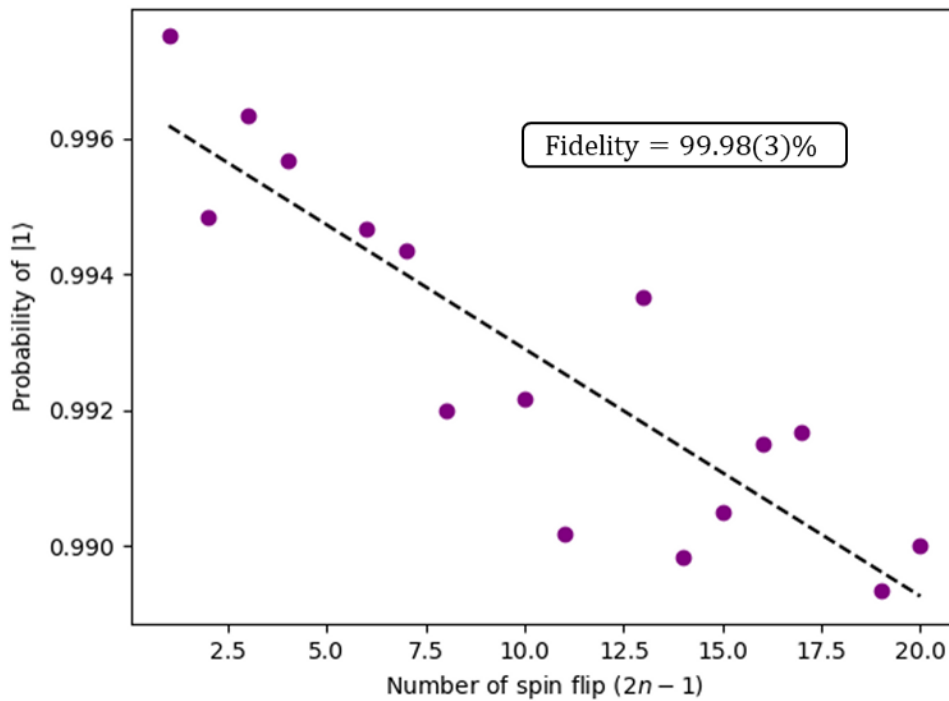


Figure 6-8. Measured spin flip fidelity by a global microwave.

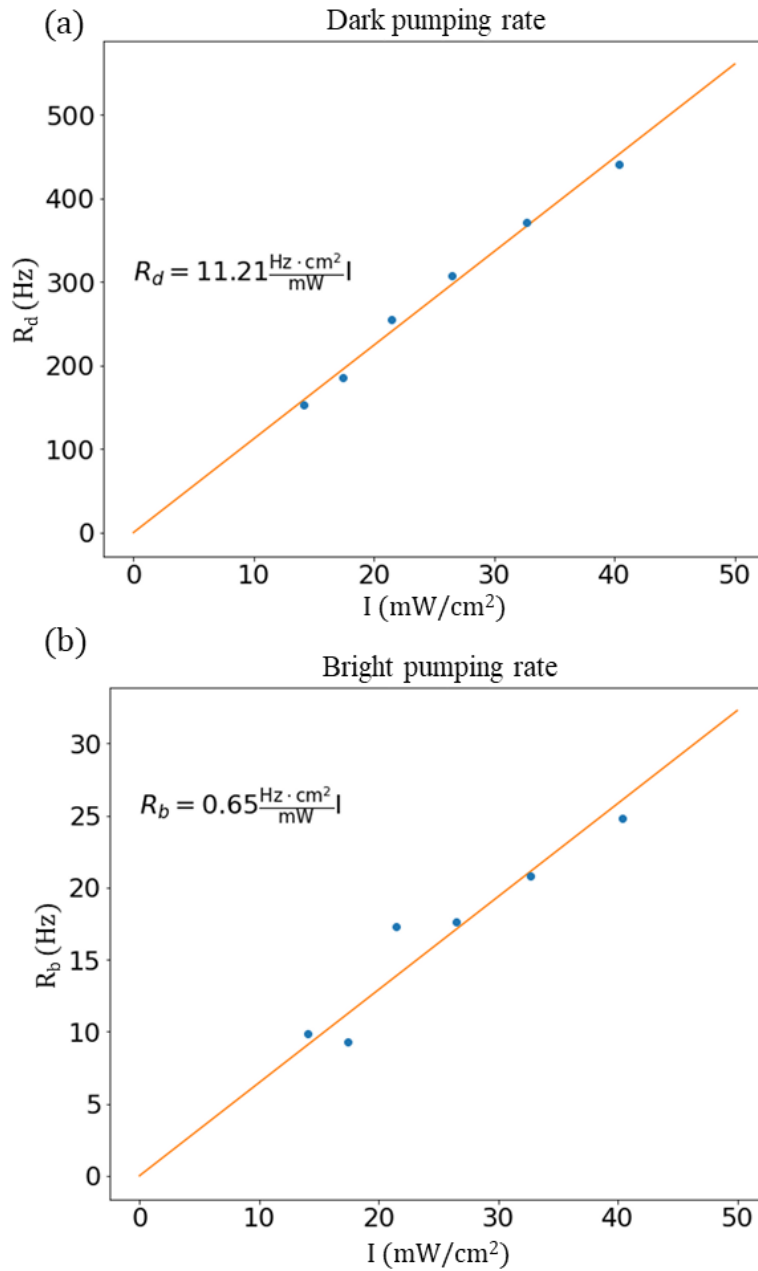


Figure 6-9. Measurements results of the dark state pumping rate and the bright state pumping rate

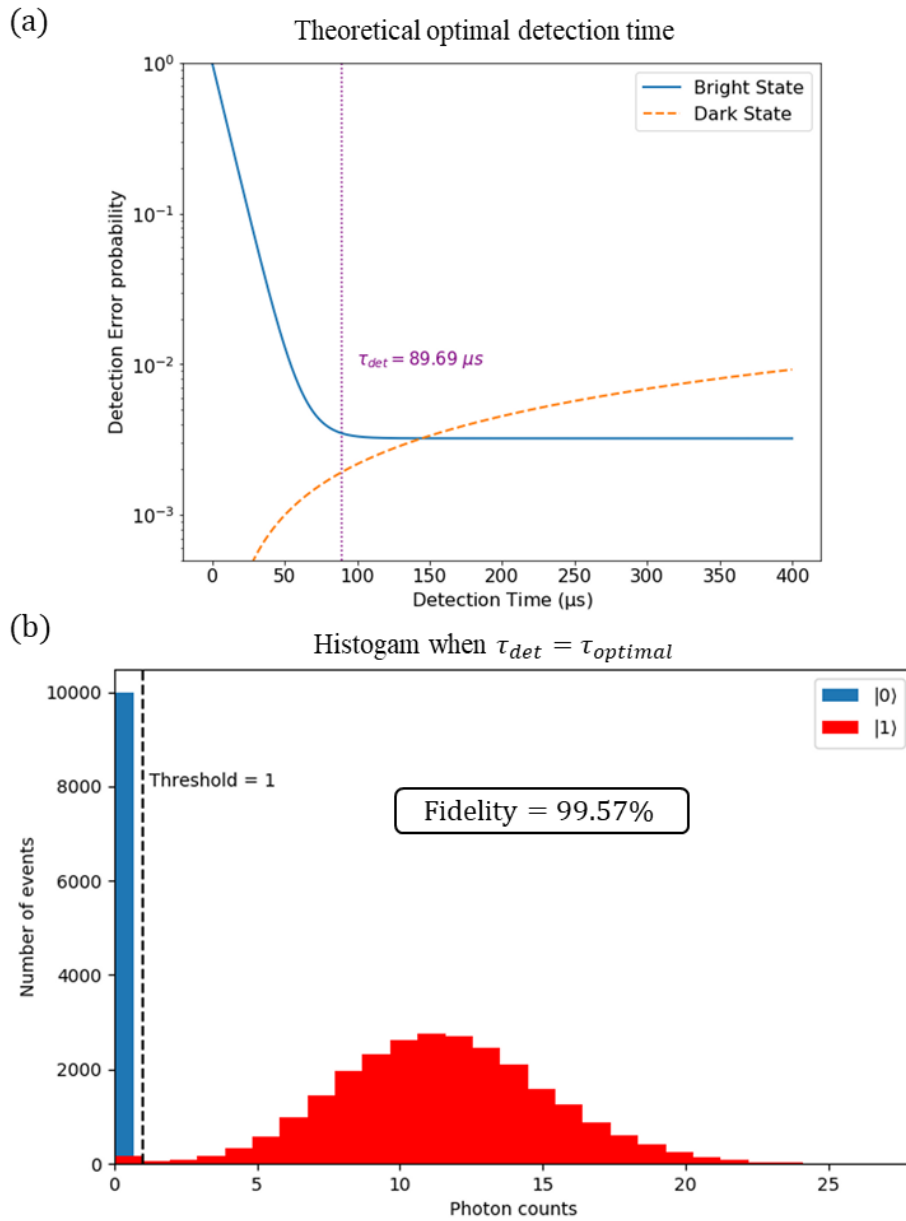


Figure 6-10. Measured single photon state detection fidelity for single-shot detection.

## 6.5. Machine Learning Model Design

To enhance the accuracy of multi-qubit ion state measurement, a ResNet-based CNN model was developed. Unlike existing pre-trained models that typically require larger input sizes of around 256x256 and utilize RGB channel values, the EMCCD data used in this experiment has a smaller size of about 36x36 and consists of 16-bit single-channel images. This difference in data characteristics poses a challenge, as the conventional models may not perform optimally when applied to this experimental data. Therefore, the model was specifically designed to address these issues, aiming to optimize performance while efficiently utilizing computational resources.

When designing the model, the following factors were taken into consideration:

1. To address the crosstalk issue, it was crucial to preserve the information about the presence of neighboring ions until the final output layer. To achieve this, ResNet and DenseNet were chosen as the base models, as they allow for the effective propagation of input image information throughout the network. However, DenseNet, which only performs concatenation without processing the input information, resulted in the propagation of false signals along with the desired information, leading to suboptimal performance.

2. An average pooling layer was used instead of a maximum pooling layer. This choice was made to avoid sampling bright false signals against the background. With average pooling, the surrounding dark background helps in averaging out these false signals, thereby improving the accuracy of the measurement.
3. The total number of layers was determined based on finding the point of saturation in performance while increasing the layer count (ranging from 30 to 102 layers). By minimizing the number of layers, computational resources could be conserved. The total number of layers is determined to be 51 layers.
4. The output size was configured to match the number of ions being measured. To prevent the exponential increase ( $2^n$ ) in the output size as the number of ions to be measured increases, the output was not represented as a one-hot vector. Instead, each output was designed to generate the quantum state of the measured ion, allowing flexibility for future measurements of varying numbers of ions.
5. Due to the correspondence between each output and the quantum state of an ion, ambiguity arose in determining the quantum states. To overcome this, each output was designed to produce quantized val

ues of 0 or 1. This was achieved by replacing the activation function of the final layer with a custom sigmoid function, ensuring that only 0 or 1 values are yielded as the training progresses.

The custom sigmoid used in the model is defined below:

$$\begin{aligned} \text{Custom sigmoid}(x, N_{epoch}) \\ = \frac{1}{1 + e^{aN_{epoch}(x+b)}} \end{aligned} \quad (6.2)$$

where  $a$  and  $b$  are hyperparameters and  $N_{epoch}$  represents the number of the training epochs. As the value of  $N_{epoch}$  increases, the gradient of the custom sigmoid function also increases. Consequently, the function eventually transforms into a step function.

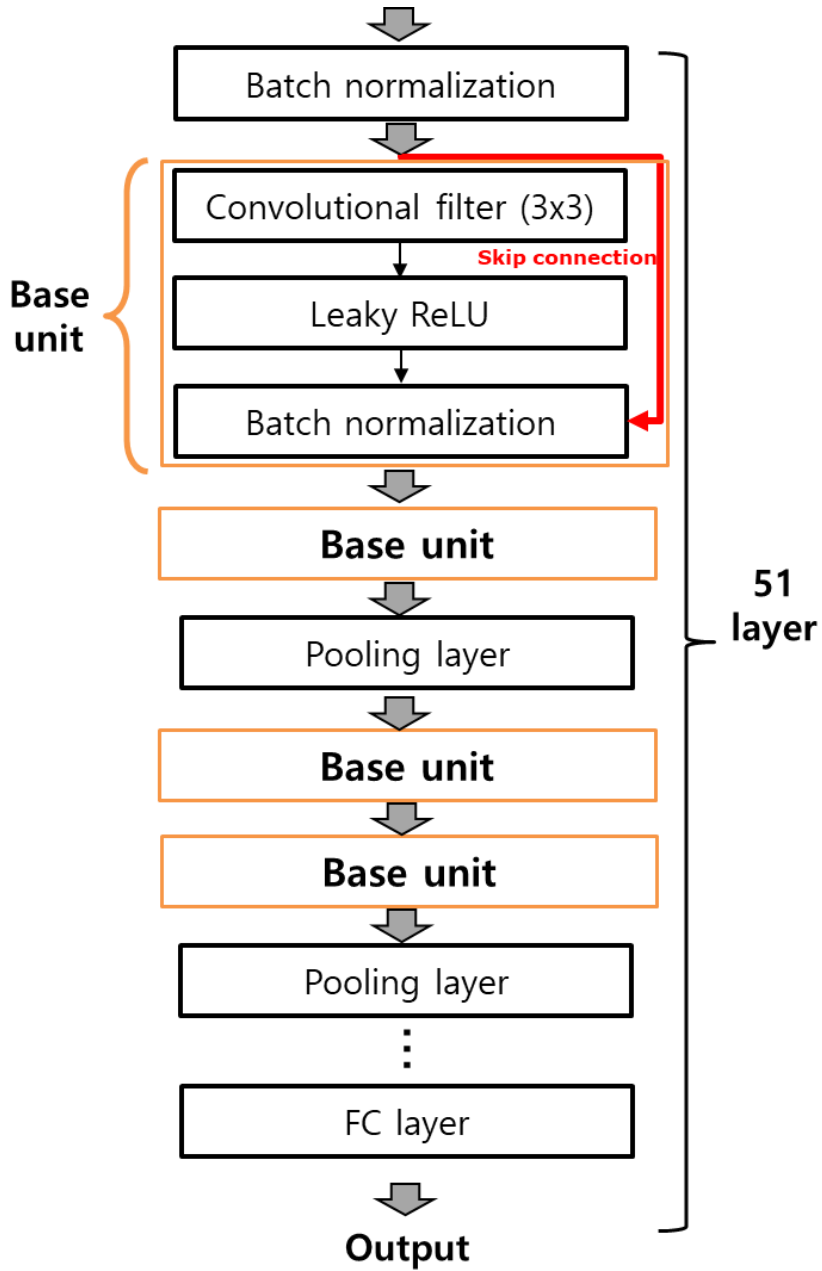


Figure 6-11. Layers of the designed Reset-Based CNN model.

# Chapter 7. Experiment

## 7.1. Multi-Qubit State Preparation

Currently, individual state control of multiple ions cannot be performed with high fidelity in our experimental setup. Therefore, to obtain data on the states of multiple ions with high fidelity, we replaced ions in the  $|1\rangle$  state of multiple ions with qubit ion  $^{171}\text{Yb}^+$  in the  $|1\rangle$  state, and ions in the  $|0\rangle$  state with the isotope  $^{170}\text{Yb}^+$  of the qubit ion that rarely interacts with the measurement beam.

The  $^{170}\text{Yb}^+$  ion is the perfect candidate to mimic the  $|0\rangle$  state of the  $^{171}\text{Yb}^+$  ion since, among other isotopes, it has the farthest resonant frequency from the detection beam, which is 5.5 GHz, and the mass difference from the qubit ion is only one neutron. Thus, any unexpected behavior due to mass mismatching in the ion chains can be excluded [62].

Figure 7-1 represents simplified energy levels of both (a)  $^{171}\text{Yb}^+$  ion and (b)  $^{170}\text{Yb}^+$  ion. The orange solid line indicates the frequency of the detection beam, and the black solid lines denote the hyperfine level splittings for  $^2S_{1/2}$  and  $^2P_{1/2}$ , which are 2.1 GHz and 12.6 GHz, respectively. The dashed solid line shows the resonant frequency between  $^2S_{1/2}$  and  $^2P_{1/2}$  of  $^{170}\text{Yb}^+$  and the required detuning frequency for off-resonant transition is represented by

the dotted blue line, which is 5.5 GHz for  $^{170}\text{Yb}^+$ .

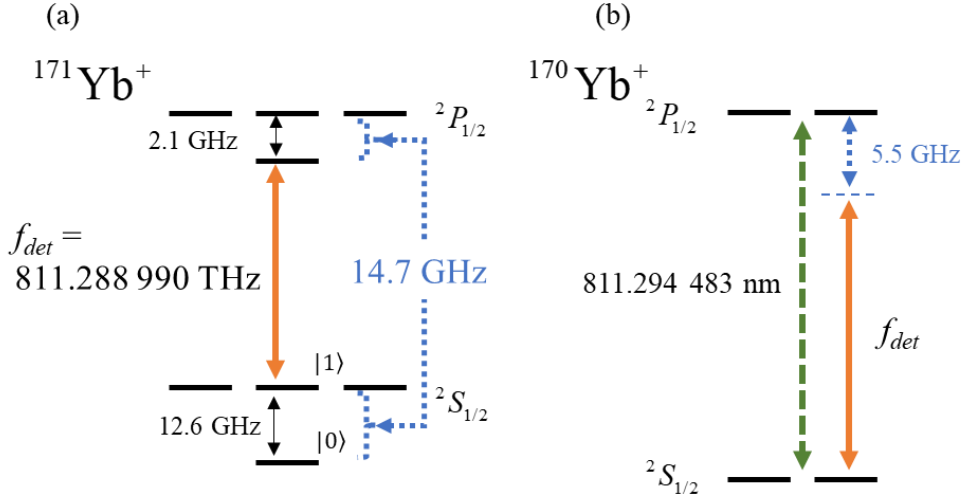


Figure 7-1. Comparison of energy levels of  $^{171}\text{Yb}^+$  and  $^{170}\text{Yb}^+$ .

To verify that the  $^{170}\text{Yb}^+$  can be used as a substitute for the  $|0\rangle$  state, the detection error rate by the off-resonant transition is calculated from the transition equation. when the detuning is large:

$$R_{off} = \left(\frac{\Gamma}{2}\right) \left(\frac{I}{I_{sat}}\right) \left(\frac{\Gamma}{2\Delta}\right)^2, \quad (7.1)$$

where  $\Gamma = 2\pi \times 19.6$  MHz is the natural linewidth of ytterbium ion, and  $I_{sat}$  is the saturation intensity,  $I$  is the beam intensity of the detection beam, which is adjusted to  $0.5I_{sat}$ , and  $\Delta$  is the detuning from the detection beam, which is 5.5 GHz. The error rate that an emitted photon by off-resonant transition is detected by the detector, which has a total photon collection

efficiency of the system  $\varepsilon = 0.023(2)$  is then,

$$R_{err} = 1 - \exp(-\varepsilon R_{off} \tau_{det}), \quad (7.2)$$

where  $\tau_{det} = 250 \mu\text{s}$  is the capturing time of the EMCCD.

Table 1 shows the detuning from the detection beam of each ytterbium isotope and their calculated error rates. The error rate of the  $^{170}\text{Yb}^+$  is the smallest due to the largest detuning, and it is less than 0.1%, which is smaller than the detection error rate of the detector. Therefore, it is valid to mimic the  $^{170}\text{Yb}^+$  ion as the  $|0\rangle$  state of the qubit ion. Furthermore, if we set the threshold of the  $|1\rangle$  state as 1.5 photons, the error rate resulting from off-resonant transitions is further reduced, since the occurrence of multiple off-resonant transitions becomes less likely.

Figure 7-2 is the EMCCD image of simultaneously trapped two different isotopes of ytterbium ions. The recorded highest values of the ROI for each ion are almost equal. However, the yellow color is painted after the acquisition of  $^{170}\text{Yb}^+$  to provide better distinguishability between the two ions. This heterogeneous trapping is used to acquire multi-qubit state detection data by mimicking the  $|0\rangle$  states of  $^{171}\text{Yb}^+$  using its isotope.

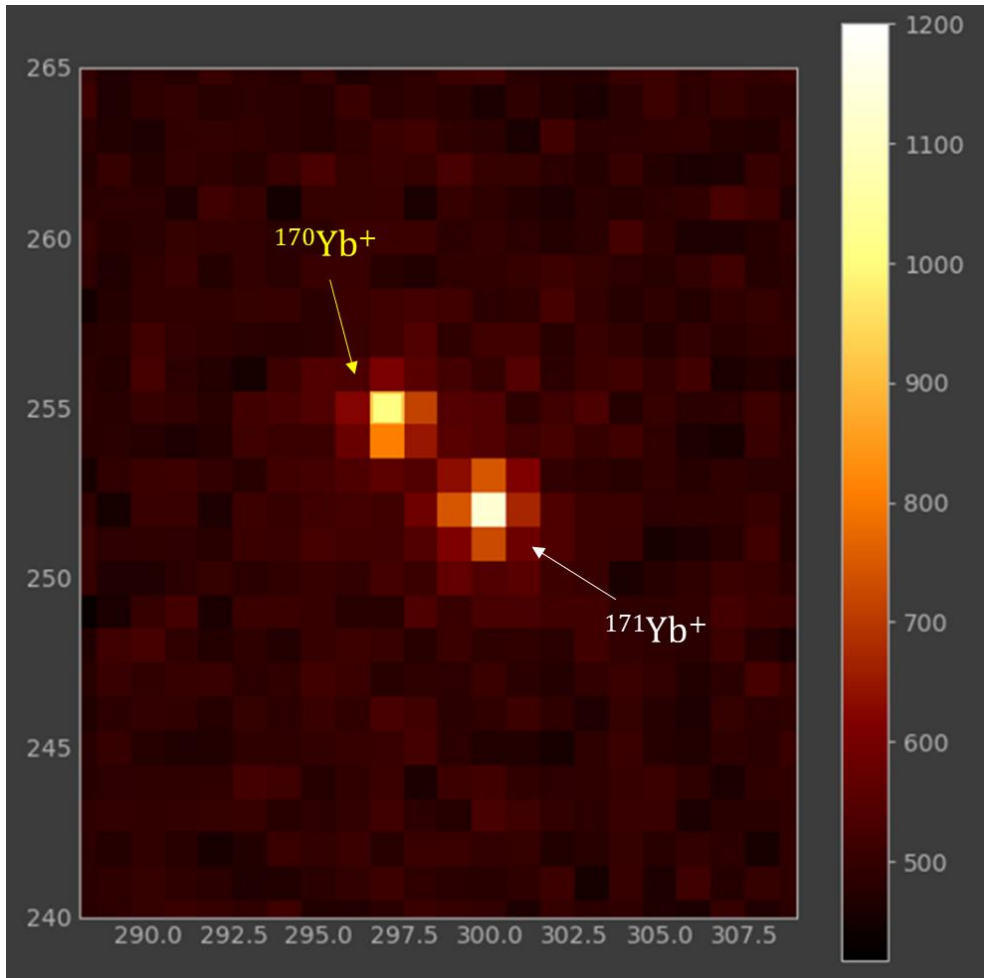


Figure 7-2. EMCCD image of simultaneously trapped  $^{170}\text{Yb}^+$  and  $^{171}\text{Yb}^+$  ions.

For the multi-qubit state detection experiment, four ytterbium ions are trapped with a combination of  $^{171}\text{Yb}^+$  ions and  $^{170}\text{Yb}^+$  ions to represent the desired multi-qubit state. For instance, if the desired state is a 4-qubit state

|0101), the four ytterbium ions should be trapped in the following order:  $^{170}\text{Yb}^+$ ,  $^{171}\text{Yb}^+$ ,  $^{170}\text{Yb}^+$ , and  $^{171}\text{Yb}^+$ .

While it would be convenient to swap or reorder specific ions within the ion chain by controlling the DC potential [53], [63], this technique has not yet been developed in our setup. Therefore, in this dissertation, the desired order is achieved in a brute-force manner. Four ions are initially trapped, and then the DC potential is intentionally perturbed by applying a high voltage to an electrode for a short duration, repeatedly. This causes the ions to briefly escape from the electrical potential, and subsequently, the cooling lasers bring them back to the center of the potential well. This process provides an opportunity for the ions to be reordered, eventually leading to the desired ion order.

Table 1. Isotopes of ytterbium ions and their transition frequency

<b>Ions of Yb isotopes</b>	$^{171}\text{Yb}^+$	$^{170}\text{Yb}^+$	$^{172}\text{Yb}^+$	$^{174}\text{Yb}^+$	$^{176}\text{Yb}^+$
Detection Frequency	811.288 990 (THz)				
Detuning from $^{171}\text{Yb}^+$ $^2\text{S}_{1/2} \leftrightarrow ^2\text{P}_{1/2}$ [19]	-	5.5 GHz	3.9 GHz	2.4 GHz	1.3 GHz
Error rate (250 $\mu\text{s}$ exp.)	-	0.06%	0.10%	0.30%	1.00%

## 7.2. EMCCD-based Multi-Qubit State Detection

Due to the stochastic nature of the photons, the activated pixels that reached photons in the ROI are arbitrary. This makes it challenging to determine the optimal ROI for state detection. To decide the optimal ROI for each ion, the photon detection rate for each ion is measured.

### 7.2.1 Characteristics of Pixels of EMCCD

According to ref. [64], the determination of optimal ROIs for each ion in EMCCD data is based on the pixel characteristics. Since every pixel in the sensor has slightly different characteristics, different criteria should be applied when determining the quantum state of the ions.

To obtain the characteristics of each pixel, their dark current rates and CIC noise rates were measured in the dark room. The EMCCD was sealed in the black box and placed in the dark room where the lights were off. Then the EMCCD captured more than 500,000 images for 250  $\mu\text{s}$  exposure. Using these data, the histograms of each pixel are curve-fitted to the model in the ref. [64] to calculate the false count generation, and minimum value of the ADC, and the variance of the readout noise. The averaged mean false signal generation rate was measured as 0.003. These fitted parameters are then utilized to generate simulated data to compensate for the insufficient number

of data points, enabling the application of the maximum likelihood method. Further details regarding this process will be explained in chapter 7.2.3.

The measured multi-qubit EMCCD images are illustrated in Figure 7-4. To find out the optimal ROI of each ion for the threshold method and MLE method, the entire data are averaged as shown in Figure 7-4 (a). In the averaged image, any spurious charges that stochastically appear are averaged out. Therefore, the averaged image is beyond the shot-noise limit, which can be analyzed in a classical approach, such as Gaussian distribution. This image is used to set an initial ROI of each ion. Figure 7-4 (b) represents acquired exemplary data of all the possible 16 states. Note that since the measurements are performed in the shot noise limit, the stochastic emission of photons makes the activated pixels in ion images unpredictable. This shot noise obscures determining the optimal ROIs of ions.

### 7.2.2 Experimental Sequence

The experimental sequence of this experiment is as follows: Firstly, the four ytterbium ions are trapped in a desired order using a combination of  $^{171}\text{Yb}^+$  ions and  $^{170}\text{Yb}^+$  ions to represent a given multi-qubit state. Then, the  $^{171}\text{Yb}^+$  ions are initialized using optical pumping with a 2.1 GHz modulated 369-nm detection beam. Subsequently, the 369-nm laser is deactivated to enable qubit

control with microwaves. The microwave switch is turned on for a duration of a  $\pi$ -pulse to flip the spin of the initialized ions, thereby placing the qubit ions in the  $|1\rangle$  state. Finally, the detection beam is activated, and the emitted photons from  $^{171}\text{Yb}^+$  ions are recorded by the EMCCD. These preceding steps are repeated over 65,000 times for each possible 16 quantum states of the 4-qubit ions to obtain enough images for multi-qubit state detection.

Figure 7-3 depicts the timing diagram of the experiment. The FPGA serves as the controller for the experimental schedule, which relies on the processing of internal registers within the EMCCD. To emit the detection beam to the ions promptly upon the EMCCD initiating image capture, the control output from the FPGA is synchronized with the signals of the EMCCD. The diagram displays the schedules after the microwave switch is turned off once the quantum state controls are completed. To minimize ion heating during the period when the cooling beam is switched off, the majority of the idle time between EMCCD image captures is allocated for ion cooling, and qubit control is executed only in the final moments.

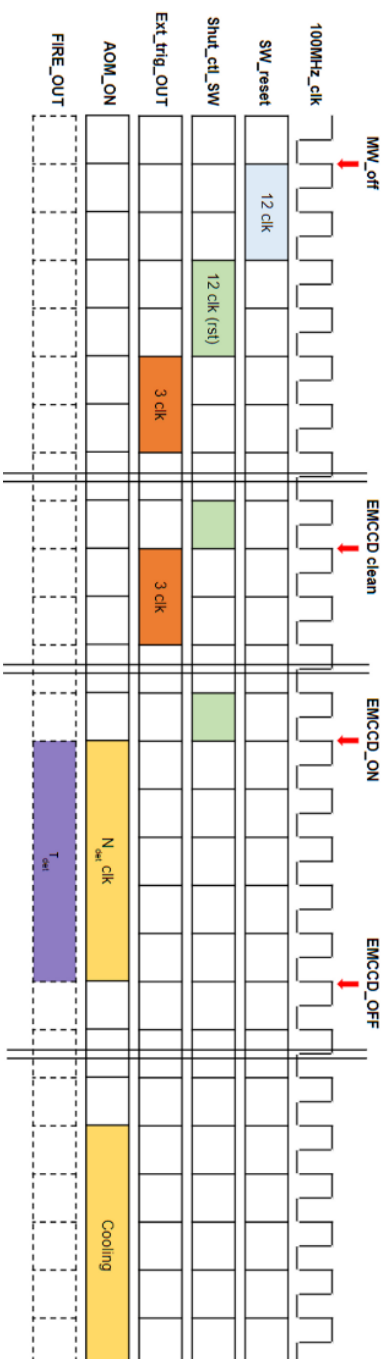


Figure 7-3. Timing diagram of the experimental schedule.

### 7.2.3 Determination of ROIs for Each Ion

The measured multi-quit EMCCD images are illustrated in Figure 7-4. To find out the optimal ROI of each ion for the threshold method and MLE method, the entire data are averaged as shown in Figure 7-4 (a). In the averaged image, any spurious charges that stochastically appear are averaged out. Therefore, the averaged image is beyond the shot-noise limit, which can be analyzed in a classical approach, such as Gaussian distribution. This image is used to set an initial ROI of each ion. Figure 7-4 (b) represents acquired exemplary data of all the possible 16 states. Note that since the measurements are performed in the shot noise limit, the stochastic emission of photons makes the activated pixels in ion images unpredictable. This shot noise obscures determining the optimal ROIs of ions.

### 7.2.4 Simultaneous Rabi Oscillation

Due to the simulation of multiple quantum states using isotopes, there was no guarantee that the proposed measurement method accurately measures the quantum states. To eliminate this ambiguity, measurements were conducted using actual qubits instead of quantum states emulated by isotopes. Therefore, four  $^{171}\text{Yb}^+$  qubit ions were trapped without isotopes, and the Rabi oscillation was measured by irradiating them with a global microwave. With the

wavelength of the global microwave spanning several centimeters, the phase differences among ions were negligible, resulting in coherent Rabi oscillations. In this dissertation, this experimental setup is referred to as simultaneous Rabi oscillation measurement. By measuring this simultaneous Rabi oscillation and observing the coherence of each ion, it is demonstrated that the measurement method proposed in this dissertation, utilizing isotopes, accurately measures the quantum states.

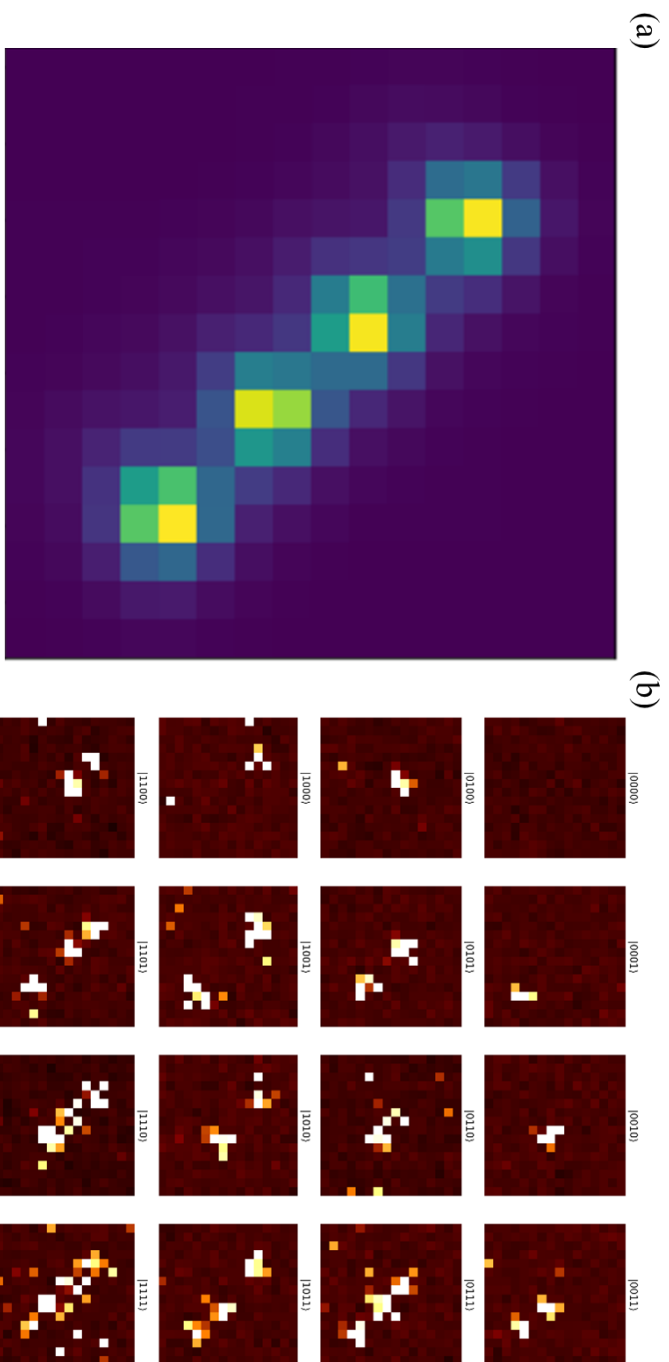


Figure 7-4. Measured 4-qubit EMCCD data: the averaged image of all data and symbolic data for each state

## Chapter 8. Results

### 8.1. Single qubit state detection

To verify the performance of the qubit state detection for the EMCCD, single qubit state detection is performed beforehand. A single  $^{171}\text{Yb}^+$  ion is trapped and prepared in either the  $|0\rangle$  state or  $|1\rangle$  state. Then more than 80,000 data for each state are acquired. Since state preparation is possible with a fidelity of over 99.9%, the state preparation error can be ignored, and only the measurement error is obtained. This measurement result is considered as the base performance for multi-qubit state detection in the next section.

The fidelity in this dissertation is defined as the probability that the expected state is measured given the prepared state. The mean measurement fidelity for the single ion is then defined,

$$\bar{F}_{single} = \frac{1}{n} \sum_s^n p(s_{meas} | s_{prep}), \quad (8.1)$$

where  $s$  represents the state of the ion,  $s_{meas}$  and  $s_{prep}$  are the measured state and prepared state, respectively, and  $n$  is the number of all possible states of the ion. For a single ion, the  $n = 2$ .

### 8.1.1 Threshold Method

Figure 8-1 shows the result of the threshold method of single qubit state detection. To calculate the fidelity of the threshold method and the optimal ROI, the pixels within the ROI are sorted from the highest mean value to the lowest mean value. Then the error rates are calculated by incrementing the number of pixels. For a given number of pixels, the threshold value is found to minimize the mean error rate of the state detection, which, in principle, minimizes the overlaps of histograms of each state.

Figure 8-1 (a) shows the error rate of the state detection with respect to the number of pixels included in the analysis. The optimal number of pixels is 8 and the error rate is 0.92%. One notable thing about applying threshold method is that, as shown in Figure 8-1 (a), the error rate is decreased initially as the number of analyzed pixels increases. However, after reaching a certain number of pixels, the error rate starts to increase. By identifying the number of pixels where the error rate begins to increase, one can determine the optimal number of pixels. Figure 8-1 (b) shows the histograms of each state when the ROI contains 8 pixels. The threshold value is set to 4,380.

### 8.1.2 Maximum likelihood method

Figure 8-2 shows the result of the maximum likelihood method on a single

ion. Based on the histograms of each state, the probabilities that a certain value occurs from the  $|0\rangle$  state and the  $|1\rangle$  state for each pixel are obtained.

Similar to the threshold method, the pixels are indexed from the highest mean value to the lowest mean value as shown in Figure 8-2 (b), and the error rate of the state detection when applied MLE is calculated by increasing the number of pixels within the ROI. The error rate with respect to the number of pixels is shown in Figure 8-2 (a).

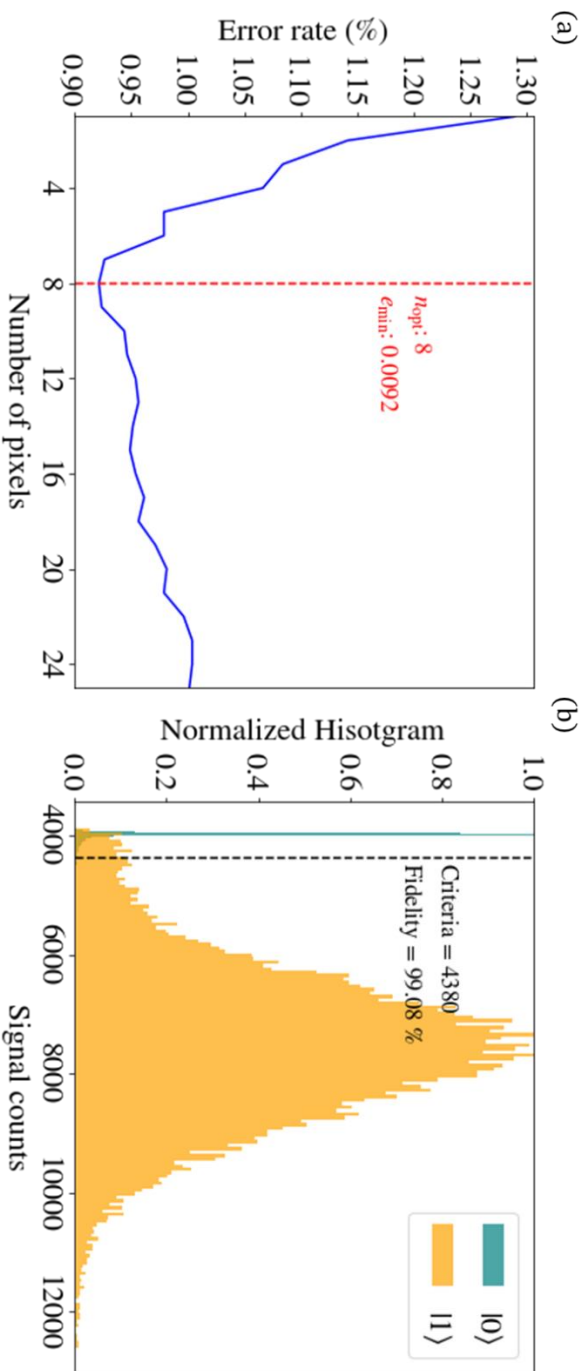


Figure 8-1. Result of applying the threshold method to single qubit state measurement.

The optimal number of pixels of ROI is found to be 30. In contrast to the threshold method, the error rate saturates as the number of pixels reaches the optimal value. Increasing the number of pixels beyond the optimal value leads to increased redundant calculations. Therefore, the optimal number of pixels is determined as the performance saturates, and the mean measurement fidelity of the MLE is calculated to be 99.72%

### 8.1.3 Machine learning

To evaluate the performance of machine learning in single qubit state detection, a CNN-based model is applied to the measured data. A simple CNN model based on VGGNet [65] is utilized, and the mean measurement fidelity is calculated to be 99.75(5)%. Trying different models to improve this result doesn't make any further improvements. This is because the model already utilizes the full information and it meets the physical limitation that cannot be improved by an analytical approach.

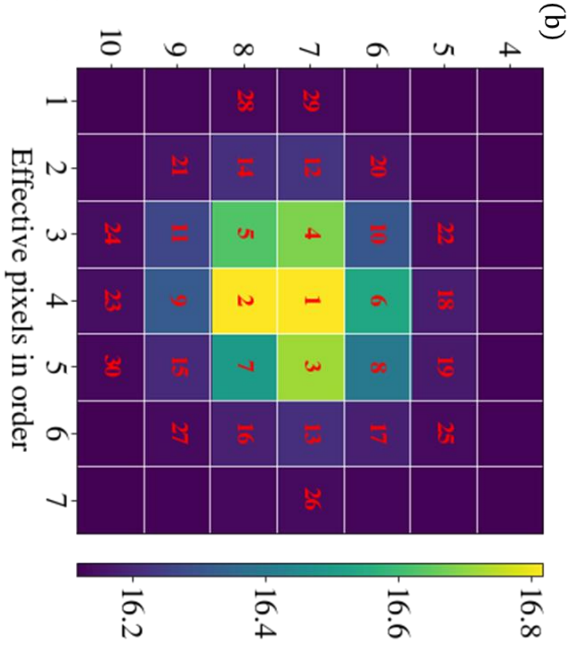
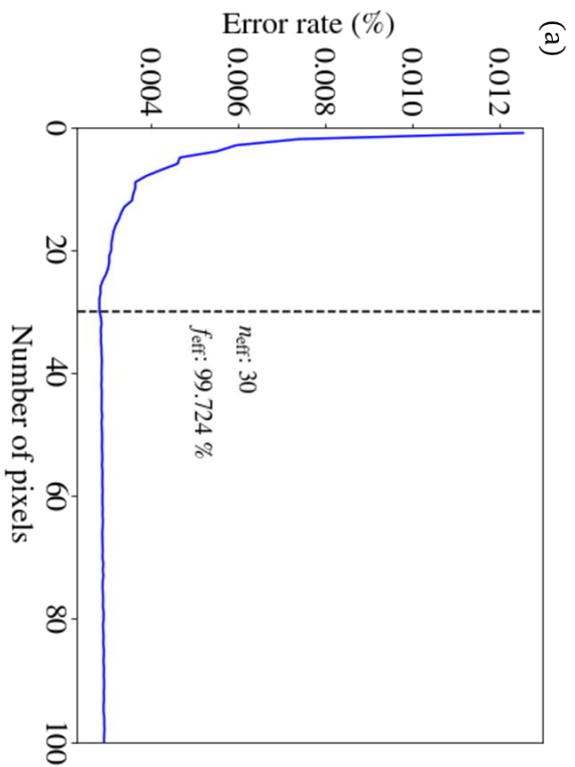


Figure 8-2. Result of applying the maximum likelihood method to a single ion for state detection.

The machine-learning model outperforms the threshold method and the maximum likelihood method. This is believed to be due to the deep neural network model can take into account the local information that is not considered in those conventional two methods. Furthermore, the deep neural network model can learn complex patterns and relationships within the data, allowing it to capture subtle features that contribute to improved state detection. This advantage over traditional methods, which rely on pre-defined thresholds or statistical models, enables the machine learning model to adapt and generalize well to varying conditions and noise levels.

## **8.2. Multi-qubit state detection**

Conventional methods such as the threshold method and MLE for multi-qubit state detection using EMCCD are not simple due to the overlaps of the ROIs among adjacent ions [64]. This detection crosstalk is a main obstacle to achieving high-fidelity state detection.

Here, two different fidelities are defined for a fair comparison: one is the fidelity of correctly measuring the multi-qubit state as a whole, and the other is the fidelity of correctly measuring each individual ion in the multi-qubit state. The former is defined as mean measurement fidelity (MMF), which can be written as

$$\bar{F} = \frac{1}{2^n} \sum_s p(\text{measured } s | \text{prepared } s), \quad (8.2)$$

where  $n$  is the number of ions and the summation index  $s$  goes over all the possible combinations of  $n$ -qubit states. The latter is defined as mean individual measurement fidelity (MIMF), which is represented as

$$\begin{aligned} & \bar{F}_{\text{indiv}} \\ &= \frac{1}{n} \sum_i \left( \frac{1}{2^n} \sum_s p(\text{measured } s_i | \text{prepared } s_i) \right), \end{aligned} \quad (8.3)$$

where  $s_i$  means the quantum state of the  $i$ -th ion in the  $s$ -th combination.

### 8.2.1 Threshold method

To evaluate the fidelity of the threshold method described in Ref. [17], the threshold method is applied to our EMCCD data as follows: To determine the initial ROIs of each ion, the average of all the acquisition data is obtained as shown in Figure 6 (a), and all the pixels within the initial ROI of each ion were sorted in decreasing order of signal intensity. Starting with the pixel with the highest signal value, the threshold value was scanned to find the highest fidelity. Subsequently, the pixel with the second-highest signal value was added to the ROI and the threshold method was applied to the sum of the ROI. The procedure continues by incrementally adding pixels to the ROI and

performing the threshold method until the highest fidelity is reached. Finally, the same procedure should be repeated for each ion and the optimal ROIs of all the ions can be obtained.

The MMF is calculated as 91.38(34)%, while 97.54(54)% is obtained for MIMF. This measurement method is vulnerable to crosstalk because we found that some pixels had to be added to more than one ROI to obtain optimal fidelity.

### 8.2.2 Maximum likelihood method

The MLE determines the state of the ion by the probability of the event. If the ion image of the obtained data has a higher likelihood of being generated by an ion in  $|1\rangle$  than in  $|0\rangle$ , then the state is determined as  $|1\rangle$ , and vice versa. By analyzing histograms of pixels, the probability of each pixel value being produced by  $|0\rangle$  or  $|1\rangle$  can be calculated. The histograms of the pixel values can be obtained from the experimental data or the simulation as well [64]. Our histograms were obtained mainly from the experiment. When the number of data is not sufficient, the histograms were interpolated by the theoretical model explained in Ref. [64].

To address crosstalk problems, the iterative method as described in Ref. [64] was applied. The result shows that this method is robust to crosstalk, and the

measurement result is consistent with the statistical calculations. The MMF of the MLE method is calculated as 96.86(9)% and the MIMF is calculated as 99.13(8)%.

### 8.2.3 ResNet-based CNN model

Although the experiment is usually performed with a fixed imaging system, small drifts of the ion image might occur over time. These small drifts can lead to a measurement fidelity drop. The conventional methods of state measurement using EMCCD are vulnerable to this kind of drift since these methods rely on pixel-specific characteristic methods [5]. The CNN architecture can cope with this kind of problem due to its inductive bias. Although the problem to solve is a translation-variant, small translation can occur due to the electrical potential drift or long-term mechanical drift of the optical components. Therefore, when the model was trained, simulated random translation data were added to the training dataset.

The total number of experimental data was 1,078,000. Half of the experimental data were used for training the model and 20% of the data were used to prevent overfitting. The rest of the data was used to calculate the fidelity. The number of generated data for simulated random translation is 20,000 for each state and these simulation data were added to the training

dataset.

The MMF is calculated as 98.32(10)% and MIMF is 99.53(14)%. We believe that the reason for the highest performance of CNN compared to other methods is that the model considers both the total counts and the image of ions simultaneously.

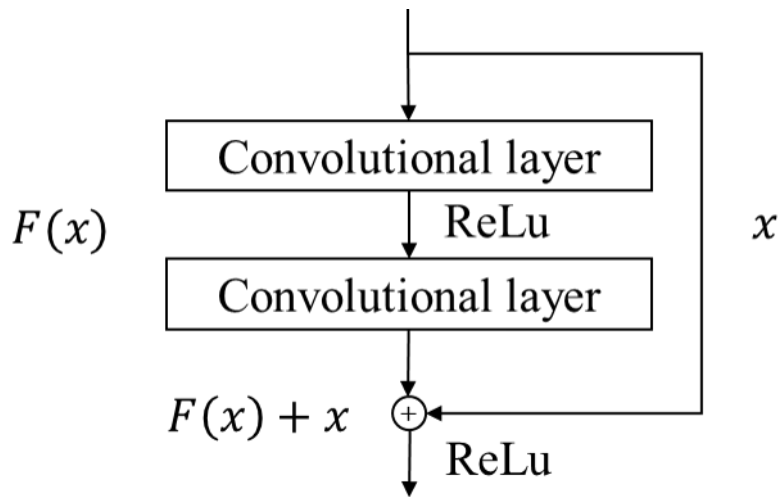


Figure 8-3. Unit structure of ResNet.

#### 8.2.4 Simultaneous Rabi oscillation of 4 qubits

To verify that the state detection of each ion is accurately made, simultaneous Rabi oscillations of four  $^{171}\text{Yb}^+$  ions by global microwave were measured with EMCCD. The oscillation result of each ion is plotted in Figure 8, which clearly shows that the 4 ions oscillate in phase. The offset of the fitted sine wave represents the detection error of the  $|0\rangle$ , which is on the order of  $10^{-4}$ .

Hence, the amplitude is almost equivalent to the measurement fidelity of the  $|1\rangle$ . The amplitudes agree with the MIMF. Therefore, it can be concluded that the CNN model correctly measures the qubit state of each ion and it outperforms the two conventional methods.

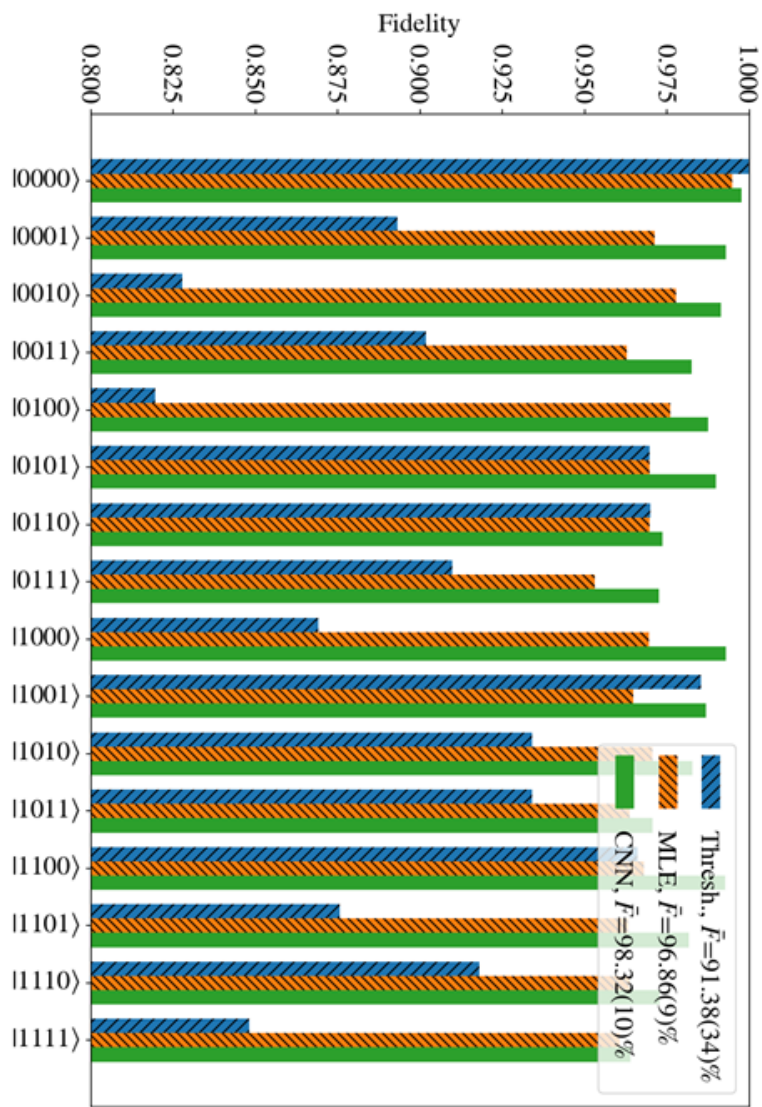


Figure 8-4. Comparison of fidelities with various state detection algorithms

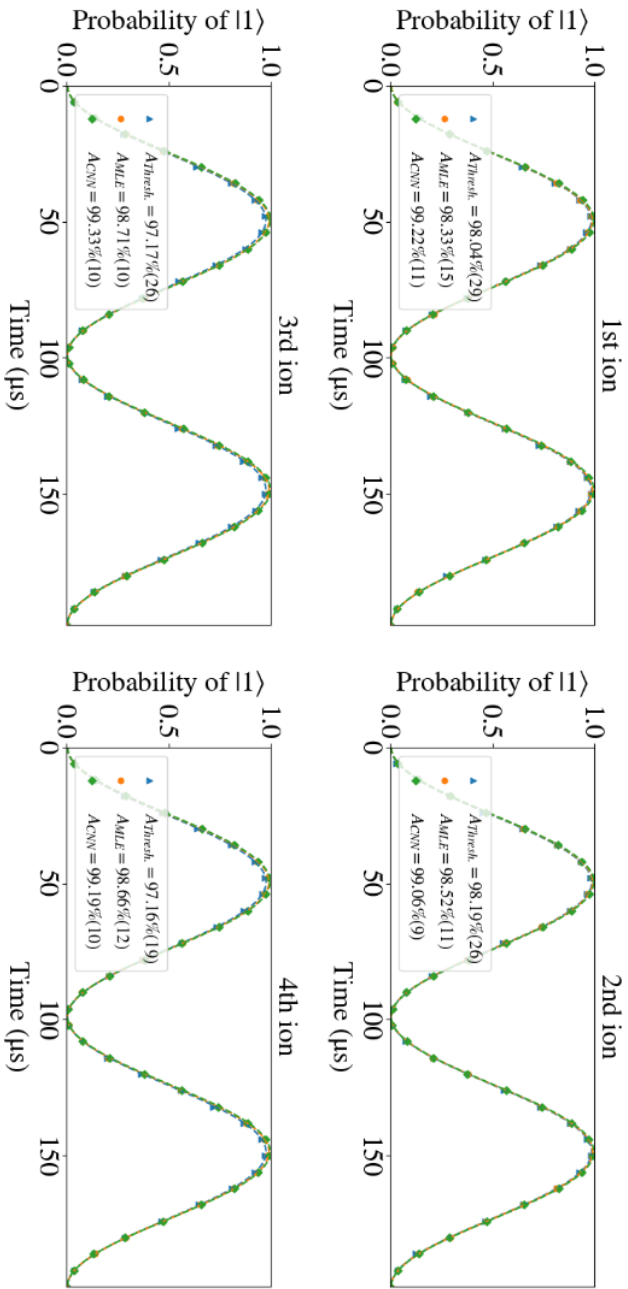


Figure 8-5. Coherent Rabi oscillation result of 4 ions.

### 8.2.5 Other Models

For comparison, other popular models that are commonly used as base models were also tested on the EMCCD images. The Vision Transformer showed similar performance to the ResNet-based CNN, indicating its effectiveness in handling the data. On the other hand, SqueezeNet, which compresses the spatial information, exhibited the lowest performance, confirming that models relying solely on spatial information tend to suffer from decreased performance.

Additionally, it was observed that models utilizing inter-channel information yielded lower performance, as expected. Conversely, models that focused on utilizing spatial information demonstrated higher performance.

Based on these results, it is evident that the performance of quantum state measurement through machine learning can be enhanced by optimizing and utilizing more suitable models.

Table 2. Performance comparison with different models.

<b>Model</b>	<b>mAP (fidelity)</b>
ResNet-based CNN	99.45%
K-Nearest Neighbors (KNN)	74.37%
Support Vector Machine (SVM)	97.10%
VGGNet16	99.27%
VGGNet19	99.37%
MobileNet V2	98.12%
MobileNet V3	98.58%
ShuffleNet V2	97.95%
SqueezeNet	97.34%
Vision transformer	99.41%

### 8.2.6 Robustness Against Optical System Drift

In addition, to test the inductive bias of the trained model and its robustness to the long-term ion image drift, the imaging lens was slightly moved to capture the ion images using the different areas of the sensor. The acquisition procedure was repeated as described above and the same types of data were acquired but in different areas of pixels.

Table 2 shows the MIMF of the 3 different methods when applied to the data that are acquired by shifting the imaging system to test robustness against

ion image drift. It should be noted that when the threshold method and MLE method were applied to the new data, they could not be directly applied since the new data had different ion spacing simulating the drift of control parameters. Therefore, the positions of ROIs were adjusted by aligning the center of each ROI in the old data with the center of each ion in the new data. On the other hand, when the new data was provided to CNN, no adjustment was made. Even though the CNN model is trained in a translation-invariant manner, it is assumed that the model is robust to small translations. This is because the model not only focuses on determining the qubit state within limited regions of interest (ROIs). Despite a slight drop in performance, the fidelity remained reasonably high, indicating that the CNN is robust to the different spacing of ions and pixel characteristics. This robustness is a significant advantage of the CNN method over the conventional methods, ensuring that measurements remain reliable over time.

Table 3. Comparison of MIMF when applied to the data with a shifted imaging system.

<b>Methods</b>	<b>Threshold*</b>	<b>MLE*</b>	<b>CNN</b>
<i>F</i> of the original pixels	97.54%	99.13%	99.53%
<i>F</i> of new pixels	96.93%	98.22%	99.12%

\*ROIs are adjusted when applied to the shifted data

## Chapter 9. Discussion and Conclusions

The multi-qubit quantum states of four trapped ions are prepared with high fidelity using a bright state by the qubit ion  $^{171}\text{Yb}^+$  in  $|1\rangle$  and a dark state represented by an isotope  $^{170}\text{Yb}^+$ . The multi-qubit states were then measured with an EMCCD and analyzed using a CNN model which is one of the popular machine-learning techniques. The CNN model is built based on ResNet architecture since the shortcut connection well preserves the original information including the presence of adjacent ions.

The measurement results with conventional methods are compared with that of this machine-learning-assisted method. The machine-learning-assisted method outperforms the conventional methods achieving a reduced error rate of 46%.

To show the inductive bias of the CNN model and its robustness to long-term drift, the same experiments were performed with the shifted imaging system. The result shows that the CNN model is robust to the long-term drift of the optical image compared to other methods, achieving 99.15(8)% MIMF without any pre-processing.

Moreover, simultaneous Rabi oscillations of four  $^{171}\text{Yb}^+$  ions are measured to prove that the model accurately determines the quantum state of each ion. The results are consistent with the individual measurement fidelity of each

ion.

In addition, the performance of the designed ResNet-based CNN model is compared to other popular image classification models to ensure a fair comparison. The results demonstrate that some conventional models achieved similar performance to the specifically designed model. However, in most cases, these conventional models have lower accuracy. The conventional models that demonstrate good performance typically have deeper layers and more parameters compared to the designed model. This suggests that models can effectively utilize computational resources when specifically designed for their intended purpose and the underlying physical model.

By utilizing machine learning for EMCCD-based multi-qubit state measurement, it is possible to perform state measurements without being constrained by predefined ROIs. This flexibility allows for more robust performance, even if there are slight variations in the positions of ions over time. This advantage ensures consistent performance over extended periods, offering greater resilience to changes in ion positions.

The machine-learning-assist method described in this paper can be further improved by providing more information to the model, such as time-binning sequential images of the data to improve the accuracy of the model.

## Appendix A. Fidelity with Different Ions

The error rate of quantum state measurements needs to be below  $10^{-4}$  for the practical realization of a quantum computer. However, the mean fidelity of quantum state measurements for each ion is approximately 99.5%, which is two orders of magnitude lower than the required criterion.

The main challenges in achieving high-fidelity quantum state measurements are the low quantum efficiency of sensors for ultraviolet (UV) light and the relatively frequent occurrence of off-resonant transitions inherent to hyperfine qubits. In this section, it is demonstrated that by changing the species of trapped ions, the proposed methods can achieve the desired error rate criteria, indicating that the method itself is not the limiting factor for practical usage.

If optical qubits are used, with each state encoded in independent transition lines, the errors resulting from off-resonant transitions can be significantly reduced. This is because the optical qubits are encoded in shelving states, where two off-resonant transitions are required to change the state. Furthermore, the two transition lines have different frequencies, which enables the filtering out of transitions from different states based on their frequencies.

Representative ions that can be utilized as optical qubits include  $\text{Ca}^+$  [70],

$\text{Sr}^+$  [71], and  $\text{Ba}^+$  [72]. Additionally, recent research has explored the use of  $\text{Yb}^+$  [73] as an optical qubit, showing the feasibility of performing quantum error correction algorithms.

The quantum efficiency of the detector can also be improved by utilizing transition lines that involve visible light, as most industrial image sensors tend to exhibit higher quantum efficiency in the visible light frequency range [74]. The EMCCD used in this dissertation has a quantum efficiency of more than 95% for visible light, which is almost three times higher than that for UV light (32%). Consequently, nearly every photon that falls onto the EMCCD can be collected and detected.

To calculate the state detection fidelity using different ions, equations (3.7) and (3.11) are used with changed parameters. The quantum efficiency is adjusted to 0.95%, resulting in  $\epsilon = 0.095$ , and the off-resonant transition rates from both the  $|0\rangle$  state and the  $|1\rangle$  state are set to 0. The calculated results for a threshold of 0.5 photons are presented in Figure A-1. The result clearly shows that the detection error rate for a single qubit can be below  $10^{-4}$ , which satisfies the requirements for quantum error correction algorithms. Furthermore, due to the negligible off-resonant transitions and high SNR from high quantum efficiency, the higher threshold value can be advantageous, Figure A-2 depicts the further reduced error rate when the threshold is

changed to 1.5 photons.5 photons.

In conclusion, the calculated results demonstrate that when using different ions, the quantum state measurement error is significantly lower than the threshold required for quantum error correction algorithms. With such a low error rate, the primary remaining source of error when measuring multiple ions is the crosstalk from adjacent ions. The measured crosstalk error rate in this dissertation is below  $10^{-4}$ . Therefore, the proposed methodology presented in this dissertation can be utilized to build a practical quantum computer with multiple qubits.

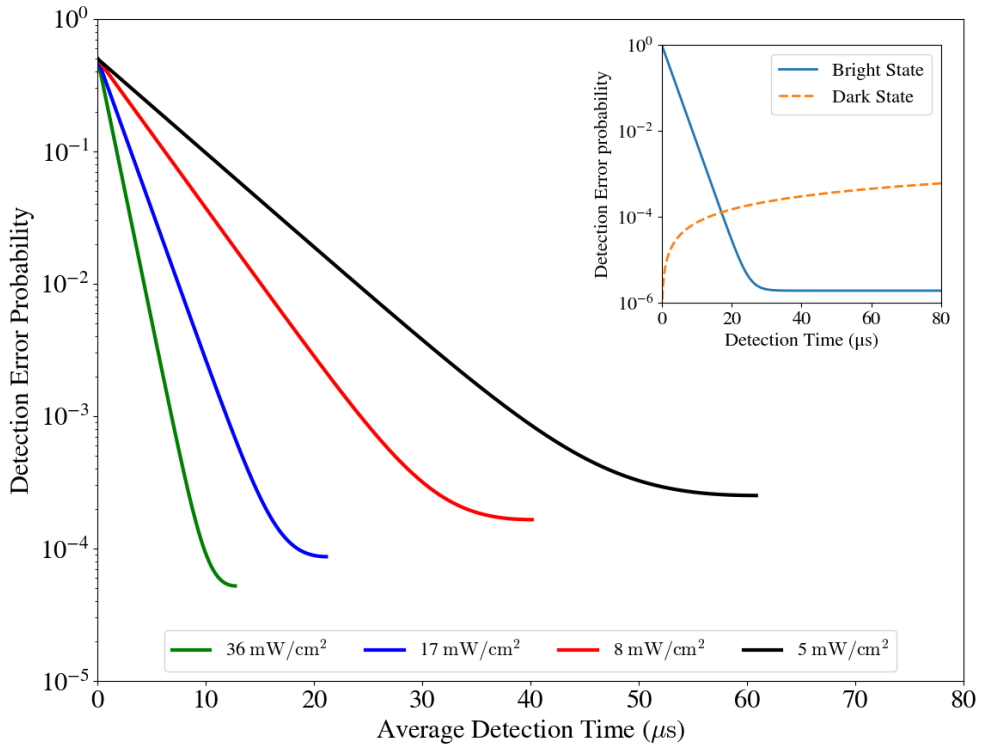


Figure A-1. Expected detection error when the ion species is changed.

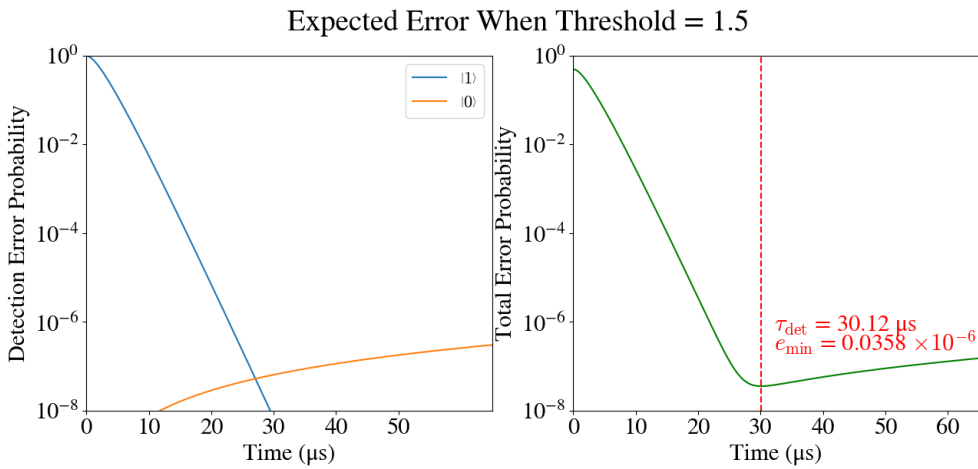


Figure A-2. Expected detection error rate when the threshold is 1.5 photons.

## Bibliography

- [1] M. A. Nielsen and I. L. Chuang, Quantum Computation and Quantum Information, 10th ed. (Cambridge University Press, Cambridge, England, 2000).
- [2] A. Galindo and M. A. Martin-Delgado, “Information and Computation: Classical and Quantum Aspects,” Review of Modern Physics **74**, 347 (2002).
- [3] A. Montanaro, “Quantum Algorithms: An Overview,” npj Quantum Information **2**, 15023 (2016).
- [4] B. M. Terhal, “Quantum Error Correction for Quantum Memories,” Review of Modern Physics **87**, 307 (2015).
- [5] T. P. Harty, D. T. C. Allcock, C. J. Balance, L. Guidoni, H. A. Janacek, N. M. Linke, D. N. Stacey, and D. M. Lucas, “High-Fidelity Preparation, Gates, Memory, and Readout of a Trapped-Ion Quantum Bit,” Phys. Rev. Lett. **113**, 220501 (2014).
- [6] B. Lekitsch, S. Weidt, A. G. Fowler, K. Molmer, S. J. Devitt, C. Wunderlich, and W. K. Hensinger, “Blueprint for a Microwave Trapped Ion Quantum Computer,” Science Advances **3**, 2 (2017).
- [7] R. Srinivas, S. C. Burd, H. M. Knaack, R. T. Sutherland, A.

- Kwiatkowski, S. Glancy, E. Knill, D. J. Wineland, D. Leibfried, A. C. Wilson, D. T. C. Allcock, and D. H. Slichter, “High-Fidelity Laser-Free Universal Control of Trapped Ion Qubits,” *Nature* **597**, 209-213 (2021).
- [8] S. Weidt, J. Randall, S. C. Webster, K. Lake, A. E. Webb, I. Cohen, T. Navickas, B. Lekitsch, A. Retzker, and W. K. Hensinger, “Trapped-Ion Quantum Logic with Global Radiation Fields,” *Phys. Rev. Lett.* **117**, 220501 (2016).
- [9] D. J. Griffiths, *Introduction to Quantum Mechanics*, 2nd ed. (Pearson Prentice Hall, 2005).
- [10] M. Knoop, N. Madsen, and R. C. Thompson, *Trapped Charged Particles: A Graduate Textbook with Problems and Solutions*, (World Scientific, 2016).
- [11] S. Earnshaw, “On the Nature of the Molecular Forces Which Regulate the Constitution of the Luminiferous Esther,” *Transactions of the Cambridge Philosophical Society* **7**, 99-112 (1842).
- [12] J. Chiaverini, R. B. Blakestad, J. Britton, J. D. Jost, C. Langer, D. Leibfried, R. Ozeri, and D. J. Wineland, “Surface-Electrode Architecture for Ion-Trap Quantum Information Processing,” *Quantum Information and Computation* **5**(6), 419-439 (2015).

- [13]D. Cho, S. Hong, M. Lee, and T. Kim, “A Review of Silicon Microfabricated Ion Traps for Quantum Information Processing,” *Micro and Nano Systems Letters* **3**, 2 (2015).
- [14]M. Lee, J. Jeong, Y. Park, C. Jung, T. Kim, and D. Cho, “Ion Shuttling Method for Long-Range Shuttling of Trapped Ions in MEMS-Fabricated Ion Traps,” *Jap. J. Appl. Phys.* **60**, 027004 (2021).
- [15]L. Deslauriers, S. Olmshenk, D. Stick, W. K. Hensinger, J. Strek, and C. Monroe, “Scaling and Suppression of Anomalous Heating in Ion Traps,” *Phys. Rev. Lett.* **97**, 103007 (2006).
- [16]I. A. Boldin, A. Kraft, and C. Wunderlich, “Measuring Anomalous Heating in a Planar Ion Trap with Variable Ion-Surface Separation,” *Phys. Rev. Lett.* **120**, 023201 (2018).
- [17]S. Hong, Y. Kwon, C. Jung, M. Lee, T. Kim, and D. Cho, “A New Microfabrication Method for Ion-Trap Chips That Reduces Exposure of Dielectric Surfaces to Trapped Ions,” *JMEMS Lett.* **27**(1), 28-30 (2018).
- [18]C. Jung, W. Lee, J. Jeong, M. Lee, Y. Park, T. Kim, and D. Cho, “A Microfabricated Ion Trap Chip with a Sloped Loading Slot to Minimize Exposing Trapped Ions to Stray Charges,” *Quantum Sci. Technol.* **6**, 044004 (2021).

- [19]S. M. Olmschenk, (2009). Quantum Teleportation Between Distant Matter Qubits, Doctoral dissertation, The University of Michigan.
- [20]P. Wang, C. Y. Luan, M. Qiao, M. Um, J. Zhang, Y. Wang, X. Yuan, M. Gu, J. Zhang, and K. Kim, “Single Ion Qubit with Estimated Coherence Time Exceeding One Hour,” *Nat. Comm.* **12**, 233 (2021).
- [21]M. Fox, *Quantum Optics: An Introduction* (Oxford University Press, Oxford, England, 2015).
- [22]M. M. Schauer, J. R. Danielson, A. –T. Nguyen, L. –B. Wang, X. Zhao, and J. R. Torgerson, “Collisional Population Transfer in Trapped Yb<sup>+</sup> Ions,” *Phys. Rev. A* **79**, 062705 (2009).
- [23]S. Hong, M. Lee, Y. D. Kwon, D. Cho, and T. Kim, “Experimental Methods for Trapping Ions Using Microfabricated Surface Ion Traps,” *J. Vis. Exp.* **126**, e56060 (2017).
- [24]J. Chivaerini, d. Leibfried, T. Schaetz, M. D. Barrett, R. B. Blakestad, J. Britton, W. M. Itano, J. D. Jost, E. Knill, C. Langer, R. Ozeri, and D. J. Wineland, “Realization of Quantum Error Correction,” *Nature* **432**, 602-605 (2004).
- [25]D. J. Wineland, J. C. Bergquist, J. J. Bollinger, and W. M. Itano, “Quantum Effects in Measurements on Trapped Ions,” *Phys. Scr.* **1995**, 286 (1995).

- [26]R. Noek, G. Vrijsen, D. Gaultney, E. Mount, T. Kim, P. Maunz, and J. Kim, “High Speed, High Fidelity Detection of an Atomic Hyperfine Qubit,” *Optics Letters* **38**(22), 4735-4738 (2013).
- [27]J. T. Merrill, C. Volin, D. Landgren, J. M. Amini, K. Wright, S. C. Doret, C. Pai, H. Hayden, T. Killian, D. Faircloth, K. R. Brown, A. W. Harter, and R. E. Slusher, “Demonstration of Integrated Microscale Optics in Surface-Electrode Ion Traps,” *New Journal of Physics* **13**, 103005 (2011).
- [28]S. Crain, C. Cahall, G. Vrijsen, E. E. Wollman, M. D. Shaw, V. B. Verma, S. W. Nam, and J. Kim, “High-Speed Low-Crosstalk Detection of a  $^{171}\text{Yb}^+$  Qubit Using Superconducting Nanowire Single Photon Detectors,” *Communications Physics* **2**, 97 (2019).
- [29]T. Harty, D. Allcock, C. J. Balance, L. Guidoni, H. Janacek, N. Linke, D. Stacey, and D. Lucas, “High-Fidelity Preparation, Gates, Memory, and Readout of a Trapped-Ion Quantum Bit,” *Phys. Rev. Lett.* **113**, 220501 (2014).
- [30]A. Burrell, D. Szwer, S. Webster, and D. Lucas, “Scalable Simultaneous Multi-Qubit Readout with 99.99% Single-Shot Fidelity,” *Phys. Rev. A* **81**, 040302 (2010).
- [31]A. Seif, K. A. Landman, N. M. Linke, C. Figgatt, and C. Monroe,

- “Machine Learning Assisted Readout of Trapped-Ion Qubits,” *J. Phys. B: At. Mol. Opt. Phys.* **51**, 17406 (2018).
- [32]Z. H. Ding, J. M. Cui, Y. F. Huang, C. F. Li, T. Tu, and G. C. Guo, “Fast High-Fidelity Readout of a Single Trapped-Ion Qubit via Machine-Learning Methods,” *Phys. Rev. Appl.* **12**, 014038 (2019).
- [33]D. J. Berkeland and M. G. Boshier, “Destabilization of Dark States and Optical Spectroscopy in Zeeman-Degenerate Atomic Systems,” *Phys. Rev. A* **65**, 033413 (2002).
- [34]I. A. Semerikov, I. V. Zalivako, A. S. Borisenko, K. Y. Khabarova, and N. N. Kolachevsky, “EIT Ground State Cooling Scheme of  $^{171}\text{Yb}^+$  Based on the  $^2\text{S}_{1/2} \rightarrow ^2\text{P}_{1/2}$  Cooling Transition,” *J. Rus. Laser Research* **39**, 568-574 (2018).
- [35]S. Olmschenk, K. C. Younge, D. L. Moehring, D. N. Matsukevich, P. Maunz, and C. Monroe, “Manipulation and Detection of a Trapped  $\text{Yb}^+$  Hyperfine Qubit,” *Phys. Rev. A* **76**, 052314 (2007).
- [36]A. Seif, K. A. Landsman, N. M. Linke, C. Figgatt, C. Monroe, and M. Hafezi, “Machine Learning Assisted Readout of Trapped-Ion Qubits,” *J. Phys. B: At. Mol. Opt. Phys.* **51**, 174006 (2018).
- [37]N. Smith, C. Coates, A. Giltinan, J. Howard, A. O’Connor, S. O’Driscoll, M. Hauser, S. Wagner, “EMCCD Technology and Its

- Impact on Rapid Low-Light Photometry,” Proc. SPIE 5499, Optical and Infrared Detectors for Astronomy, (29 September 2004).
- [38]W. Zhang, Q. Chen, B. Zhou, and W. He, “Signal-to-Noise Ratio Improvement of EMCCD Cameras,” World Academy of Science, Engineering and Technology **4**(5), 966-970 (2010).
- [39]Oxford Instruments: <https://andor.oxinst.com>.
- [40]M. Fox, Quantum Optics: An Introduction (Oxford University Press, Oxford, England, 2015).
- [41]T. Mitchell, Machine Learning, vol. 1 (New York: McGraw Hill, 2007).
- [42]P. Shinde and S. Shah, “A Review of Machine Learning and Deep Learning Applications,” 2018 Fourth International Conference on Computing Communication Control and Automation (ICCUBEA), Pune, India, 2018.
- [43]F. Rosenblatt, “The perceptron: a probabilistic model for information storage and organization in the brain,” Psychological Review **65**, 6 (1958).
- [44]I. Goodfellow, Y. Bengio, and A. Courville, Deep Learning, (MIT Press, 2016).
- [45]R. Pascanu, C. Gulcehre, K. Cho, and Y. Bengio, “How to Construct

Deep Recurrent Neural Networks,” arXiv:1312.6026 (2013)

- [46]J. Gu, Z. Wang, J. Kuen, L. Ma, A. Shahroudy, B. Shuai, Ting, Liu, X. Wang, G. Wang, J. Cai, and T. Chen, “Recent Advances in Convolutional Neural Networks,” *Pattern Recognition* **77**, 354-377 (2018).
- [47]K. Han, Y. Wang, H. Chen, X. Chen, J. Guo, Z. Liu, Y. Tang, A. Xiao, C. Xu, Y. Xu, Z. Yang, Y. Zhang, and D. Tao, “A Survey on Vision Transformer,” *IEEE Transactions on Pattern Analysis and Machine Intelligence* **45**(1) (2023).
- [48]A. Vaswani, N. Shazeer, N. Parmar, J. Uszkoreit, L. Jones, A. N. Gomez, L. Kaiser, and I. Polosukhin, “Attention is all you need,” in *Proc. Conf. Neural Informat. Process. Syst.*, 2017, pp. 6000–6010.
- [49]K. He, X. Zhang, S. Ren, and J. Sun, “Deep Residual Learning for Image Recognition.” *2016 IEEE Conference on Computer Vision and Pattern Recognition (CVPR)* (2015).
- [50]A. G. Howard, M. Zhu, B. Chen, D. Kalenichenko, W. Wang, T. Weyand, M. Andreetto, and H. Adam, “MobileNets: Efficient Convolutional Neural Networks for Mobile Vision Applications. *CoRR*, abs/1704.04861 (2017).
- [51]F. N. Landola, S. Han, M. W. Moskewicz, K. Ashraf, W. J. Dally, and

- K. Keutzer, “SqueezeNet: AlexNet-level accuracy with 50x fewer parameters and <0.5MB model size,” arXiv:1602.07360 (2016).
- [52]X. Zhang, X. Zhou, M. Lin, and J. Sun, “ShuffleNet: An Extremely Efficient Convolutional Neural Network for Mobile Devices,” arXiv:1707.01083 (2017).
- [53]W. Liu, D. Anguelov, D. Erhan, C. Szegedy, S. Reed, C. Fu, and A. C. Berg, “SSD: Single Shot MultiBox Detector,” arXiv:1512.02325 (2015).
- [54]S. Ren, K. He, R. Girshick, and J. Sun, “Faster R-CNN: Towards Real-Time Object Detection with Region Proposal Networks,” arXiv:1506.01497 (2015).
- [55]J. Redmon, S. Divvala, R. Girshick, and A. Farhadi, “You Only Look Once: Unified, Real-Time Object Detection,” arXiv:1506.02640 (2016).
- [56]Y. Wan, R. Jordens, S. D. Erickson, J. J. Wu, R. Bowler, T. R. Tan, P. Y. Hou, D. J. Wineland, A. C. Wilson, and D. Leibfried, “Ion Transport and Reordering in a 2D Trap Array,” *Advanced Quantum Technologies* **3**, 202000028 (2020).
- [57]R. J. Epstein, S. Seidelin, D. Leibfried, J. H. Wesenberg, J. J. Bollinger, J. M. Amini, R. B. Blakestad, J. Britton, J. P. Home, W. M.

- Itano, J. D. Jost, E. Knill, C. Langer, R. Ozeri, N. Shiga, and D. J. Wineland, “Simplified Motional Heating Rate Measurements of Trapped Ions,” *Phys. Rev. A* **76**, 033411 (2007).
- [58]N. V. Semenin, A. S. Borisenko, I. V. Zalivako, I. A. Semerikov, M. D. Aksenov, K. Yu. Khabarova, and N. N. Kolachevsky, “Determination of Heating Rate and Temperature of an Ion Chain in a Linear Paul Trap by the Dephasing of Rabi Oscillations,” *JETP Letters* **116**, 77-82 (2022).
- [59]IntraAction Corp. (2019). Acousto-Optic Modulator [Model ASM-2002B8]. IntraAction Corp.
- [60]User Guide, Version 3.6. Andor Technology, Belfast, United Kingdom, 2007.s
- [61]R. Noek, (2013). Integration of Advanced Optics for Trapped Ion Quantum Information Processing, Doctoral dissertation, Duke University.
- [62]K. Sosnova, A. Carter, and C. Monroe, “Character of Motional Modes for Entanglement and Sympathetic Cooling of Mixed-Species Trapped-Ion Chains,” *Phys. Rev. A* **103**, 012610 (2021).
- [63]F. Splatt, M. Harlander, M. Brownnutt, F. Zahringer, R. Blatt, and W. Hansel, “Deterministic Reordering of  $^{40}\text{Ca}^+$  Ions in a Linear

- Segmented Paul Trap,” *New Journal of Physics* **11**, 103008 (2009).s
- [64]A. H. Burrell, “High Fidelity Readout of Trapped Ion Qubits,”  
Doctoral Dissertation, University of Oxford (2010).
- [65]K. Simonyan and A. Zisserman, “Very Deep Convolutional Networks  
for Large-Scale Image Recognition,” CoRR abs/1409.1556 (2014).s
- [66]J. Zhang, G. Pagano, P. W. Hess, A. Kypianidis, P. Becker, H. Kaplan,  
A. V. Gorshkov, Z. –X. Gong, and C. Monroe, “Observation of a  
Many-Body Dynamical Phase Transition with a 53-Qubit Quantum  
Simulator,” *Nature* **551**, 601-604 (2017).
- [67]C. Piltz, T. Sriarunothai, A. F. Varon, and C. Wunderlich, “A Trapped-  
Ion-Based Quantum Byte with  $10^{-5}$  Next-Neighbour Cross-Talk,”  
*Nat. Comm.* **5**, 4679 (2014).
- [68]A. H. Myerson, D. J. Szwer, S. C. Webster, D. T. C. Allcock, M. J.  
Curtis, G. Imreh, J. A. Sherman, D. N. Stacey, A. M. Steane, and D.  
M. Lucas, “High-Fidelity Readout of Trapped-Ion Qubits,” *Phys.*  
*Rev. Lett.* **100**, 200502 (2008).
- [69]Zi. H. Ding, J. M. Cui, Y. F. Huang, C. F. Li, T. Tu, and G. C. Guo,  
“Fast High-Fidelity Readout of a Single Trapped-Ion Qubit via  
Machine-Learning Methods,” *Phys. Rev. Appl.* **12**, 014038 (2019).
- [70]A. H. Myerson, D. J. Szwer, S. C. Webster, D. T. C. Allcock, M. J.

- Curtis, G. Imreh, J. A. Sherman, D. N. Stacey, A. M. Steane, and D. M. Lucas, “High-Fidelity Readout of Trapped Ion Qubits,” *Phys. Rev. Lett.* **100**, 200502 (2008).
- [71]N. Akerman, N. Navon, S. Kotler, Y. Glickman, and R. Ozeri, “Universal Gate-Set for Trapped-Ion Qubits Using a Narrow Linewidth Diode Laser,” *New J. Phys.* **17**, 113060 (2015).
- [72]M. R. Dietrich, N. Kurz, T. Noel, G. Shu, and B. Blinov, “Hyperfine and Optical Barium Ion Qubits,” *Phys. Rev. A* **81**, 052328 (2010).
- [73]C. L. Edmunds, T. R. Tan, A. R. Milne, A. Singh, M. J. Biercuk, and C. Hempel, “Scalable Hyperfine Qubit State Detection via Electron Shelving in the  $^2D_{5/2}$  and  $^2F_{7/2}$  Manifolds in  $^{171}\text{Yb}^+$ ,” *Phys. Rev. A* **104**, 012606 (2021).
- [74]J. Ma, D. Zhang, D. Robledo, L. Anzagira, and S. Masoodian, “Ultra-High-Resolution Quanta Image Sensor with Reliable Photon-Number-Resolving and High Dynamic Range Capabilities,” *Scientific Reports* **12**, 13869 (2022).

## 초록

양자 정보 처리는 컴퓨팅, 통신 및 암호학을 혁신적으로 변화시킬 수 있는 잠재력을 지는 분야로, 최근 빠르게 성장 중이다. 대규모 양자 정보 처리 장치를 구현하기 위해서는 높은 신뢰도를 가진 양자 상태 측정이 필수적인데, 특히나 기술이 발전할수록 다루는 큐비트의 숫자가 늘어남에 따라 다중 큐비트의 개별 상태를 높은 신뢰도로 측정하는 것이 점점 어려워진다.

이온 트랩은 이온의 긴 결맞음 시간과 우주 어느 곳에서도 똑같은 특성을 갖는 자가 교정이 가능하여 양자 컴퓨터를 실현하기 위한 유망한 플랫폼 중 하나이다. 이온 트랩에서의 양자 상태 측정은 이온으로부터 상태 의존적으로 방출된 광자를 수집함으로써 이루어진다. 각 이온의 개별 상태를 측정하기 위해서는 검출기의 높은 민감도뿐만 아니라 감지한 광자의 공간 정보를 제공할 수 있는 검출기가 요구된다.

포획된 다중 이온의 양자 상태 측정을 위한 유망한 장치 중 하나는 전자증배 다중 전하 결합 소자 (electron-multiplying charge coupled device, EMCCD)이다. 이 장치는 물리적으로 전자

의 수를 증가시킬 수 있는 전자증배 이득을 통해 단일 광자 수준의 작은 신호를 증폭하여 검출할 수 있는 독특한 기능을 갖추고 있으며, 카메라와 같은 동작을 통해 검출한 광자의 공간 정보도 제공할 수 있다.

이온 트랩 분야에서 양자 상태 측정 신뢰도를 향상시키기 위해 여러 연구들이 선행되었다. 우선 실험적인 구성과 관련하여서는 방출된 광자들의 시간 정보를 활용하거나, 검출기의 양자 효율성을 향상시키거나, 광자 수집 시스템의 수집 각도 확대 등이 연구되었다. 알고리즘적인 측면에서는 이온의 양자 상태를 결정하기 위해 두 가지 방법이 연구되었는데, 첫 번째로는 측정한 데이터에서 특정 기준 값에 따라 측정한 이온의 양자 상태를 결정하는 문턱값 방법이 있고, 두 번째로는 측정 데이터가 각 양자 상태에 속할 확률을 고려하여 가장 확률이 높은 양자 상태를 선택하는 최대 우도법 방법이 있다.

최근에는 빠르게 성장하는 기계 학습 기술을 양자 상태 측정 분야에 적용하는 시도들이 있었다. 기계 학습 모델은 검출기의 잡음 패턴을 자동으로 학습하고 기존 분석에서 고려되지 않는 신호의 독특한 지엽적 패턴을 포착할 수 있는 능력을 갖고 있기 때문

에 이러한 시도들은 기존의 알고리즘 방법보다 우수한 성능을 보여주었다.

합성곱 신경망(convolutional neural network, CNN)은 이미지 및 음성 인식을 포함한 다양한 분야에서 널리 사용되는 강력한 딥러닝 알고리즘 중 하나이다. 특히나 합성곱 신경망은 주로 2차원 배열 형태의 이미지 데이터를 다루는 데 탁월한 성능을 보인다. 이는 합성곱 신경망의 독특한 아키텍처와 연산 방식으로 인해 이미지 내의 공간적 종속성과 계층적인 특징을 효과적으로 포착할 수 있기 때문이다. 합성곱층, 풀링층 및 비선형 활성화 함수를 사용하여 합성곱 신경망은 이미지로부터 관련된 특징을 자동으로 학습하고 추출하여 정확한 이미지 인식, 물체 감지 및 기타 시각적 작업을 수행할 수 있다.

본 논문에서는 4개의 이온으로 구성된 16개의 양자 상태를 높은 신뢰도로 획득하기 위해, 측정 레이저와 거의 상호 작용하지 않는 큐비트 이온( $^{171}\text{Yb}^+$ )의 동위 원소인  $^{170}\text{Yb}^+$ 를 이용하여 다중 이온의  $|0\rangle$  상태를 표현하였다. 반대로  $^{171}\text{Yb}^+$  이온은 높은 신뢰도로  $|1\rangle$  상태로 준비되어, 다중 이온의  $|1\rangle$  상태를 표현하였다. 이 방법을 통해 이온들의 개별적인 양자 상태 제어 없이 높은 신뢰도로 다중

양자 상태를 획득할 수 있었다.

위와 같이 획득한 데이터에 합성곱 신경망 모델을 사용하여 다중 양자 상태를 결정하고, 이 결과를 기존에 연구된 문턱값 방법과 최대우도법과 비교하였다. 그 결과, 기계학습을 이용한 방법의 성능이 기존 방법들을 상회하였으며, 또한 실험 장치들의 장기간 표류로 인한 이온 이미지 위치 이동에 대해서도 강건한 결과를 보여 장시간 실험 중에서도 높은 신뢰도를 제공할 수 있다.

본 논문에서 연구한 내용은 큐비트의 개수의 증가에도 성능 감소 없이 사용될 수 있으므로 향후 실제 양자 컴퓨터 개발과 양자 오류 정정 알고리즘을 실험적으로 보이는 데에 활용될 것으로 기대된다.

주요어: 이온 트랩, 기계학습, 양자 정보, EMCCD, 양자 상태 측정

학 번: 2017-28386

## 감사의 글

2017년에 신입생으로 입학하여 지금에 이르기까지의 연구실 생활 동안 많은 사람들에게서 도움을 받았고, 감사할 일이 참 많습니다. 많은 배움을 얻고자 대학원을 입학하였고, 아직도 받아야 할 배움이 많은 저이기에 많은 사람들의 도움이 없었다면 결코 이루지 못했을 성취입니다. 먼저 지금까지 저를 지지해주고 힘이 되어준 주변분들에게 감사의 인사를 드리고 싶습니다.

학위과정동안 저를 지도해주신 조동일 교수님께 감사드립니다. 부족한 저를 제자로 받아주시고 오랜 시간 동안 정성어린 지도를 해주셨습니다. 때론 엄격하게 질책하시어 저의 잘못을 바로잡아 주셨습니다. 교수님의 헌신적인 지도가있었기에 연구실 생활동안 발전할 수 있었고 그 발전들이 계속되어 지금에 이를 수 있었던 것 같습니다. 교수님의 지도를 밑거름 삼아 계속해서 발전해 나가도록 하겠습니다.

또한 연구와 관련한 조언을 구했을 때 아낌없이 도와주신 김태현 교수님께도 감사의 인사를 드립니다. 김태현 교수님의 가르침이 연구에 큰 도움이 되었습니다. 학위 심사에 참석해주셔서 저에

겐 더할 나위 없는 큰 힘이 되어 주셨습니다.

또한 제 논문 심사를 승낙해주신 박남규 교수님, 윤성로 교수님 및 이화여자대학교의 최태영 교수님께도 감사를 드립니다. 여러 교수님들의 조언을 통해 큰 가르침을 받고 학위를 마무리 할 수 있었습니다.

또한 저를 위해 지원을 아끼지 않았던 형에게도 감사를 표하고 싶습니다. 언제나 한결같이 자기 일의 책임감을 갖고 맡겨진 일에 임하는 그 모습이 큰 귀감이 되어 저도 정진할 수 있었던 것 같습니다. 항상 도움을 받으며 언젠가 보답할 날이 올 것을 기대하고 있었고, 앞으로 살아나가며 그 도움에 보답을 해나갈 것입니다.

연구실 생활을 함께하며 동고동락한 실험실원 분들에게도 감사의 인사를 드립니다. 석준이형, 민재형, 윤재형, 태재형, 철홍이형, 서형이형, 태일이형, 지석이형에게 실험실 내에서 지켜야 할 사항들에 많이 배웠습니다. 특히나 창현이에게는 많은 도움을 받은 것 같습니다. 더불어 진우, 태호, 태엽이, 영석이, 승현이, 대영이, 현택이, 지성이, 태훈이, 정현이 및 숙영 누나에게도 감사의 마음을 전합니다.

그리고 연구실 생활이 힘들 때에 지지해주고 격려를 해준 주현

이와 홍범이에게 감사한 마음을 전하고, 대응이에게는 일이 바빠 자주 만나지 못해 미안한 마음을 전합니다.

마지막으로 저를 항상 지지해주고 따뜻하게 맞이해주신 어머니께도 감사의 마음을 전합니다. 그 헌신적인 사랑을 통해 제가 이러한 성과를 이루어 낼 수 있었습니다.

И я также хотел бы выразить свою благодарность Алине за то что верила в меня и безграничную поддержку когда я проходил через трудные времена, связанные с моей работой в науке. Её присутствие было просто чудесным. Она давала мне силу и поднимала мое настроение, и я смог находить пути вперед в итог.

년

월

일

정

준

호